ICFO-INSTITUT DE CIÈNCIES FOTÒNIQUES

&

UPC-UNIVERSITAT POLITÈCNICA DE CATALUNYA

Sources of Photonic Entanglement for Applications in Space

FABIAN STEINLECHNER

Thesis Advisor: Prof. Valerio Pruneri

PhD Thesis - 2015

To my grandparents
Dolly, Josef, Eileen and Lawrence

Abstract

The nonlocal correlations of entangled systems are fundamentally at odds with our common-sense notions of realism and locality. Additionally, quantum entanglement is an essential resource for numerous quantum communication protocols such as quantum teleportation and quantum dense coding, quantum cryptography, as well as quantum-enhanced metrological schemes and quantum computation. These quantum schemes allow for significant gains in performance over their classical counterparts, and a commercial implementation of protocols utilizing entangled photons thus seems likely in the foreseeable future. A key challenge to be addressed, in order to achieve a global-scale implementation of quantum-enhanced protocols, is the distribution of entanglement over long distances.

While photons are in many ways ideal carriers of quantum information, their distribution over long distances is significantly impeded by losses. At present, loss in optical fiber links, or atmospheric attenuation and obstructions of the line of sight in terrestrial free-space links, limit the distribution of photonic entanglement to several hundred kilometers. Installing sources of photons with quantum correlations on space platforms would allow such distance limitations to be overcome. This would not only lead to the first global-scale implementation of quantum communication protocols, but would also create the opportunity for a completely new class of quantum experiments in a general relativistic framework.

State-of-the-art laboratory sources of entangled photons are generally ill-suited for applications in harsh environments such as space, either owing to the use of bulky lasers, the requirement for active interferometric stabilization, or insufficient photon-pair-generation efficiency. Thus, an integral milestone for the experimental implementation of quantum communication protocols over satellite links is the development of robust, space-proof sources of entangled photons with high brightness and entanglement visibility.

This thesis is intended to bridge laboratory experiments and real-world applications of quantum entanglement in harsh operational conditions. To this end, the main results of this thesis are:

- Highly efficient sources of polarization-entangled photons for the distribution of entanglement via long-distance free-space links. The sources are very robust and compact, and incorporate only components which are compliant with the severe requirements of space flight and operation.

- Study and optimization of spectral properties and fiber-coupling efficiency of photon pairs generated via spontaneous parametric down-conversion in bulk periodically poled potassium titanyl phosphate. The results of these studies are of great practical relevance for the development of an ultra-stable and efficient entangled photon source.

- Engineering and characterization of field-deployable polarization-entangled photon sources with high visibility ($>$99%) and record pair-detection rates ($>$3 million detected pairs per mW of pump power). As a result of the performance demonstrated, the sources developed have been incorporated into ongoing experiments, for example in quantum nanophotonics and quantum communications, and will provide an enabling tool for future real-world applications.

Resumen

Las correlaciones no locales de sistemas entrelazados son una característica inherente a la teoría cuántica que está fundamentalmente en desacuerdo con nuestra noción intuitiva de realismo y localidad. Además, el entrelazamiento es un recurso esencial en numerosos protocolos de comunicaciones cuánticas, como por ejemplo la teleportación cuántica o la criptografía cuántica, en esquemas metrológicos cuánticos y en computación cuántica. Todos estos esquemas cuánticos permiten mejoras significativas de rendimiento con respecto a sus homólogos clásicos, por lo tanto, parece previsible que en un futuro próximo veamos implementaciones comerciales de protocolos que utilicen fotones entrelazados. Un reto fundamental con el fin de lograr una implementación a escala global del entrelazamiento cuántico es su distribución a grandes distancias.

A pesar de que los fotones son portadores ideales de información cuántica, su distribución a través de largas distancias está significativamente limitada por pérdidas. En la actualidad, las pérdidas introducidas por las fibras ópticas, la atenuación atmosférica, o la dificultad de obtener una línea de visión directa en enlaces terrestres limitan la distribución de entrelazamiento fotónico a varios cientos de kilómetros. La instalación de fuentes de fotones con correlaciones cuánticas en plataformas espaciales permitiría superar tales limitaciones de distancia. Esto no sólo daría lugar a la primera aplicación de protocolos de comunicación cuántica a escala mundial, sino que también daría la oportunidad de llevar a cabo un nuevo tipo de experimentos cuánticos en un marco de la relatividad general.

Las fuentes de fotones entrelazados que podemos encontrar hoy en día en los laboratorios de óptica cuántica no están en general preparadas para ser usadas en entornos hostiles, como podría ser el espacio, ya sea por la utilización de láseres voluminosos, la necesidad de estabilizar interferómetros activamente o simplemente por tener una eficiencia insuficiente. Por lo tanto, un prerrequisito para lograr la implementación experimental de protocolos de comunicación cuántica a través de enlaces satelitales es el desarrollo de fuentes de fotones entrelazados que sean robustas, compatibles con operación espacial, y con alto brillo y visibilidad.

En esta tesis se pretende conectar los experimentos de laboratorio en entrelazamiento cuántico y las aplicaciones en entornos operacionales desfavorables en el mundo real. Los principales resultados son:

- Fuentes de fotones entrelazados en polarización de alta eficiencia para la

Resumen

Las correlaciones no locales de sistemas entrelazados son una característica inherente a la teoría cuántica que está fundamentalmente en desacuerdo con nuestra noción intuitiva de realismo y localidad. Además, el entrelazamiento es un recurso esencial en numerosos protocolos de comunicaciones cuánticas, como por ejemplo la teleportación cuántica o la criptografía cuántica, en esquemas metrológicos cuánticos y en computación cuántica. Todos estos esquemas cuánticos permiten mejoras significativas de rendimiento con respecto a sus homólogos clásicos, por lo tanto, parece previsible que en un futuro próximo veamos implementaciones comerciales de protocolos que utilicen fotones entrelazados. Un reto fundamental con el fin de lograr una implementación a escala global del entrelazamiento cuántico es su distribución a grandes distancias.

A pesar de que los fotones son portadores ideales de información cuántica, su distribución a través de largas distancias está significativamente limitada por pérdidas. En la actualidad, las pérdidas introducidas por las fibras ópticas, la atenuación atmosférica, o la dificultad de obtener una línea de visión directa en enlaces terrestres limitan la distribución de entrelazamiento fotónico a varios cientos de kilómetros. La instalación de fuentes de fotones con correlaciones cuánticas en plataformas espaciales permitiría superar tales limitaciones de distancia. Esto no sólo daría lugar a la primera aplicación de protocolos de comunicación cuántica a escala mundial, sino que también daría la oportunidad de llevar a cabo un nuevo tipo de experimentos cuánticos en un marco de la relatividad general.

Las fuentes de fotones entrelazados que podemos encontrar hoy en día en los laboratorios de óptica cuántica no están en general preparadas para ser usadas en entornos hostiles, como podría ser el espacio, ya sea por la utilización de láseres voluminosos, la necesidad de estabilizar interferómetros activamente o simplemente por tener una eficiencia insuficiente. Por lo tanto, un prerrequisito para lograr la implementación experimental de protocolos de comunicación cuántica a través de enlaces satelitales es el desarrollo de fuentes de fotones entrelazados que sean robustas, compatibles con operación espacial, y con alto brillo y visibilidad.

En esta tesis se pretende conectar los experimentos de laboratorio en entrelazamiento cuántico y las aplicaciones en entornos operacionales desfavorables en el mundo real. Los principales resultados son:

- Fuentes de fotones entrelazados en polarización de alta eficiencia para la

distribución de entrelazamiento a través de enlaces en espacio libre de larga distancia. Las fuentes son muy robustas y compactas, y utilizan Ã°nicamente componentes que son compatibles con estrictos requisitos de vuelo y operaciones espaciales.

- Estudio y optimización de las propiedades espectrales y la eficiencia de acoplamiento a fibra monomodo de pares de fotones generados a través de spontaneous parametric down-conversion en titanil fosfato de potasio polarizado periódicamente. Los resultados de estos estudios son de gran importancia para el desarrollo de una fuente de fotones entrelazados ultra-estable y eficiente.

- Desarrollo y caracterización de fuentes de fotones entrelazados en polarización con alta visibilidad ($>$99%) y alto brillo ($>$3 millones de pares detectados por mW de potencia de bombeo). Como resultado del rendimiento obtenido, las fuentes desarrolladas en esta tesis ya están siendo utilizadas en experimentos en curso, como por ejemplo en nanofotónica cuántica y en comunicaciones cuánticas, y serán un elemento esencial en futuras aplicaciones.

Contents

List of Publications

The thesis contains results and discussion of my own work in collaboration with others, which has been published or submitted for publication in peer-reviewed research journals.

Publications included in this thesis

A *A high-brightness source of polarization-entangled photons optimized for applications in free space*
Fabian Steinlechner, Pavel Trojek, Marc Jofre, Henning Weier, Daniel Perez, Thomas Jennewein, Rupert Ursin, John Rarity, Morgan W Mitchell, Juan P Torres, Harald Weinfurter, Valerio Pruneri, Optics Express, Vol. 20, Issue 9, pp. 9640-9649 (2012)

B *Phase-stable source of polarization-entangled photons in a linear double-pass configuration*
Fabian Steinlechner, Sven Ramelow, Marc Jofre, Marta Gilaberte, Thomas Jennewein, Juan. P. Torres, Morgan W. Mitchell, and Valerio Pruneri, Optics Express, Vol. 21, Issue 10, pp. 11943-11951 (2013)

C *Efficient heralding of polarization-entangled photons from type-0 and type-II spontaneous parametric down-conversion in periodically poled $KTiOPO_4$*,
Fabian Steinlechner, Marta Gilaberte, Marc Jofre, Thomas Scheidl, Juan P. Torres, Valerio Pruneri, and Rupert Ursin, Journal of the Optical Society of America B, Vol. 31, Issue 9, pp. 2068-2076 (2014)

D *Efficient fiber-coupling of polarization-entangled photon pairs*
Fabian Steinlechner et al. (in preparation, based on the results presented in Chapter 4)

Other relevant publications and conference contributions

E *True random numbers from amplified quantum vacuum*,
M Jofre, M Curty, F Steinlechner, G Anzolin, JP Torres, MW Mitchell, V Pruneri, Optics Express, Vol. 19, Issue 21, pp. 20665-20672 (2011)

List of Common Abbreviations

BBO	beta barium borate ($\beta-BaB_2O_4$)
dPBS	dual-wavelength polarizing beam splitter
cps	counts per second
cwl	center wavelength
EPS	entangled photon source
DM	dichroic mirror
F	fidelity
FPS	faint laser pulse source
FR	free running
FWHM	full width at half maximum
GEO	geosynchronous Earth orbit
HWP	half-wave plate
i	idler photon
KTP	potassium titanyl phosphate ($KTiOPO_4$)
LD	laser diode
LN	lithium niobate ($LiNbO_3$)
LEO	low Earth orbit
MMF	multi-mode fiber
NIR	near infrared
p	pump photon
PBS	polarizing beam splitter

pp	periodically poled
QPM	quasi-phase matching
QWP	quarter-wave plate
s	signal photon
SMF	single-mode fiber
SPAD	single-photon avalanche diode
SPDC	spontaneous parametric down-conversion
V	visibility
WDM	wavelength division multiplexer
WP	wave plate
YVO	yttrium orthovanadate (YVO_4)

Chapter 1

Introduction

Quantum theory has led to a paradigm shift in our understanding of common-sense notions, such as realism and locality of certain properties of physical objects [1–4]. Unlike physical systems in classical physics, quantum systems can exist in superposition states of mutually exclusive properties that are not defined until measured. The extension of the superposition principle to multi-partite composite systems leads to another peculiarity of quantum theory, known as quantum entanglement. In entangled systems the physical properties of a composite system are shifted from its individual constituents to correlations between them. This leads to nonlocal correlations between possibly distant information carriers, which can be stronger than those allowed by any theory that is based on the assumption that quantum measurements merely uncover pre-determined local properties [5]. This notion is known as local realism, and has been experimentally falsified for entangled systems by violating so-called Bell inequalities [6–11].

The quantum superposition principle and quantum entanglement are not only interesting from a fundamental physics point of view, but also hold enormous technological potential [12]. The efficient generation, manipulation, and transmission of quantum states are thus central issues for both experiments addressing the fundamental nature of the universe and the experimental realization of novel applications such as quantum-enhanced communication protocols.

Quantum communication, or more generally quantum information processing, consists of methods for transmitting, manipulating, and extracting physical information which are based on the principles of quantum theory [13, 14]. These schemes significantly outperform, or completely lack, comparable schemes in classical physics. Some examples of successfully demonstrated quantum-enhanced protocols include quantum teleportation [15, 16], in which the state of a quantum system is transferred from one location to another, quantum computation, which allows certain classes of computational problems to be solved at faster speeds [17], and quantum imaging [18] and quantum metrology for performing ultra-precise measurements [19–21].

An application that has received increased media attention in the recent past is

quantum cryptography. Quantum cryptography [22–27], or more precisely quantum key distribution (QKD), allows communicating parties to generate a set of identical, and completely random secret keys. This set of shared secret keys can subsequently be used as a one-time pad to encrypt and decrypt their messages, thus allowing for unconditionally secure communication over a public channel. The security of quantum cryptography, which relies on the randomness and secrecy of the key, is footed on the very principles of quantum physics. Since information can only be extracted via quantum measurements, which result in uncontrollable changes of the quantum state, the communicating parties can detect the presence of an eavesdropper and discard compromised sections of their set of keys. Quantum key distribution, which has already reached a level of commercial maturity due to its established market opportunity, is the technologically most advanced application of quantum information processing. Another closely related application that promises immediate commercial impact is the physical generation of random numbers. Quantum random number generators use the intrinsic randomness of quantum processes to generate truly random bit sequences at high rates [22, 28, 29].

However, just as transistors, wave-guiding structures, and lasers were the result of fundamental, curiosity-driven research, unlikely to have been geared towards the development of the internet, I believe that the quantum-enhanced applications of the future that will have the largest influence on society are yet to be devised - or will at least occur in a different context than one might expect today.

The wonderful possibilities of quantum communications come with a caveat: quantum information is more fragile than its classical counterpart, and its faithful transmission requires information carriers that can be isolated from decoherence effects induced by the interaction with an uncontrolled environment. The excitations of electromagnetic radiation modes - *photons* - are a particularly attractive system for encoding quantum information as they propagate at the speed of light and interact weakly with the environment, thus permitting coherent transmission of quantum information via optical fiber and free-space links. As in classical communications, it is convenient to encode quantum information in binary photonic degrees of freedom - *qubits*. For the transmission of photons via fibers, qubits are typically encoded using the phase of photons (time-bin encoding), whereas orthonormal-polarization-mode encoding is commonly used in free-space links. The distance over which photonic qubits can be faithfully transmitted is ultimately limited by loss in the transmission channel and noise in the single-photon detectors. In classical fiber-optical communication, amplifiers located along the transmission line can be used to mitigate the effect of loss. As a consequence of the no-cloning theorem [30], however, it is impossible to faithfully copy unknown quantum states. Consequently photonic qubits cannot be amplified in the same simple manner as their classical analogue. This limits the distance over which quantum information can be faithfully distributed via fiber-links to $\sim$300km [31–33]. Quantum repeaters located along the transmission line could circumvent this limitation and allow a faithful distribution without distance limitations [34–38]. They are, however, still in the early stages of development.

An alternative could be the transmission via atmospheric free-space links. For wavelengths in the near infrared the atmospheric absorption loss is significantly lower than that of silica fibers, and link attenuation is mainly the result of beam diffraction and the limited aperture size of transmitting and receiving telescopes. Terrestrial free-space links, however, require a direct line of sight between the transmitter and the receiver, and are thus limited by obstructions and ultimately by the earth's curvature. Thus, in order to fully benefit from free-space propagation, ground-to-satellite, satellite-to-ground, and inter-satellite links are required. Deploying quantum sources, relaying stations, and/or detection hardware on satellites would, for the first time, allow a global-scale implementation of quantum communication protocols. Furthermore, it would provide unique opportunities for both fundamental tests of quantum theory at unprecedented distances, as well as entirely new experiments aimed at a better understanding of the interplay between quantum physics and general relativistic physics. While this might seem like science fiction, a number of advanced experiments over long-distance free-space links (Tab. 1.1), accompanied by several feasibility studies [39–46], have shown that distributing quantum information via satellite links is indeed viable with state-of-the-art technology. Consequently, a number of international research groups in Europe, Singapore, China, USA, and Canada are pursuing projects aimed at bringing quantum experiments to space - The quantum space race has begun.

1.1 Experiments with Entangled Photons in Space

Figure 1.1 depicts a typical experimental scenario for the distribution of entanglement from a transmitter terminal to two receiver stations (Alice and Bob). Before initializing the transfer of quantum information, the transmitter must establish a standard communications channel with Alice and Bob. This classical communications channel is subsequently used to send information about the quantum state and which measurements were performed on a given pair, and forms an integral part of all quantum communications protocols. The quantum source installed on the transmitter emits pairs of photons in a desired entangled state. The photon pairs exhibit strong correlations in time, and entanglement in the degree of freedom in which the quantum information is encoded. The single photons comprising each of these entangled pairs are sent to Alice and Bob via free-space communications links (quantum links). The photons are collected via telescopes at the receiver terminals, where Alice and Bob each perform quantum measurements on their respective photons. The detection time of every arriving photon is recorded using fast single-photon detectors, and detection events that comprise an entangled pair are identified by means of their temporal correlations. The identification of photon pairs by their detection times requires the transmitter and receiver modules to establish and maintain a synchronized time basis, which can be achieved using an external reference, or autonomously via the classical communications link. Once the pair-detection events have been identified, Alice and Bob can reveal their

stronger-than-classical correlations by communicating the outcomes of quantum measurements performed on each photon pair via the classical communications channel.

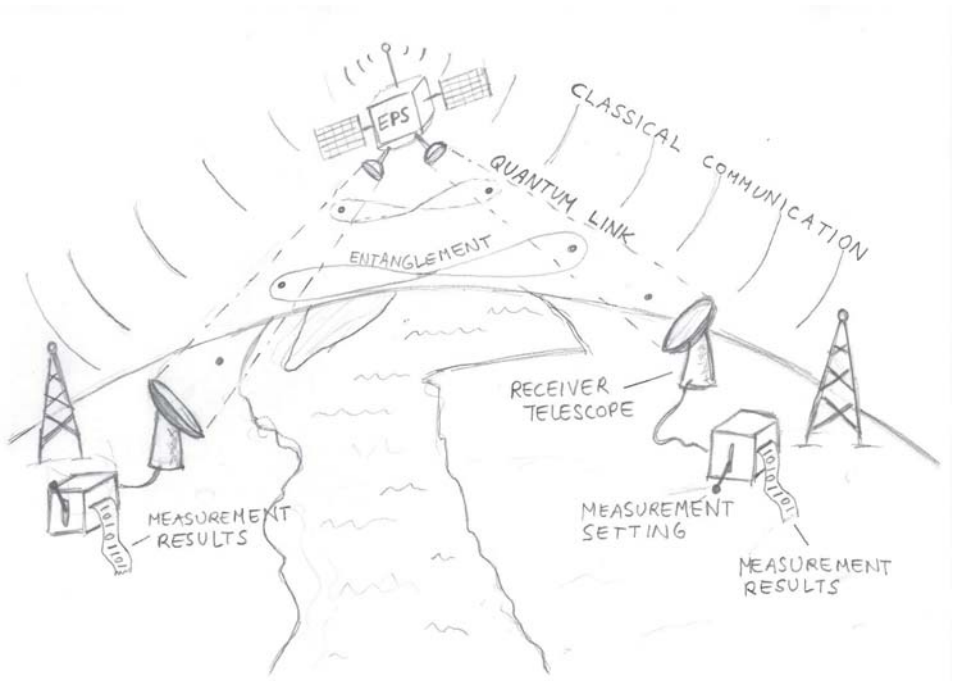

Figure 1.1: Distribution of entangled photon pairs from a quantum transmitter module installed on a satellite to two ground-based receiver modules.

Distributing entangled photon pairs over long-distance links and revealing their quantum correlations is a an immensely challenging task from a technological point of view, in particular due to the fact that, as a result of unavoidable losses in the quantum link, only a fraction of the photons emitted by the transmitter actually arrive at the receiver modules. The main sources contributing to losses along the optical transmission channel are atmospheric absorption and scattering, on the one hand, and diffraction, telescope pointing errors, and atmospheric turbulence, which all lead to beam broadening and thus limit the fraction of photons collected by the receiver aperture, on the other.

Achieving experimentally feasible pair-detection rates thus requires a large number of photon pairs to be emitted from the transmitter, as well as minimizing losses in the transmission channel (e.g. advanced tracking techniques in order to minimize beam wander and telescope pointing errors) and the receivers (e.g. the use of efficient single-photon detectors). Note that, since correlated photon pairs are identified by their arrival times, there is an upper limit to how effective the source rate can mitigate against link loss. Once the average time between two successive pair emissions at the source decreases below the timing resolution of the detectors and/or the precision of synchronization of the respective clocks, suc-

cessive pairs emitted by the source can no longer be distinguished, which leads to an increased number of so-called accidental coincidence counts. These accidental coincidences stem from un-correlated photon pairs, and thus diminish the quality of entanglement observed.

Additionally, the quantum correlations of the attenuated photon streams arriving at the receiver modules are masked by the detection of uncorrelated background photons and intrinsic noise in the single-photon detectors (dark counts). As a result, achieving an acceptable signal-to-noise ratio (i.e. fringe visibility) requires the entangled photons to be well-isolated from spurious background counts, which can be achieved by employing narrowband spectral filters (passband $<$1nm), spatial filtering (i.e. minimizing the detectors' field of view), and temporal filtering techniques, which in turn requires precise and stable timing synchronization of transmitter and receiver modules.

Detecting the desired quantum correlations also requires the transmitter to continuously emit photons in a well-defined, maximally entangled state, as well as the continuous compensation of transformations induced by changes in the quantum links, receivers, and transmitter [59, 62].

1.1.1 Mission scenarios for quantum entanglement in space

The installation of quantum transmitter modules and/or receiver modules on space platforms will enable a wide range of experiments in space. Currently envisaged experimental scenarios could involve transmitter/receiver modules in space and/or on the ground, and distribute quantum entanglement from ground to satellites - in Low Earth (LEO), Mid Earth (MEO), or geosynchronous orbit (GEO) - from satellites in GEO/LEO/MEO to ground, or via inter-satellite links. Future missions may also extend to scenarios involving Moon-Earth/Moon-Mars links with a suitable source of entangled photons placed symmetrically or asymmetrically between the two receiving locations.

Ambitious long-term projects could also invoke quantum relaying satellites capable of performing Bell-state analysis on photons received from independent entangled photon sources (entanglement swapping [63]). If such relaying stations were additionally equipped with quantum memories [64–67], this would enable a satellite-based quantum repeater infrastructure which could extend the distance limitations in quantum communications to unimaginable distances [34–38]. In order to perform Bell-state analysis on photons from independent sources, however, requires the photons received to be indistinguishable in time - i.e. the arrival time of the photons must be synchronized to within the coherence time of the photons [68, 69]. This can be achieved either by synchronizing pair-generation time in the two sources, or with sources that have extremely long coherence times [70–73](i.e. narrow bandwidth) and ultra-fast detectors. The significant technological effort of such a relaying station combined with the fact that quantum memories are still in the first stages of development, however, make such a scenario highly unlikely to occur in the near future.

Quantum correlations in presence of loss and background noise

As outlined in the previous section, one of the fundamental challenges in the realization of quantum experiments in space is overcoming the significant loss in the transmission channel. Figures 1.2 and 1.3 depict the expected detected pair rate and correlation visibility as a function of the total loss accumulated along the transmission channel for various levels of background noise. Figure 1.2 assumes a two-link scenario with the transmitter located symmetrically between the two receivers, such that both photons experience the same attenuation factors (dual-link scenario). In Fig. 1.3 one of the receiver modules is integrated into the transmitter module, and only one photon is subject to attenuation. The plots assume a module detection efficiency of 20%, a temporal resolution of 1 ns, and an emitted pair rate of 10^7cps. The simplified model used for the calculations is described in Chapter 2. The comparison of the single-link and dual-link scenarios in Fig. 1.2 and Fig. 1.3 clearly shows that the latter case is more resilient with respect to loss and background noise. In order to fully exploit the nonlocal correlations of entangled photons and extend quantum correlations to largest possible distances, the transmitter should thus be located symmetrically between the two receivers. In the first stage of proof-of-concept experiments, however, one of the receivers may also be included in the transmitter module, which has the obvious advantage that only a single quantum communications link must be established.

Expected link loss in various mission scenarios

Table 1.2 lists the estimated losses in quantum communications links between ground and satellites in LEO ($\sim$500km altitude) and GEO ($\sim$36000km altitude) for various scenarios. Notice that the loss in satellite-to-ground links is significantly lower than that in ground-to-satellite links. This asymmetry is a result of the differing impact of turbulence in the lower atmosphere for the two cases; turbulent layers close to the emitter result in more severe beam distortions than those close to the receiver telescope (so-called shower curtain effect), which leads to a larger effective beam diameter and correspondingly higher link loss.

Comparing the expected loss (Tab. 1.2) with the modelled behavior in the presence of noise (Fig. 1.2 and Fig. 1.3), we see that quantum communications with satellites is possible in a variety of configurations. While maintaining a link with a LEO satellite is more challenging than in the case of a GEO satellite, the significantly lower loss for both uplink and downlink scenarios, together with the lower costs of launching a dedicated LEO satellite, suggest that the first proof-of-principle experiments will involve LEO-to-ground, or ground-to-LEO links.

1.1.2 Proposals for quantum experiments with LEO satellites

A number of international research projects aimed at experiments on LEO space-platforms have been launched around the globe:

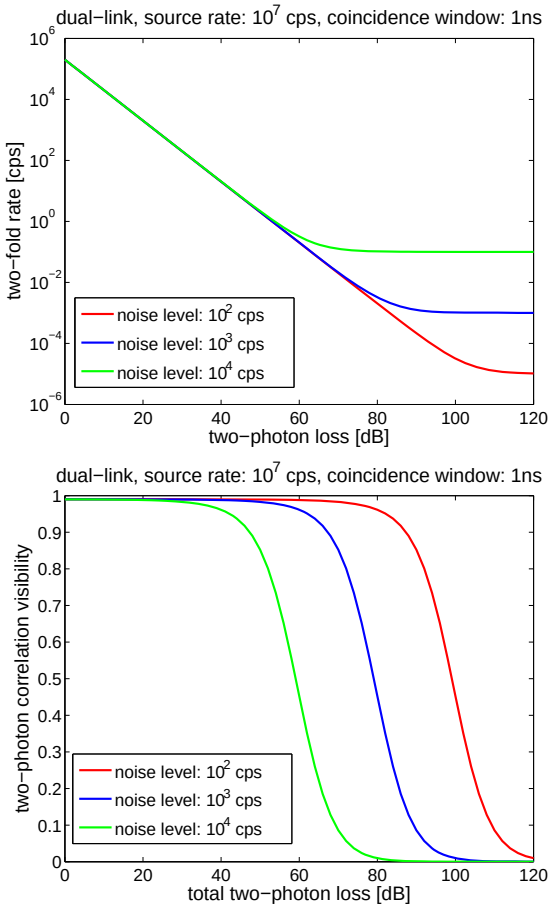

Figure 1.2: Detected pair rate and correlation visibility as a function of link loss, for various background count levels. The source is assumed to be located symmetrically between the two receiver modules, such that each photon of the entangled pair experiences approximately the same link loss. I have assumed a local source pair rate of 10^7, a timing resolution of 1 ns, and a receiver module efficiency of 0.2.

Space-QUEST

The Space-QUEST (QUantum Entanglement for Space experimenTs) proposal [74] aims at installing a full quantum transceiver module, consisting of an entangled photon source, a faint laser pulse source[1] [76], detection modules, and two transmitter telescopes, on the Columbus module at the international space station (ISS). The declared goal is to distribute entangled photons to distant ground stations via two simultaneous downlinks and to perform tests of quantum theory at unprecedented distances, as well as global-scale quantum key distribution. This latter objective could also be accomplished using two successive downlinks, and

[1] A faint laser pulse source (FPS) emits on average less than one photon per pulse, and can be used for decoy state quantum key distribution [75].

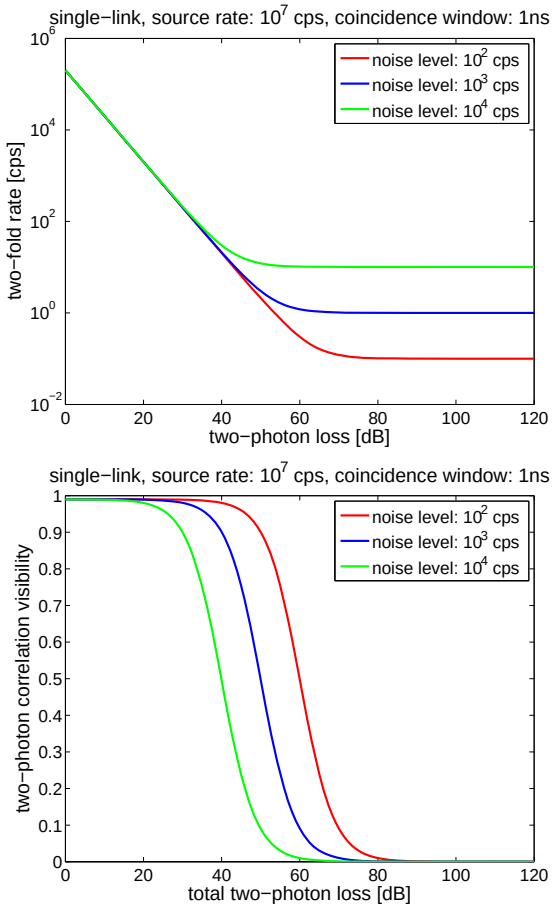

Figure 1.3: Detected pair rate and correlation visibility as a function of link loss, for various background count levels. One of the detection modules is incorporated into the transmitter module, such that only one photon of the entangled pair experiences link loss. I have assumed a local source pair rate of 10^7, a timing resolution of 1 ns, and a receiver module efficiency of 0.2.

independently generating cryptographic keys with two distant ground stations. The two ground stations could then establish a shared key known only to themselves and the satellite service provider, by publicly announcing the XOR value of the two independently generated secret keys.

The realization of such an experiment would require an efficient quantum communications terminal, subject to highly restrictive requirements in terms of mass, dimensions, stability, and power consumption [41].

Chinese Quantum Science Satellite

The Quantum Science Satellite project lead by the Chinese Academy of Sciences and the Hefei National Laboratory for Physical Sciences aims at installing a quan-

tum communications terminal onboard a dedicated satellite platform. The project foresees the launch of a microsatellite (10-100 kg) into a 600-km altitude orbit. The microsatellite will be equipped with a full quantum communications payload, consisting of an entangled photon source, a faint pulse laser source for QKD, detection hardware, and transmitter telescopes with tracking capabilities. The mission duration is estimated at two years, over which a series of downlinks with dedicated ground stations distributed in China and around the globe will be established. The project goals involve tests of fundamental quantum principles and quantum communication protocols over record distances. The building and testing activities of the dedicated microsatellite and its payload are estimated to conclude in the summer of 2015.

Ground-to-ISS uplink

Another recent proposal involving the ISS advocates the distribution of an entangled photon from ground to space via a single ground-to-space link, while its partner photon is detected locally on the ground. This scenario requires a space-proof polarization-detection module, whereby the most critical components, space-qualified single-photon detectors, have already been demonstrated [77, 78]. Another benefit of the proposal is that the ISS is already equipped with a large-diameter objective lens with tracking capabilities, which can be mounted in front of a glass viewing panel and is accessible from inside the ISS. As a first proof-of-principle demonstration, they propose performing a Bell-type experiment between ground and space. The realization of such an experiment would require a suitable single-photon polarization analyzer module to be developed and subsequently launched to the ISS, where it would be installed in place of the camera body currently attached to the objective lens. The more complex optical components, such as a highly efficient entangled photon source and a module for compensating polarization measurements for relative rotations between satellite and ground stations, could remain on the ground.

The QEYSSAT mission proposal

Researchers at the Institute of Quantum Computing at the University of Waterloo are currently developing a microsatellite mission concept for the Canadian Space Agency (CSA). The QEYSSat (Quantum EncrYption and Science Satellite) proposal [79] aims at establishing an ground-to-satellite link between a quantum emitter on ground and a detection module installed on a microsatellite. The microsatellite will be launched into a 600-km orbit, and will be designed for a two-year lifetime. The declared mission objectives are the generation of cryptographic keys between two ground stations via successive uplinks, as well as fundamental physics experiments involving entangled photons.

Experiments with nano-satellites

Researchers at the Centre for Quantum Technologies at the National University of Singapore have devised another cost-efficient way of testing quantum hardware under space conditions [80]. They propose launching a polarization-entangled photon source into LEO on board a CubeSat, and testing its functionality under space conditions. A CubeSat is a miniaturized satellite with standardized volume and mass restrictions (10 cm cube, $\leq$ 1.33 kg), and is the most cost-effective means of launching a quantum payload into LEO. In contrast to the two aforementioned proposals, this proposal does not foresee the entangled photons to be transmitted from the source to distant receivers. In a first step the single-photon polarization analysis would be integrated into the payload, and quantum correlations would be directly verified on board the satellite.

Faint pulse QKD with LEO satellites at Los Alamos

Researchers at the Los Alamos National Laboratory are also pursuing experiments involving downlinks from quantum transmitters installed on LEO satellites. To the best of my knowledge, however, the mission scenarios currently pursued do not involve entangled photon sources and are geared towards the implementation of decoy state QKD protocols with faint laser pulse sources.

1.2 Entangled Photon Sources for Quantum Communications in Space

The generation of entangled photon pairs in a laboratory environment has become a routine task for experimentalists around the globe [81], and research and development now focus mainly on the optimization of the performance characteristics of the sources.

The quality of an entangled photon source is commonly characterized by its brightness (i.e. the number of generated pairs per mW of pump power), the spectral bandwidth over which the photons are generated, and the purity, or visibility, of the entangled state.

Several schemes for the generation of photon pairs exist, but at present the most widely used and versatile method is spontaneous parametric down-conversion (SPDC) in second-order nonlinear crystals. Recent developments in the field have resulted in rapidly increasing source efficiency over the past few years. Figure 1.4 depicts the development of source brightness over time.

While numerous sources of entangled photon pairs have been shown to work well under laboratory conditions, the demands regarding misalignment tolerances, mechanical stability, and temperature control remain high. Improving the long-term stability and ruggedness, while maintaining a compact footprint and minimizing power consumption, are key challenges to be addressed in the development

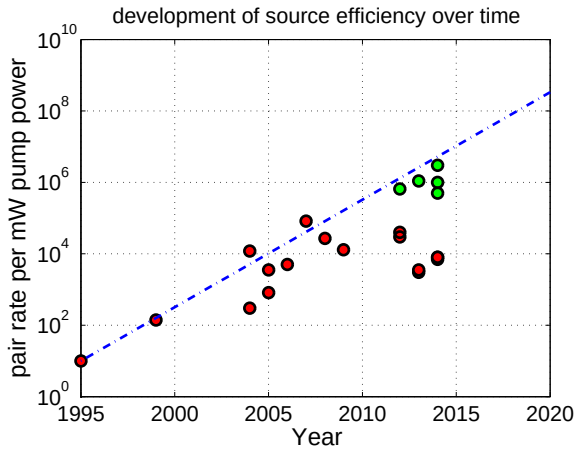

Figure 1.4: Development of efficiency of polarization-entangled photon sources based on bulk SPDC from 1995 to the present day. The red data points denote the prior state of the art. The green data points denote sources developed in the course of this thesis. For a detailed comparison refer to Appendix A. The blue trend line shows a yearly doubling of source pair rate since 1995.

of space-proof sources of entangled photons. However, with experiments incorporating entangled photons rapidly expanding to other fields of research, such as biology and telecom engineering, interest in field-deployable sources is not only limited to applications in space. Additional criteria which must be addressed in order to extend the usage of entangled photons beyond quantum optics laboratories, and enable possible commercial applications, are ease of operation and the number, cost and complexity of optical components required to build the source.

Figure 1.5 lists a number of factors that have influenced design parameters chosen for the sources developed in the course of this thesis. These are discussed in more detail in the following paragraphs.

1.2.1 Encoding quantum information

Quantum information can be encoded in various degrees of freedom of photons. A number of possible approaches are listed in Tab. 1.3 with a short discussion about the respective advantages and disadvantages regarding applications in free space. The type of encoding of quantum information pursued in this thesis is the polarization of single photons, as polarization qubits have been shown to be largely unaffected by transmission through turbulent atmospheric free-space links. Furthermore, polarization qubits can be conveniently detected and manipulated using only simple optical devices such as wave plates and polarizers, likely to be space-qualifiable and thus compatible with both ground-based and space-based detection modules and sources.

One of the main challenges with regard to applications under harsh operational conditions is the temperature dependence of birefringent optical elements. This

could be addressed by athermalizing the optimal design by implementing an appropriate combination of birefringent materials.

1.2.2 Pair-generation mechanisms

A space-suitable source of polarization-entangled photons requires a reliable and highly efficient pair-generation process. The present-day gold standard, and by far the most mature method for generating polarization-entangled photon pairs, is spontaneous parametric down-conversion (SPDC) in nonlinear materials. This makes SPDC the most viable candidate for implementation into the first generation of space applications. On the long run, however, alternative emergent technologies, most notably four-wave mixing in nonlinear fibers, and solid-state sources are promising candidates for further improvements in terms of performance.

Spontaneous parametric down-conversion

SPDC is a quantum mechanical process that occurs in non-centro-symmetric second-order nonlinear crystals (e.g. BBO, LBO, KTP, or LN), in which a strong pump field (p) can induce the spontaneous emission of two lower-energy photons, commonly termed signal (s) and idler (i) photons. Unlike an ideal "photon pair gun" that deterministically generates photon pairs, SPDC is a fundamentally probabilistic process that exhibits typical photon pair-generation probabilities of $< 10^{-9}$ per pump photon. Consequently, the signal and idler fields are in their respective vacuum states the majority of the time and the correlations of entangled photon pairs can only be revealed after their detection (post-selection). Due to the random emission characteristics, there is also always a finite probability of emitting more than one photon pair in a given time window. This leads to accidental coincidence counts which reduce the quality of the entangled two-photon state. Regardless of such limitations, probabilistic pair generation via SPDC remains the most widely used approach, owing mainly to the relative simplicity and versatility of the process. A myriad of different two-photon quantum states can be generated with high-visibility quantum correlations in various degrees of freedom [23, 83–87]. This has allowed for the performance of fundamental tests of quantum theory, as well as the implementation of diverse applications in quantum optics.

Depending on the polarizations of the interacting fields, one distinguishes between type-0, type-I and type-II SPDC, whereby type-I and II processes involve orthogonally polarized fields, whereas in type-0 processes all photons are co-polarized. In the first generation of type-II SPDC based sources [83], correlations in energy and momentum were exploited to generate polarization-entangled photons in restricted spatial regions. The pair-collection efficiency was improved by overlapping type-I emission cones from separate crystals [88]. The scheme was, however, limited to relatively short crystals due to the non-collinear configuration. A significant increase in pair rate was achieved with a collinear non-degenerate configuration, which allowed the entangled photons to be efficiently coupled into single-

mode fibers [89]. Further improvements were subsequently achieved in sources that made use of periodically poled materials [90–92] (see Fig. 1.4 and Appendix A for a comparison).

Current developments in waveguide technology also present an attractive option for fully integrated entangled photon sources based on SPDC [72, 93–100] and promise significantly higher pair-generation efficiency[2]. A fully integrated solution is highly appealing as it could significantly reduce problems with mechanical stability. The achievable reduction in size (including temperature control and electronics etc.), however, is unlikely to be significant compared to a well-designed bulk optics solution.

At present, sources based on SPDC in bulk crystals are the most suitable candidate to meet the challenging performance requirements in terms of versatility, stability, fiber-coupling efficiency, visibility, and pair-detection rates for application in high-loss free-space links.

Four-wave mixing

Four-wave mixing (FWM) [101] is a third-order nonlinear process, in which two pump photons of a strong pump laser spontaneously produce a signal and idler pair. Four-wave mixing is mediated by the third-order nonlinearity $\chi^{(3)}$, and occurs naturally in many optical materials, in particular waveguiding structures such as single-mode fibers [102–106], highly nonlinear photonic-crystal fibers [107–110], or nanoscale silicon waveguides [111–114]. In-fiber sources based on four-wave mixing can exhibit very high brightness and ultra-narrow bandwidths as a result of the long interaction lengths and the confinement to a single spatial mode. High-fidelity polarization entanglement has been achieved in a fiber Sagnac geometry [115, 116], and an all-fiber solution would be a significant advantage in terms of mechanical stability. A significant drawback in four-wave mixing is the high level of linear background noise due to spontaneous Raman scattering. At present, high signal-to-noise ratios are typically achieved at low temperatures and with picosecond-pulsed pump sources. Nevertheless, fully integrated on-chip sources with suitable input and output coupling are likely to become a viable solution in the near future.

Solid state sources

Solid state sources are a promising candidate for generating entangled photon pairs on demand [117, 118]. In solid state sources, an excitation pulse prepares a quantum dot in a biexciton state (electron-hole pairs with opposite spin). As the electron-hole pairs recombine, two photons are emitted following one of two possible relaxation cascades. The circular polarizations of the emitted photons are anti-correlated due to the conservation of spin. If the two relaxation channels can be

[2] Note, that high brightness, and high entanglement visibility are yet to be demonstrated simultaneously in a wave-guide-based source of polarization-entangled photons around 810nm.

made indistinguishable then the procedure yields a pair of photons in a maximally polarization-entangled state. In contrast to the spontaneous parametric processes, the biexciton decay produces triggered photon pairs with, in an ideal quantum dot, two photons per excitation pulse.

The main drawback with solid state sources is the low demonstrated entanglement visibility of only $\sim$ 70% [119, 120]. This is a consequence of structural imperfections which result in a polarization dependent intermediate exciton level and lead to decoherence of the entangled state. Another limitation of solid state sources is that, at present, they require operation at cryogenic temperatures ($<$20K).

The on-demand generation of photon pairs is definitely a great advantage of solid state sources over sources based on spontaneous parametric processes. However, in order for solid-state sources to become a viable alternative to SPDC, it will be necessary to overcome difficulties in the repeatable production of symmetric quantum dots, and to demonstrate a higher degree of entanglement.

1.2.3 Wavelength considerations

The ideal operational wavelength for space-suitable entangled photon sources depends on a number of factors, such as available atmospheric transmission windows, single-photon detection efficiency, beam diffraction, and the availability of space-proof optical components, as well as the wavelength range addressable via the SPDC process.

Single-photon detectors and optical components

The vast majority of experiments with polarization-entangled photon pairs operate in the wavelength range between 700-850 nm, or in the telecom windows around 1300nm and 1550nm. The first wavelength range is motivated mainly by the responsivity of silicon-based single-photon avalanche diodes (SPADs) in this region. Silicon SPADs can exhibit timing jitters as low as $<$0.05 ns [121], dead times of only a few ns, low intrinsic dark counts $<$10 cps, and photon-detection capability ranging from 400-1000nm, with peak detection efficiencies as high as $>$70%. Furthermore, space-qualified silicon SPADs have already been demonstrated [77].

Operation at 1300nm or 1550nm is used in classical fiber-based telecom systems, and is motivated by the dispersive and transmittive properties of silica fibers. Working in this wavelength range thus has the benefit of an increased number of commercially available fiber-based products. The main disadvantage is that single-photon detection in the NIR (900nm to 1700nm) region requires InGaAs/InP SPADs, which are more prone to internal noise ($>$5000 cps) and are less efficient ($<$25%) than silicon SPADs. While the increased number of commercial, and possibly already space-proof, components is an appealing argument for operation in the 1550nm region, this benefit is outweighed by the better performance characteristics of silicon SPADs for shorter wavelengths.

At present there are various efforts towards improving photon-counting technology and methodology.

Superconducting transition-edge sensors (TES) [122–126], for example, are highly sensitive bolometers that can detect single-photons over a wide range of wavelengths. TES are becoming increasingly popular in quantum optics experiments, as they exhibit unprecedented detection efficiencies (>95%), negligible intrinsic dark count rates, and the capability of discriminating between single-photon and multi-photon detection events. However, compared to off-the-shelf SPADs they exhibit long dead times ($\sim 1\mu$s), and low timing accuracy ($\sim$100 ns), and require operation in a cryogenic environment.

Single-photon detectors based on superconducting nanowires (SSPDs) [127–131] are another promising technology, as they offer high efficiency (>70%), low dark counts, and very good timing resolution (<50ps) over a wide wavelength range. Their compatibility with free-space receivers, however, is unclear, because of the requirement for single-mode coupling into the detector.

Atmospheric transmission windows

Since the most probable mission scenarios include free-space transmission through earth's atmosphere, the atmospheric transmission properties are another factor to be considered. Specifically, within the responsivity range of silicon and InGaAs SPADs, the bands 400nm-650nm, 730nm-750nm, 770nm-870nm, 1000nm-1100nm, 1170nm-1300nm, and 1500nm-1700nm are 900nm are clear of strong absorption resonances, whereby a slight increase in transmittance is observed as the wavelength increases.

Diffraction and turbulence

The effective aperture of receiving telescopes leads to another loss mechanism: beam broadening due to diffraction and atmospheric turbulence. Diffraction loss can be minimized by utilizing shorter wavelengths and/or larger diameter transmitter telescopes, and becomes the main source of loss for inter-satellite, and satellite downlink experiments. Note that, in an uplink scenario, atmospheric turbulence becomes the dominant factor once the transmitter diameter extends beyond a certain length and thus limits the extent to which increasing the sender aperture can mitigate diffractive broadening.

Pump sources for SPDC

Numerous laser technologies produce coherent radiation suitable for pumping the SPDC emission process. Semiconductor laser diodes (LD) are the preferred choice as they present a well-rounded trade-off between complexity, volume occupation, and performance.

Laser diodes are currently not available at wavelengths below 400nm. Consequently, the wavelength of signal and idler photons generated via SPDC must be

centered around wavelengths above 800nm. Shorter wavelengths could be generated by doubling the frequency of the radiation emitted by a 700nm LD pump, for example, but this would come at the significant cost of added complexity.

Conclusion on wavelength selection

Taking into account all these factors leads to the conclusion that a source producing SPDC photons between 750 nm and 850 nm is currently the best choice for a flexible space-suitable source of entangled photons.

1.3 Thesis Objectives

This thesis is dedicated to the development of highly efficient sources of polarization-entangled photons for future integration into fully space-proof prototypes. To this end the main objectives of this thesis are:

- Design of highly efficient sources of polarization-entangled photon pairs for the distribution of entanglement via long-distance free-space links. The main constraints are robustness and compactness, requiring the use of only components compliant with the severe requirements of space flight and operation.
- Detailed study of photon-pair-generation efficiency, spectral and spatial properties of photon pairs generated via SPDC in bulk periodically poled potassium titanyl phosphate (ppKTP):

  Experimental comparison of collinear type-0 and type-II quasi-phase-matching configurations in ppKTP.

  Evaluation of pair-generation efficiency and spectral properties of SPDC, pumped with continuous-wave and free-running laser diodes and resulting conclusions for space-based sources of entangled photons.

  Study of single-mode fiber-coupling efficiency and spectral characteristics of SPDC photon pairs after mode-projection, and subsequent corroboration of theoretical results in experimental test setup.
- Development and characterization of efficient field-deployable polarization-entangled photon sources which exhibit unprecedented performance (see comparative table in Appendix A) in terms of pair-detection rates and entanglement visibility:

  Engineering of high-brightness and high-visibility entangled photon source within the framework EQUO project (ESA/ESTEC contract 22542/09/NL/SFe) and delivery of compact breadboard source to ESA. The baseline approach for this project is a non-degenerate crossed-crystal configuration in ppKTP.

  Development of entangled photon source based on a novel “folded sandwich” configuration, which uses a single nonlinear crystal in a linear bi-directional double-pass interferometer.

Demonstration of high-heralding-efficiency source of polarization-entangled photons in the 810-nm region, based on type-0 and type-II Sagnac loop configurations.

1.4 Thesis Outline

The thesis is structured as follows:

Chapter 2 gives a brief overview of the relevant concepts of quantum theory with the main emphasis on encoding and measuring qubits encoded in the polarization of single photons, as well as the generation of polarization-entangled photon pairs via SPDC in nonlinear crystals. Chapter 3 covers a detailed study of the pair yield and the spectral properties of photon pairs generated via SPDC in ppKTP. The material presented in Chapter 3 was published as a part of Publication C. Chapter 4 addresses the single-mode fiber coupling of SPDC photon pairs. A publication based on the material presented in this chapter is in preparation (Publication D). In Chapter 5 I discuss the design and characterization of a highly efficient source of polarization-entangled photons. The source was developed as part of the ESA-funded EQUO project, and the results were published in Publication A. In Chapter 6 I present a novel source of polarization-entangled photons that evolved from the EQUO source. A number of practical improvements were implemented in this source, which resulted in higher brightness and Bell-state fidelity. The results were published in Publication B. Chapter 7 discusses the results achieved in a source of polarization-entangled photons which was optimized with regard to heralding efficiency. The results presented in Chapter 7 were published together with the spectral characterization of SPDC in ppKTP (Chapter 3) in Publication C. The main results of this thesis, together with a brief outlook on potential future developments, are summarized in Chapter 8.

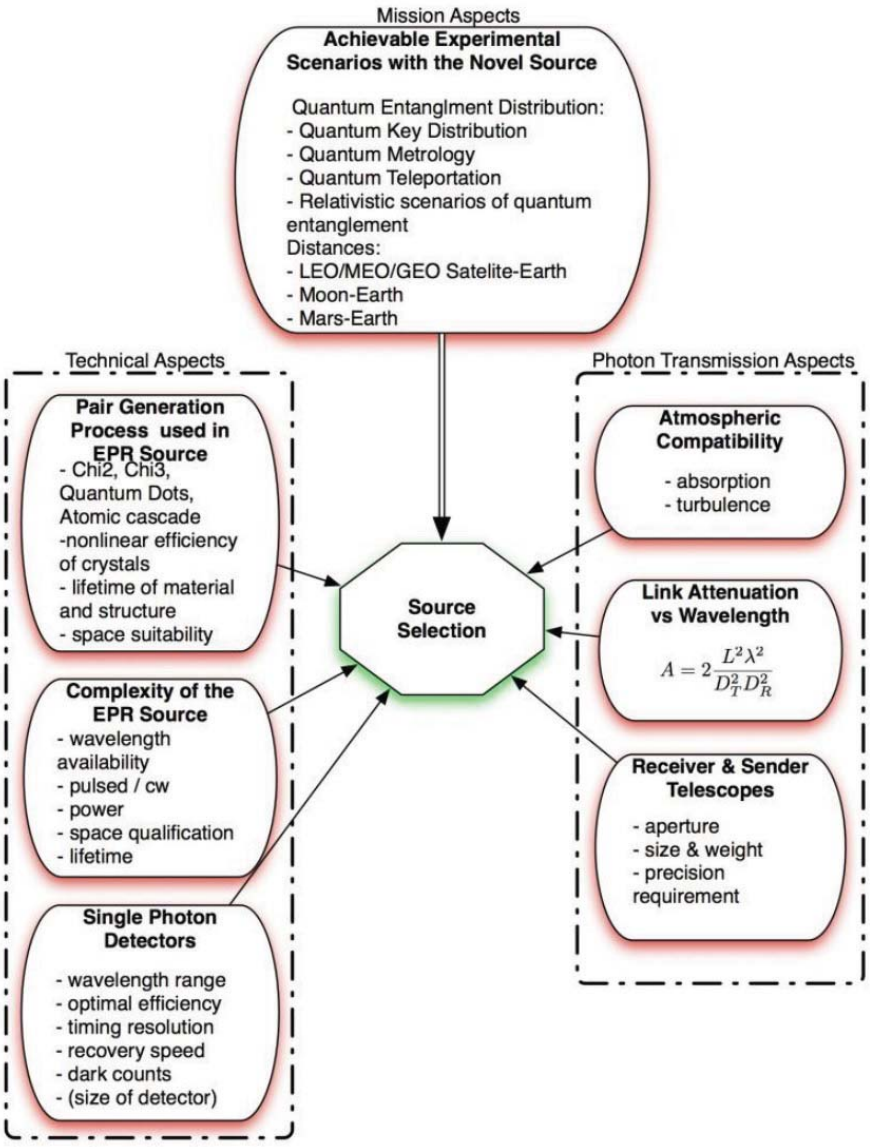

Figure 1.5: Considerations for the design of an optimal source of entangled photons for applications in space. Image copied from [132].

Distance (Location)	Experimental Achievement	Reference
0.6km (Vienna)	Long-Distance Free-Space Distribution of Entangled Photons	Aspelmeyer et al. 2003 [47]
7.8km (Vienna)	Distributing entanglement and single photons through an intra-city free-space quantum channel	Resch et al. (2005) [48]
13km (Hefei, China)	Free-Space Distribution of Entangled Photon Pairs over 13-km	Peng et al. (2005) [49]
1.5 km (Singapore)	Free-space Quantum Key Distribution with entangled photons	Marcikic et al. (2006) [50]
144 km (Canary Islands)	Experimental Demonstration of Free-Space Decoy-State Quantum Key Distribution	Schmitt-Manderbach et al. (2007) [51]
144 km (Canary Islands)	Entanglement-based quantum communication over 144 km	Ursin et al. (2007) [52]
6000 km (Matera)	Experimental demonstration of a quantum communication channel from a LEO satellite to Earth	Villoresi et al. (2008) [42]
1.5 km (Waterloo, Canada)	Entangled quantum key distribution over two free-space links	Erven et al. (2008) [53]
350m (Singapore)	Daylight operation of a free space, entanglement-based quantum key distribution system	Peloso et al. (2009) [54]
144 km (Canary Islands)	Transmission of entanglement over a 64-dB free-space channel	Fedrizzi et al. (2009) [55]
16 km (Huailai)	Experimental demonstration of free-space quantum teleportation	Jin et al. (2010) [56]
144 km (Canary Islands)	Violation of CHSH inequality while closing freedom of choice loophole	Scheidl et al. (2010) [57]
143 km (Canary Islands)	Quantum teleportation over 143 kilometres using active feed-forward	Ma et al. (2012) [58]
20 km (Germany)	Air-to-ground quantum communication with airplane moving at 290 km/h	Nauerth et al. (2013) [59]
1.6 km (Erlangen)	Atmospheric continuous-variable quantum communication	Heim et al. (2014) [60]
$\sim$ 0.7km (Waterloo)	Demonstration of three-photon quantum nonlocality	Erven et al. (2014) [61]

Table 1.1: List of long-distance quantum communications experiments utilizing free-space links, which demonstrate the feasibility of satellite-link experiments.

800nm 1550nm	ground-based receiver	LEO receiver	GEO receiver
ground-based transmitter	-	27.4dB 26.3dB	64.5dB 63.4dB
LEO transmitter	6.4dB 12.2dB	28.5dB 33.6dB	52.9dB 58.6dB
GEO transmitter	43.6dB 49.3dB	52.9dB 58.6dB	53.9dB 59.7dB

Table 1.2: Link attenuation in various space scenarios, reproduced from [40]. The losses listed assume a ground-based telescope aperture of 1m, a space-based aperture diameter of 30cm, weak atmospheric turbulence, and operation under excellent sight conditions. For a detailed list of all assumptions involved, refer to [40].

Degree of freedom	Behavior in free-space link	Experimental advantage	Experimental challenge
Polarization	Well-tested under turbulent atmospheric conditions.	Detection and manipulation (wave plates) straightforward. Polarization correlations independent of spatial mode.	Alignment and temperature-dependence of birefringent elements in sender and receiver. Requires compensation of relative rotations of the sender and receiver.
Relative phase/time-bin	Not tested under turbulent atmospheric conditions, but should work in principle.	Only one polarization required, possibly of relative orientation.	Active stabilization of two unbalanced interferometers at the source and the receivers. High visibility only in single spatial mode.
Spatial mode	Not expected to work well under strong turbulent atmospheric conditions due to wave-front distortion.	No polarization dependence. High dimensionality (channel capacity).	Perfect compensation of wave-front distortions, and accurate pointing required.
Continuous Variables (quadrature encoding)	Has been demonstratede under turbulent atmospheric conditions.	Robust with respect to background. Sources and detection modules well-developed from classical communications.	Loss-tolerance currently below anticipated efficiency of free-space satellite link.

Table 1.3: Examples of degrees of freedom for encoding photonic quantum information. Table modified from [82].

Chapter 2

Fundamentals of Quantum Entanglement

In classical communications, the elementary unit of information is the "bit", a binary variable with the values "0" or "1". Physically, bits may be encoded in systems that have two clearly distinguishable states - from the "heads" and "tails" of a coin to the "0" and "π" phase difference between successive light pulses, as used in the glass fibers that form the backbone of the Internet. Quantum communications is the extension from classical systems to quantum systems, and its power is rooted in linearity of quantum theory and the existence of superpositions of quantum bits - *qubits*. When multiple qubits exist in a simultaneous superposition state, the system is *entangled*. In an entangled state, the constituent particles are intimately correlated and their entangled nature can be preserved over large distances. These nonlocal correlations are stronger than any classically permissible correlations, and lie at the heart of quantum theory and many of its applications.

In this chapter I outline the basic principles behind the manipulation and measurement of qubits encoded in the polarization of single photons, and the generation of pairs of polarization-entangled photons via the process of spontaneous parametric down conversion. The underlying theory, which has been extensively studied in the literature, is reviewed in a formalism which is particularly suitable for the interpretation of the results presented in the later chapters of the thesis. I will make no effort at achieving great mathematical rigor and refer to the standard quantum optics textbooks [133–138] for a more in-depth introduction.

2.1 Basic Concepts

Quantum state vector The state of a quantum system is completely described by a state vector $|\psi\rangle$ embedded in a linear unitary vector space (Hilbert Space $\mathcal{H}$). If two orthogonal vectors $|\psi_1\rangle$ and $|\psi_2\rangle$ ($\langle\psi_1|\psi_2\rangle = 0$) are possible states of the

quantum system then so is the coherent superposition state:

$$|\psi\rangle = \alpha|\psi_1\rangle + \beta|\psi_2\rangle \tag{2.1}$$

where $\alpha^*\alpha + \beta^*\beta = 1$. When a physical system can be described by means of a state vector, it is said to be in a pure state. This implies that the states $|\psi_1\rangle$ and $|\psi_2\rangle$ be decoupled from, i.e. identical in, any other degrees of freedom. Any correlations with uncontrolled external degrees of freedom reduce the purity of the superposition state.

States that cannot be described by state vectors are known as mixed states. In this case there remains some uncertainty in the preparation procedure, and the physical system is described by means of a density operator.

Density matrix The density operator describing a mixed state can be written as a sum of orthogonal projection operators $|\psi_i\rangle\langle\psi_i|$:

$$\hat{\rho} = \sum_i p_i |\psi_i\rangle\langle\psi_i| \tag{2.2}$$

where $p_i > 0$ ($\sum_i p_i = 1$) is the probability with which the system resides in the pure state $|\psi_i\rangle$. For pure quantum state vectors the density matrix reduces to the projection operator $|\psi_j\rangle\langle\psi_j|$, such that the relation $\hat{\rho}^2 = \hat{\rho}$ holds. In general, the degree of mixedness is quantified by the purity:

$$\mathscr{P}(\hat{\rho}) = \mathrm{Tr}\big(\hat{\rho}^2\big) \tag{2.3}$$

The purity is one for a pure state and $1/N$ for a maximally mixed state of dimension N.

Quantum measurements Assume an experimenter has an ensemble of identically prepared systems, each in a state $|\psi\rangle$, and performs a quantum measurement of an observable physical quantity on each system. In quantum theory, measurable quantities are described by means of Hermitian operators $\hat{\mathcal{M}}$, whereby the operators' real eigenvalues correspond to possible measurement outcomes. Hermitian operators can be decomposed in terms of orthogonal projection operators ($\hat{\Pi}_i = |m_i\rangle\langle m_i|$):

$$\hat{\mathcal{M}} = \sum_i m_i \hat{\Pi}_i \tag{2.4}$$

These projection operators fulfill the relations:

$$\hat{\Pi}_i^2 = \hat{\Pi}_i \tag{2.5}$$

$$\hat{\Pi}_i \hat{\Pi}_j = \delta_{ij} \hat{\Pi}_i \tag{2.6}$$

and can be considered as elementary observables that query the system, "are you in state m_j?". Their eigenvalues (1/0) can directly be interpreted as the response ("yes"/"no") to such a query:

$$\hat{\Pi}_i|m_j\rangle = \delta_{ij}|m_i\rangle \tag{2.7}$$

The probability of obtaining a measurement value m_i for a quantum system prepared in a state $|\psi\rangle$ is calculated as the expected value of the corresponding projection operator

$$P(m_i) = \langle\psi|\hat{\Pi}_i|\psi\rangle = |\langle\psi|m_i\rangle|^2 \tag{2.8}$$

After a quantum measurement has been performed, the state vector must be updated according to the random measurement outcome m_l and the wave function "collapses" onto the eigenvector $|m_l\rangle$:

$$\frac{\hat{\Pi}_l|\psi\rangle}{P(m_l)} = |m_l\rangle \tag{2.9}$$

When a quantum system is described by a density matrix $\hat{\rho}$, the probability of obtaining a measurement outcome m_j is calculated via the trace operator:

$$P(m_i) = \mathrm{Tr}\big(\hat{\rho}\,\hat{\Pi}_i\big) = \sum_i \langle m_i|\hat{\rho}\hat{\Pi}_i|m_i\rangle \tag{2.10}$$

Similarly, the expected value of the observable $\hat{\mathcal{M}}$ is:

$$\langle\hat{\mathcal{M}}\rangle = \mathrm{Tr}\big(\hat{\rho}\,\hat{\mathcal{M}}\big) \tag{2.11}$$

2.2 Encoding Quantum Information in Photons

Two-dimensional quantum states, qubits, can be encoded in various degrees of freedom of photons (Tab. 1.3), the most common being time-bin and polarization encoding. Time-bin encoded qubits are used mainly in fiber-based quantum cryptography systems [139–144]. Polarization qubits, on the other hand, suffer from polarization-mode dispersion in long fibers, and coherent transmission via long fiber links is a more delicate matter [145]. However, polarization qubits have shown to be particularly well-suited for transmitting quantum information over turbulent atmospheric free-space links, and have been used for numerous fundamental tests of quantum theory at long distances (Tab. 1.1). In the following, we will only consider qubits encoded in polarization states of single photons, for example:

$$|0\rangle \equiv |H\rangle\,,\ |1\rangle \equiv |V\rangle \tag{2.12}$$

where $|H\rangle$ and $|V\rangle$ correspond to the vertical and horizontal linear polarization states.

Polarization states

A very useful way to visualize polarization states (Tab. 2.1), is the geometrical representation on the Poincaré sphere. In this representation, a pure state corresponds to a point on the surface of the sphere with polar coordinates 2θ and ϕ (Fig. 2.1):

$$|\psi\rangle = \cos(\theta)\,|H\rangle + e^{i\phi}\sin(\theta)\,|V\rangle \tag{2.13}$$

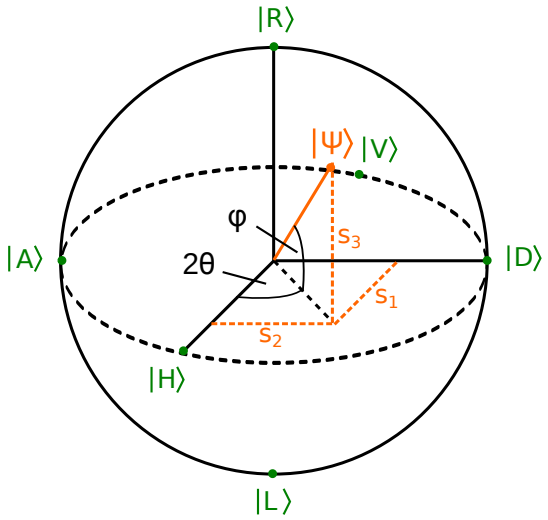

Figure 2.1: Representation of polarization states (Tab. 2.1) on the Poincaré sphere.

The coordinate axes in Fig. 2.1 have been chosen as the eigenvectors of the Pauli operators:

$$\hat{\sigma}_1 = |H\rangle\langle H| - |V\rangle\langle V| \tag{2.14}$$
$$\hat{\sigma}_2 = |D\rangle\langle D| - |A\rangle\langle A| \tag{2.15}$$
$$\hat{\sigma}_3 = |R\rangle\langle R| - |L\rangle\langle L| \tag{2.16}$$

Together with the identity operator $\hat{\sigma}_0 = \hat{\mathbb{1}}$, these operators form a complete basis for 2×2 Hermitian operators. Consequently, the density operator can be expressed as:

$$\hat{\rho}(\boldsymbol{s}) = \frac{1}{2}(\hat{\mathbb{1}} + \boldsymbol{s}\cdot\hat{\boldsymbol{\sigma}}) \tag{2.17}$$

where $\boldsymbol{s} = (s_1, s_2, s_3)$ is known as the Stokes vector and $\hat{\boldsymbol{\sigma}} = (\hat{\sigma}_1, \hat{\sigma}_2, \hat{\sigma}_3)$. The elements of the Stokes vector are simply the expected values for polarization measurements in the Pauli basis ($s_i = \mathrm{Tr}\big(\hat{\rho}(\boldsymbol{s})\hat{\sigma}_i\big)$). Stokes vectors representing pure states ($|\Psi(\boldsymbol{s})\rangle\langle\Psi(\boldsymbol{s})|$) lie on the surface of the Poincaré sphere ($|\boldsymbol{s}| = 1$). The Stokes vectors lying inside the Poincaré sphere $|\boldsymbol{s}| < 1$ correspond to mixed states,

with the center of the sphere $|\boldsymbol{s}| = 0$ corresponding to the completely depolarized mixed state:

$$\hat{\rho}_{unpol} = \frac{1}{2}(|H\rangle\langle H| + |V\rangle\langle V|) \equiv \frac{\hat{\mathbb{1}}}{2}. \tag{2.18}$$

polarization	state symbol	$\|H\rangle$,$\|V\rangle$ decomposition	(s_1, s_2, s_3)
linear horizontal	$\|H\rangle$	$\|H\rangle$	$(1, 0, 0)$
linear vertical	$\|V\rangle$	$\|V\rangle$	$(-1, 0, 0)$
linear diagonal	$\|D\rangle$	$\frac{1}{\sqrt{2}}(\|H\rangle + \|V\rangle)$	$(0, 1, 0)$
linear antidiagonal	$\|A\rangle$	$\frac{1}{\sqrt{2}}(\|H\rangle - \|V\rangle)$	$(0, -1, 0)$
right-handed circular	$\|R\rangle$	$\frac{1}{\sqrt{2}}(\|H\rangle + i\|V\rangle)$	$(0, 0, 1)$
left-handed circular	$\|L\rangle$	$\frac{1}{\sqrt{2}}(\|H\rangle - i\|V\rangle)$	$(0, 0, -1)$

Table 2.1: Common polarization states and their representations (Fig. 2.1).

Polarization measurement

A polarization measurement along a polarization direction $\boldsymbol{n}$ ($|\boldsymbol{n}| = 1$) on the Poincaré sphere is described by the operator:

$$\hat{\sigma}_{\boldsymbol{n}} \equiv \hat{\boldsymbol{\sigma}} \cdot \boldsymbol{n} \tag{2.19}$$

The state projectors corresponding to the measurement outcomes ($\sigma_{\boldsymbol{n}} = \pm 1$) read:

$$\hat{\Pi}(\sigma_{\boldsymbol{n}} = \pm 1) = \frac{1}{2}(\hat{\mathbb{1}} \pm \hat{\sigma}_{\boldsymbol{n}}) \tag{2.20}$$

For a polarization measurement performed on a photon described by a Stokes vector $\boldsymbol{s}$, the expected value of is given by:

$$\langle \hat{\sigma}_{\boldsymbol{n}} \rangle = \mathrm{Tr}\big(\hat{\rho}(\boldsymbol{s})\hat{\sigma}_{\boldsymbol{n}}\big) = (\boldsymbol{s} \cdot \boldsymbol{n}) \tag{2.21}$$

Complementary observables

Two observable quantities ($\hat{\sigma}_{\boldsymbol{n}}, \hat{\sigma}_{\boldsymbol{n}'}$) are considered complementary when complete knowledge of the result of a measurement of the first precludes any knowledge of the measurement outcome of the latter. Mathematically, the complementarity of observables is captured using the commutation operator:

$$[\hat{\sigma}_{\boldsymbol{n}}, \hat{\sigma}_{\boldsymbol{n}'}] = \hat{\sigma}_{\boldsymbol{n}}\hat{\sigma}_{\boldsymbol{n}'} - \hat{\sigma}_{\boldsymbol{n}}\hat{\sigma}_{\boldsymbol{n}'} \tag{2.22}$$

When two operators do not commute, i.e $[\hat{\sigma}_{\boldsymbol{n}}, \hat{\sigma}_{\boldsymbol{n}'}] \neq 0$, then it is impossible to simultaneously measure the corresponding observables with arbitrary precision

(Heisenberg uncertainty principle). In the two-dimensional Hilbert space, the Pauli operators form a set of three complementary, or mutually unbiased, measurement operators, i.e. $[\sigma_i, \sigma_j] = 2i\epsilon_{ijk}\sigma_k \neq 0$.

In order to illustrate this, let us consider a qubit prepared in the state $|H\rangle$. For this state, a measurement of $\hat{\sigma}_1$ results in a value 1 with unit probability ($\langle\hat{\sigma}_1\rangle = 1$). On the other hand, the measurement outcomes are completely undetermined for measurements of the complementary observables $\hat{\sigma}_2$ (or $\hat{\sigma}_3$), and values ± 1 are observed with equal probability. For the latter observables the measurement statistics are identical to those obtained for a completely mixed state ($\langle\hat{\sigma}_2\rangle = \langle\hat{\sigma}_3\rangle = 0$). This impossibility of simultaneously predicting the outcomes of conjugate measurements is the basis of the BB84 protocol for quantum key distribution [24, 146].

2.2.1 Polarization entanglement

In quantum theory composite quantum systems, comprising subsystems of two parties Alice (A) and Bob (B), are described by means of a state vector on the tensor product space $\mathcal{H}_A^2 \otimes \mathcal{H}_B^2$. A pure bi-partite quantum state that describes the composite system is called "entangled" if it cannot be written as a direct tensor product of individual state vectors of A and B ($|\psi\rangle_{AB} \neq |\psi\rangle_A \otimes |\phi\rangle_B$). An important class of pure entangled states are the maximally entangled Bell states:

$$\begin{aligned} |\Psi^{\pm}\rangle_{AB} &= \frac{1}{\sqrt{2}}(|H\rangle_A|V\rangle_B \pm |V\rangle_A|H\rangle_B) \\ |\Phi^{\pm}\rangle_{AB} &= \frac{1}{\sqrt{2}}(|H\rangle_A|H\rangle_B \pm |V\rangle_A|V\rangle_B) \end{aligned} \tag{2.23}$$

In a maximally entangled state, *all* information is shifted from the individual photons' polarizations to correlations between the polarizations of photons A and B. In order to see this let us assume Alice and Bob share a pair of photons in a $|\Phi^{\pm}\rangle_{AB}$ state and perform polarization measurements with linear polarizers oriented at angles α and β, respectively. Inserting the projection operators (Eq. 2.20) for linear polarizers:

$$\hat{\Pi}_{\alpha}^{A} = \frac{1}{2}\left(\hat{\mathbb{1}} + \cos(2\alpha)\hat{\sigma}_1 + \sin(2\alpha)\hat{\sigma}_2\right) \tag{2.24}$$

$$\hat{\Pi}_{\beta}^{B} = \frac{1}{2}\left(\hat{\mathbb{1}} + \cos(2\beta)\hat{\sigma}_1 + \sin(2\beta)\hat{\sigma}_2\right) \tag{2.25}$$

the probability for a coincidence detection of two photons reads:

$$\langle\Phi^{+}|\hat{\Pi}_{\alpha}^{A} \otimes \hat{\Pi}_{\beta}^{B}|\Phi^{+}\rangle = \frac{1}{2}\cos^2(\alpha - \beta) \tag{2.26}$$

which, remarkably, depends only on the relative orientation of the polarization analyzers. Hence, whenever a photon passes Alice's polarizer, oriented at an

angle α she can say with certainty that Bob's photon will also pass his polarizer, *should he have chosen to orient his polarizer at the same angle*. However, Alice cannot anticipate whether or not a given photon will actually pass her polarizer - which occurs with a probability of 50% - i.e., she can make definitive conditional predictions about the outcome of correlation measurements, but none about the polarization of her photon independently from Bob's.

More formally, when Alice attempts to describe the local state of her photon using a local density matrix $\hat{\rho}_A$, she does so by performing an average over Bob's possible measurement outcomes:

$$\hat{\rho}_A = \sum_{i=H,V} {}_B\langle i|\hat{\rho}_{AB}|i\rangle_B = \mathrm{Tr}_B\left(\hat{\rho}_{AB}\right) \tag{2.27}$$

with the partial trace operator Tr_B. Bob's reduced polarization state is calculated analogously ($\hat{\rho}_B = \mathrm{Tr}_A(\hat{\rho}_{AB})$). When applied to a maximally entangled state (Eq. 2.23), the partial trace yields a completely unpolarized mixed state (Eq. 2.18). We see that, while the local measurement outcomes are completely random they can, nevertheless, be nonlocally correlated.

This perplexing combination of nonlocal correlations and random local measurement outcomes inspired the famous Gedankenexperiment by Einstein, Podolsky, and Rosen, which subsequently became known as the EPR paradox [2, 147].

EPR paradox

The EPR example demonstrated that, assuming realism: "*if without in any way disturbing a system, we can predict with certainty - i.e. with probability equal to unity - the value of a physical quantity, then there exists an element of reality corresponding to this physical quantity*", and locality: "*no real change can take place in the second system in consequence of anything that may be done to the first*", quantum mechanics cannot be considered a complete theory, in which: "*every element of physical reality has a counterpart in the theory*".

In order to sketch their line of reasoning, let us consider a pair of photons, produced in a singlet state $|\Psi^-\rangle$, which are subsequently distributed to Alice who has a laboratory in Alicante, and Bob, in Barcelona. When Alice performs a polarization measurement $\hat{\sigma}_1^A$ on her photon, and obtains a result $\sigma_1^A = +1$, she can immediately conclude that the state of Bob's photon is $|V\rangle$ ($\sigma_1^B = -1$). Since the anti-correlation of the singlet state is invariant under rotations of the Poincaré sphere ($\hat{\sigma}_{\boldsymbol{n}}^A\hat{\sigma}_{\boldsymbol{n}}^B|\Psi^-\rangle = -|\Psi^-\rangle$), their results are also anti-correlated for polarization measurements in any other measurement basis. Thus, had Alice chosen to measure in the complementary basis $\hat{\sigma}_2^A$ and obtained a result $\sigma_2^A = 1$, she would have inferred that Bob's photon's state was $|A\rangle$ ($\sigma_2^B = -1$). Since the measurement performed on Alice's photon cannot influence the state of Bob's photon (locality assumption), the results of these complementary polarization measurement on Bob's photon must have been pre-determined, and thus, according to the above

definition, elements of physical reality. Hence, if quantum mechanics were a complete theory, it would have to contain a representation for the elements of reality corresponding to the complementary observables $\hat{\sigma}_1^B$ and $\hat{\sigma}_2^B$. Their measurement outcomes should thus be simultaneously predictable, which is not the case (uncertainty principle). EPR therefore concluded that *the quantum-mechanical description of physical reality can not be considered complete*, and implied the possibility of some other, complete, theory with unknown hidden variables that could be attributed to A and B individually (local realism).

Bell's inequality

In 1964 J. Bell showed that the assumption of underlying local realism leads to experimentally testable consequences [3]. A modified version of his original argument [6, 148] goes as follows: Consider an experiment in which Alice and Bob can each perform one of two possible polarization measurements along the directions $\boldsymbol{a}$, $\boldsymbol{a'}$ and $\boldsymbol{b}$, $\boldsymbol{b'}$, respectively. If the two-valued measurement outcomes ($\sigma_{\boldsymbol{a}}^A, \sigma_{\boldsymbol{a'}}^A, \sigma_{\boldsymbol{b}}^B, \sigma_{\boldsymbol{b'}}^B = \pm 1$) are pre-determined (local realism), then the following equation must hold[1]:

$$S = \left(\sigma_{\boldsymbol{a}}^A + \sigma_{\boldsymbol{a'}}^A\right)\sigma_{\boldsymbol{b}}^B + \left(\sigma_{\boldsymbol{a}}^A - \sigma_{\boldsymbol{a'}}^A\right)\sigma_{\boldsymbol{b'}}^B = \pm 2 \tag{2.28}$$

This also implies an upper bound for the expected value of $|\langle S\rangle|$:

$$|\langle S\rangle| = |\langle\sigma_{\boldsymbol{a}}^A\sigma_{\boldsymbol{b}}^B\rangle + \langle\sigma_{\boldsymbol{a}}^A\sigma_{\boldsymbol{b'}}^B\rangle + \langle\sigma_{\boldsymbol{a'}}^A\sigma_{\boldsymbol{b}}^B\rangle - \langle\sigma_{\boldsymbol{a'}}^A\sigma_{\boldsymbol{b'}}^B\rangle| \leq 2 \tag{2.29}$$

Eq. 2.29 is known as the CHSH (Clauser-Horne-Shimony-Holt) variant of Bell's inequality [6]. Now let us calculate the quantum-mechanical prediction $\langle\hat{S}\rangle$. Assuming Alice and Bob share photon pairs in a maximally-entangled $|\Psi^-\rangle$ state, then the expected value for a joint polarization measurement is:

$$\langle\Psi^-|\hat{\sigma}_{\boldsymbol{a}}^A\hat{\sigma}_{\boldsymbol{b}}^B|\Psi^-\rangle = -\boldsymbol{a}\cdot\boldsymbol{b} \tag{2.30}$$

Now, considering, for example, polarization measurements along the directions $\boldsymbol{a'} = (1,0,0)$,$\boldsymbol{a} = (0,1,0)$,$\boldsymbol{b} = 1/\sqrt{2}(1,1,0)$,$\boldsymbol{b'} = 1/\sqrt{2}(-1,1,0)$ on the Poincaré sphere (Fig. 2.1)[2] the quantum-mechanical expected values are:

$$\langle\hat{\sigma}_{\boldsymbol{a}}^A\hat{\sigma}_{\boldsymbol{b}}^B\rangle = \langle\hat{\sigma}_{\boldsymbol{a}}^A\hat{\sigma}_{\boldsymbol{b'}}^B\rangle = \langle\hat{\sigma}_{\boldsymbol{a'}}^A\hat{\sigma}_{\boldsymbol{b}}^B\rangle = -\frac{1}{\sqrt{2}} \tag{2.31}$$

$$\langle\hat{\sigma}_{\boldsymbol{a'}}^A\hat{\sigma}_{\boldsymbol{b'}}^B\rangle = \frac{1}{\sqrt{2}} \tag{2.32}$$

[1] Either ($\sigma_{\boldsymbol{a}}^A + \sigma_{\boldsymbol{a'}}^A = \pm 2$), in which case ($\sigma_{\boldsymbol{a}}^A - \sigma_{\boldsymbol{a'}}^A$), or ($\sigma_{\boldsymbol{a}}^A + \sigma_{\boldsymbol{a'}}^A = 0$), in which case ($\sigma_{\boldsymbol{a}}^A - \sigma_{\boldsymbol{a'}}^A = \pm 2$).

[2] Corresponding to linear polarization measurements under angle settings $\alpha = 45°$,$\alpha' = 0°$,$\beta = 22,5°$,$\beta' = -22,5°$

We thus see that quantum mechanics predicts a violation of the CHSH inequality:

$$\langle \hat{S} \rangle = \frac{4}{\sqrt{2}} = 2\sqrt{2} \nleq 2 \tag{2.33}$$

Eq. 2.29 can be tested experimentally by evaluating the correlation functions:

$$\langle \sigma_{\boldsymbol{a}}^{A} \sigma_{\boldsymbol{b}}^{B} \rangle_{exp} = \frac{N(+,+) + N(-,-) - N(+,-) - N(-,+)}{N(+,+) + N(-,-) + N(+,-) + N(-,+)} \tag{2.34}$$

where $N(\pm,\pm) = N(\sigma_{\boldsymbol{a}}^{A} = \pm 1, \sigma_{\boldsymbol{b}}^{B} = \pm 1)$ denotes the number of recorded coincidence detections.

The violation of Bell's inequality has been verified in numerous Bell test experiments with entangled particles, which irrefutably[3] demonstrate that a local realistic interpretation of quantum entanglement cannot hold. Interestingly, this opens up the door for exciting applications that extend beyond the capabilities of any method based on classical physics alone. An example of a quantum technology that directly makes use of the randomness associated with entanglement and complementarity is quantum key distribution [24].

Bell-state fidelity

In a laboratory setup, experimental imperfections inadvertently lead to some degree of impurity in the preparation of entangled qubits. A common way of quantifying the quality of the prepared state $\hat{\rho}$ is its overlap fidelity with an ideal target state. In the case of a pure target state, e.g. the maximally entangled Bell state $|\Psi^-\rangle$, the fidelity is defined as:

$$F_{\Psi^-}(\hat{\rho}) = \mathrm{Tr}\big(\hat{\rho}|\Psi^-\rangle\langle\Psi^-|\big) \tag{2.35}$$

When the generated state has perfect overlap with the ideal Bell state, the fidelity is 1, and for a completely mixed state the fidelity is 0.25. Typically, entanglement is ensured when F>0.5. For a detailed discussion of methods for quantifying entanglement, refer to [151]. The overlap fidelity is computed by reconstruction of the density matrix via quantum state tomography [152], and then directly evaluating Eq. 2.35.

Quantum state tomography is a procedure for reconstructing the density matrix of an unknown quantum state from a set of measurements performed on an ensemble of identically prepared particles. To see how this can be accomplished for

[3] There is a remaining issue of loopholes [11, 149, 150] in the experimental implementation of violations of Bell's inequality, which could conceivably lead to a local realistic explanation of the observed measurement results. However, all of these have been closed, albeit in different experiments. A violation of Bell's inequality that simultaneously closes all loopholes in a single experiment is highly likely to occur in the near future.

polarization-entangled photon pairs, consider the general definition of a two-qubit density matrix in terms of the complete set of Pauli matrices[4]:

$$\hat{\rho} = \frac{1}{4}\left(\sum S_{ml}\hat{\sigma}_m \otimes \hat{\sigma}_l\right) \tag{2.36}$$

The coefficients S_{ml} can be interpreted as two-photon Stokes parameters:

$$S_{ml} = \mathrm{Tr}\big(\hat{\rho}\,(\hat{\sigma}_m \otimes \hat{\sigma}_l)\,\big) \tag{2.37}$$

Inserting (Eqs. 2.14,2.15,2.16) into Eq. 2.37, the two-photon Stokes parameters, and thus the density matrix of the two photons, can be reconstructed by performing 6×6=36 elementary projective measurements ($|i\rangle\langle i|_A|j\rangle\langle j|_B$, where $i,j = H,V,D,A,L,R$). Note, however, that this procedure, known as linear state reconstruction, can lead to unphysical density matrices with negative eigenvalues. When this occurs the linearly reconstructed matrix can be used as the starting point for a numerical optimization procedure, called maximum likelihood estimation [153]. The maximum likelihood optimization determines the density matrix which was most probable, given the observed count rates, whereby the numerical optimization procedure is restricted to physically permissible density matrices.

When the Bell-state fidelity of an unknown experimental state $\hat{\rho}$ is the only parameter to be determined, it is more convenient to evaluate it directly [151]. Inserting Eq. 2.36 into Eq. 2.35 the Bell-state fidelity can be expressed as [154]:

$$F_{\Phi^\pm}(\hat{\rho}) = \frac{1 + \langle\hat{\sigma}_1\hat{\sigma}_1\rangle \pm \langle\hat{\sigma}_2\hat{\sigma}_2\rangle \mp \langle\hat{\sigma}_3\hat{\sigma}_3\rangle}{4} \tag{2.38}$$

$$F_{\Psi^\pm}(\hat{\rho}) = \frac{1 - \langle\hat{\sigma}_1\hat{\sigma}_1\rangle \pm \langle\hat{\sigma}_2\hat{\sigma}_2\rangle \pm \langle\hat{\sigma}_3\hat{\sigma}_3\rangle}{4} \tag{2.39}$$

The absolute values of the two-photon correlation functions are also referred to as the visibility in the respective Pauli basis ($V_{H/V} \equiv |\langle\hat{\sigma}_1\hat{\sigma}_1\rangle|$,$V_{D/A} \equiv |\langle\hat{\sigma}_2\hat{\sigma_2}\rangle|$, $V_{L/R} \equiv |\langle\hat{\sigma}_3\hat{\sigma}_3\rangle|$).

2.2.2 Entanglement-based quantum key distribution

Quantum key distribution (QKD) is one of the technically most advanced applications of quantum information theory, and a number of commercial products are already available. QKD solves the key distribution problem and enables two communicating parties, Alice and Bob, to establish a secret shared key (i.e. a random series of "1" and "0") via a quantum communication channel (e.g. fiber link, or free-space link). This key can be used for the encryption and decryption of subsequent communications, by performing a logical XOR operation on the binary coded message (plaintext). If the length of the key matches that of the plaintext, and the key is not re-used (one-time pad), the method enables unconditional security -

[4]Note, however, that the procedure presented is by no means the most efficient one. For a detailed review of quantum state tomography, the reader is referred to [152]

security regardless of the computational power of an eavesdropping adversary - of communications over a public communications channel (e.g. the internet)[5]. The security of QKD is rooted in the fundamental quantum principles of uncertainty (BB84 protocol [146]) and entanglement (BBM92 and E91 protocols [155, 156])[6].

In the BBM92 protocol, N photon pairs, each in a maximally polarization-entangled state (Eq. 2.23), are distributed to the communicating parties Alice and Bob via a quantum communications channel. Alice and Bob perform polarization measurements on the incoming photons, whereby they each randomly choose their measurement basis for the i-th measurement from one of two complementary measurement bases (e.g.$|H\rangle, |V\rangle$, and $|D\rangle, |A\rangle$). Alice and Bob assign binary values "0" to measurement outcomes (H, D) and "1" to outcomes (V, A), and thus obtain a random binary series, the raw key. In a subsequent step, called key sifting, Alice and Bob (publicly) announce the measurement basis chosen for the i-th polarization measurement, but keep the outcome of the respective measurement to themselves. Whenever they choose to measure their photons in the same basis, which occurs on average 50% of the time, Alice and Bob can infer their partner's bit-value, due to the perfectly correlated (or anti-correlated) nature of the entangled state i.e., in absence of errors, they share a set of identical random keys of length $N/2$ (sifted key).

The security of quantum key distribution is rooted in the basic principles of quantum physics. In order to gain information on the bit values obtained by A and B, a third party adversary (eavesdropping Eve) must perform quantum measurements on one (or both) of the entangled photons. Eve cannot make a faithful copy of the unknown quantum state and perform measurements after Alice and Bob announce their measurement settings, as a consequence of the no-cloning theorem [30]. Since the bit values are encoded in one of two randomly chosen, complementary bases, Eve can only guess in which measurement basis to perform her polarization measurement. Whenever Eve performs her measurement in a basis that differs from that subsequently chosen by A and B, she will thus introduce changes in Alice's and Bob's (ideally perfectly) correlated measurement outcomes.

Consequently, A and B can identify potential eavesdroppers by comparing parts of their sifted keys and evaluating the fraction of mis-matching bits (quantum bit error ratio - QBER). As long as the QBER stays below a certain threshold, the maximal amount of information gained by Eve can be estimated, and privacy amplification protocols can be used to distill a shorter, but unconditionally secure, key from the sifted key. In real-world QKD experiments, additional errors are caused by imperfections in the optical setup. In order to guarantee unconditional security, such errors must be regarded as potentially caused by an eavesdropping adversary. For a comprehensive security study of entanglement-based QKD in presence of experimental errors, see [159–161]. Concerning QKD in space, see [44] for a fea-

[5] QKD does not solve the problem of the authentication of the communicating parties, for which some initial shared key is required. It should, more appropriately, be understood as a method for key growing.

[6] See e.g. Refs. [24, 157, 158] for a review.

sibility study, and [46] for a performance analysis of quantum communication with a LEO satellite.

2.3 Spontaneous Parametric Down-Conversion (SPDC)

To date, the most well developed process for generating entangled photon pairs is spontaneous parametric down-conversion (SPDC). In SPDC, a strong coherent pump field interacts with the atoms of a second order nonlinear material, thus inducing a nonlinear polarization response which can give rise to the generation of two other fields, referred to as signal (s) and idler (i) fields. Unlike in classical parametric processes, the signal and idler fields are initially in their respective vacuum states. This spontaneous generation of signal and idler fields from the thinnest of air is not possible in classical nonlinear optics; SPDC is a purely quantum-mechanical phenomenon, and is therefore described within the framework of quantum optics. For a detailed introduction to nonlinear quantum photonics, see e.g. [162].

2.3.1 Two-photon SPDC state

In order to derive an expression for the two-photon SPDC state of the signal and idler photons, let us consider a strong pump laser which propagates along a principal axis of a nonlinear crystal of length L, which we choose as the z-axis of our coordinate system (Fig. 2.2).

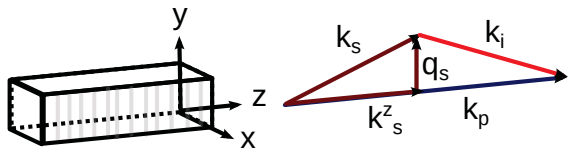

Figure 2.2: Coordinate system used in the calculation of the SPDC mode function.

Assuming that the wave-vector distribution of the pump, signal, and idler fields are peaked around this preferential propagation direction, it is prudent to separate the respective wave vectors into a longitudinal component ($k^z \boldsymbol{e}_z$) and a transverse component ($\boldsymbol{q} = q_x \boldsymbol{e}_x + q_y \boldsymbol{e}_y$):

$$\boldsymbol{k} = k_j^z(\omega, \mathbf{q})\boldsymbol{e}_z + \boldsymbol{q} \tag{2.40}$$

where ω denotes the angular frequency.

The phenomenological Hamilton operator [133, 135, 162, 163] that mediates the SPDC interaction between the pump, signal, and idler fields is given by:

$$\hat{H}_I = \epsilon_0 \int dV \boldsymbol{\chi}^{(2)}(z)\hat{\mathbf{E}}_p^+(\mathbf{r}_\perp, t, z)\hat{\mathbf{E}}_s^-(\mathbf{r}_\perp, t, z)\hat{\mathbf{E}}_i^-(\mathbf{r}_\perp, t, z) + H.c. \tag{2.41}$$

where $\boldsymbol{\chi}^{(2)}(z)$ is the second-order susceptibility tensor, V is the interaction volume, and $\hat{\mathbf{E}}_j^+(\mathbf{r}_\perp, t, z) = \hat{\mathbf{E}}_j^-(\mathbf{r}_\perp, t, z)^\dagger$ are the electromagnetic field operators ($j = s, i, p$) at time t and a position $\mathbf{r}_\perp = (x, y)$ in the transverse plane. The field operators can be expanded in terms of the orthonormal set of paraxial plane wave modes:

$$\begin{aligned}\hat{\mathbf{E}}_j^-(\mathbf{r}_\perp, t, z) &= \sum_{k=H,V} \frac{\boldsymbol{e}_{k,j}}{(2\pi)^{3/2}} \int d\omega_j d\mathbf{q}_j \, \hat{a}_{k,j}^\dagger(\omega_j, \mathbf{q}_j) f(\omega_j^0) \\ &\times \exp\left[ik_j^z(\omega_j, \mathbf{q}_j)z + i\mathbf{q}_j \cdot \mathbf{r}_\perp - i\omega_j t\right] \end{aligned} \tag{2.42}$$

where $f(\omega_j) = (\hbar\omega/2\epsilon_0 c n_j(\omega_j))^{1/2}$ is a normalization factor, and $n_j(\omega_j)$ denotes the refractive index. In this decomposition, the field creation operator ($\hat{a}_{k,j}^\dagger(\omega_j, \mathbf{q}_j)$) creates a photon in a plane-wave spatial mode with transverse wave vector $\boldsymbol{q}_j$, frequency ω_j, and polarization unit vector $\boldsymbol{e}_{k,j}$ ($j = s, i$), whereas the pump annihilation operator ($\hat{a}_{k,p}(\omega_p, \mathbf{q}_p)$ removes a photon from the pump field. The creation and annihilation operators fulfill the commutator relations:

$$\left[\hat{a}_{k,j}(\omega_1, \mathbf{q}_1), \hat{a}_{l,j}^\dagger(\omega_2, \mathbf{q}_2)\right] = \delta(\omega_1 - \omega_2)\delta^{(2)}(\mathbf{q}_1 - \mathbf{q}_2)\delta_{kl} \tag{2.43}$$

$$[\hat{a}_{k,j}(\omega_1, \mathbf{q}_1), \hat{a}_{l,j}(\omega_2, \mathbf{q}_2)] = 0 \tag{2.44}$$

$$\left[\hat{a}_{k,j}^\dagger(\omega_1, \mathbf{q}_1), \hat{a}_{l,j}^\dagger(\omega_2, \mathbf{q}_2)\right] = 0 \tag{2.45}$$

When the nonlinear material has only a single relevant non-zero tensor coefficient, the susceptibility tensor contracted with the unit vectors of the field operators reduces to a scalar effective nonlinear coefficient ($\boldsymbol{\chi}^{(2)}\boldsymbol{e}_p\boldsymbol{e}_s\boldsymbol{e}_i = \chi_{eff}^{(2)}$), and the electric field operators can be replaced by scalar operators $\hat{E}_j^- = \boldsymbol{e}_j \cdot \hat{\mathbf{E}}_j^-$. Depending on which nonlinear coefficient mediates the interaction, one distinguishes between type-0 (pump, signal, and idler co-polarized), type-I (signal and idler co-polarized, but orthogonal to pump), or type-II (signal and idler polarizations orthogonal) SPDC. In the following we assume a non-degenerate ($\omega_s \neq \omega_i$) type-0 interaction with vertically polarized pump, signal, and idler fields.

We have also left open the possibility of a spatial modulation of the nonlinear coefficient. In the case of an ideal periodic poling, the spatial dependence of the nonlinear coefficient is of the form:

$$\chi^{(2)}(z) = \chi^{(2)} e^{i\frac{2\pi}{\Lambda}z} \tag{2.46}$$

where Λ is the poling period along the crystal's z axis.

In order to calculate the state of the SPDC photons after the interaction, let us assume that the interaction of the pump signal and idler fields starts at a time t_1, at which the system is in an initial state $|\Psi_{initial}\rangle$. The state at time t_2, at which we

assume the interaction to be complete, is then given by the time-evolution operator:

$$|\Psi_{final}\rangle = \exp\left(-\frac{i}{\hbar}\int_{t_1}^{t_2}\hat{H}_I dt\right)|\Psi_{initial}\rangle \tag{2.47}$$

As the "S" in SPDC suggests, the signal and idler fields are in their respective vacuum states prior to the interaction. Assuming that the nonlinear interaction is sufficiently weak, the pump field remains undepleted and we can model the pump field as a vertically polarized, multi-mode coherent state with a distribution of transverse momenta $E_p(\boldsymbol{q})$, and a spectral distribution $S(\omega_p)$. The combined state of pump, signal, and idler prior to the interaction thus reads:

$$|\Psi_{initial}\rangle = |E_p(\boldsymbol{q}), S_p(\omega), V\rangle_p \otimes |vac\rangle_s|vac\rangle_i \tag{2.48}$$

Coherent states [164] are eigenstates of the photon creation- and annihilation operators, i.e.:

$$\hat{a}_{V,p}(\omega_p, \mathbf{q}_p)|E_p(\boldsymbol{q}), S_p(\omega), V_p\rangle = E_p(\boldsymbol{q})S_p(\omega)|E_p(\boldsymbol{q}), S_p(\omega), V_p\rangle \tag{2.49}$$

Consequently, when applying the Hamilton operator (Eq. 2.41) to the input state (Eq. 2.48), one can replace the pump field operator ($\hat{\mathbf{E}}_p^+$) with the pump beam's classical field amplitude ($\mathbf{E}_\mathbf{p}^+$). Then, approximating the time evolution (Eq. 2.47) to first order, we can write the SPDC state of the signal and idler at time t_2 as:

$$|\Psi_{final}\rangle_{s,i} = \left\{|vac\rangle_s|vac\rangle_i - \underbrace{\frac{i}{\hbar}\int_{t_1}^{t_2} dt\hat{H'}_I|vac\rangle_s|vac\rangle_i}_{|\Psi\rangle_{s,i}^{(2)}}\right\} + O(2). \tag{2.50}$$

where $\hat{H'}_I = \epsilon_0 \int dV \boldsymbol{\chi}^{(2)}(z)\mathbf{E}_\mathbf{p}^+\hat{\mathbf{E}}_\mathbf{s}^-\hat{\mathbf{E}}_\mathbf{i}^-$ denotes the modified Hamilton operator which acts only on the signal and idler subspaces. The two-photon contribution of Eq. 2.50 can be written as:

$$|\Psi\rangle_{s,i}^{(2)} \sim \int d\mathbf{q}_s d\mathbf{q}_i d\omega_s d\omega_i \Phi(\mathbf{q}_s, \mathbf{q}_i, \omega_s)|\omega_s, \mathbf{q}_s, V\rangle_s|\omega_i, \mathbf{q}_i, V\rangle_i \tag{2.51}$$

where $|\omega, \mathbf{q}, V\rangle \equiv \hat{a}_V^\dagger(\omega_j, \mathbf{q})|vac\rangle$ denotes the state of a single vertically polarized photon with with a frequency ω and a transverse wave vector $\boldsymbol{q}$. The bi-photon

mode function [162] in transverse momentum and frequency space, reads:

$$\begin{aligned}\Phi(\boldsymbol{q}_s, \boldsymbol{q}_i, \omega_s, \omega_i) \propto \int dz\, \boldsymbol{d\rho}\, dt\, d\omega_p\, d\boldsymbol{q}_p \\ \times E_p(\boldsymbol{q}_p) S_p(\omega_p) \exp\left[-i(\omega_p - \omega_s - \omega_i)t\right] \\ \times \exp\left[i\left(k_p^z(\boldsymbol{q}_p) - k_i^z(\boldsymbol{q}_i) - k_s^z(\boldsymbol{q}_s) - G^z\right) \cdot z\right] \\ \times \exp\left[i(\boldsymbol{q}_p - \boldsymbol{q}_s - \boldsymbol{q}_i) \cdot \boldsymbol{\rho}\right]\end{aligned} \tag{2.52}$$

At this point we should emphasize that SPDC only yields a two-photon entangled state when one neglects the higher-order terms as well as the dominant vacuum contribution in Eq. 2.50. The first-order approximation is justified by the assumption that the interaction is sufficiently weak, i.e. that the majority of pump photons do not result in the emission of photon pairs. Since the pair-production process is inherently random, there is no way of predicting when an entangle photon pair will be emitted by the nonlinear crystal. Consequently, the emission of the two-photon state can only be verified a posteriori, i.e. after a photon pair has been consumed by the photo-detectors. This post-selection procedure does not pose a significant problem for applications in QKD and fundamental tests of quantum theory. It is, however, a significant drawback for the implementation of quantum computation algorithms, which would ideally require that the generation of entanglement be announced beforehand [165–167]. The heralded generation of entangled photon pairs without the vacuum contribution can be achieved using higher-order SPDC emissions [168, 169], or by cascading two SPDC sources and using one photon of an entangled pair to pump a secondary down-conversion process [170, 171].

Another fundamental issue related to the stochastic nature of pair sources based on SPDC is multiple-pair emission due to the higher-order interaction terms in Eq. 2.50. Effects due to higher-order pair emissions will be discussed in more detail in Section 2.5.

2.3.2 SPDC mode function

The expression (2.52) for the bi-photon mode function can be significantly simplified by making a number of plausible assumptions: if the pump field is confined to a region much smaller than the nonlinear crystal's lateral dimensions, the spatial integration limits in the transverse plane can be extended to infinity, and the integration yields a delta function:

$$\int d\boldsymbol{\rho} e^{i(\boldsymbol{q}_p - \boldsymbol{q}_s - \boldsymbol{q}_i)\cdot\boldsymbol{\rho}} \to \delta(\boldsymbol{q}_p - \boldsymbol{q}_s - \boldsymbol{q}_i) \tag{2.53}$$

Furthermore, since we are interested in the SPDC once a steady-state condition has been reached, the integration limits can also be extended to infinity ($t_1 \to$

$-\infty$ and $t_2 \to \infty$). The resulting delta function can be interpreted as the energy-conservation condition:

$$\int dt e^{-i(\omega_p - \omega_s - \omega_i)t} \to \delta(\omega_p - \omega_s - \omega_i) \tag{2.54}$$

Inserting (Eq. 2.54) and (Eq. 2.53) into (Eq. 2.52), and carrying out the integration over the crystal length L, we arrive at a compact expression for the SPDC bi-photon mode function in transverse momentum and frequency space:

$$\Phi(\boldsymbol{q}_s, \boldsymbol{q}_i, \omega_s, \omega_i) = L\sigma \underbrace{E_p(\boldsymbol{q}_s + \boldsymbol{q}_i) S_p(\omega_s + \omega_i)}_{\text{pump field}} \underbrace{\text{sinc}(\frac{\Delta k^z}{2} L)}_{\text{phase matching}} \tag{2.55}$$

with an effective nonlinear coupling coefficient:

$$\sigma = \chi^{(2)} \sqrt{\frac{\hbar^3 \omega_s \omega_i \omega_p F_p}{64\pi^3 \epsilon_0 c^3 n_s(\omega_s) n_i(\omega_i) n_p(\omega_p)}} \tag{2.56}$$

The SPDC mode function (Eq. 2.55) is determined by two contributions: one from the pump field, which determines the total transverse momentum and energy available for the down-conversion process, and a phase-matching contribution

$$\text{sinc}\left(\frac{\Delta k^z}{2} L\right) \equiv \frac{\sin\left(\frac{\Delta k^z}{2} L\right)}{\frac{\Delta k^z}{2} L} \tag{2.57}$$

where Δk^z denotes the z-component of the wave-vector mismatch:

$$\Delta k^z = k_p^z(\boldsymbol{q}_s + \boldsymbol{q}_i, \omega_s + \omega_i) - k_s^z(\boldsymbol{q}_s, \omega_s) - k_i^z(\boldsymbol{q}_i, \omega_i) - \frac{2\pi}{\Lambda}. \tag{2.58}$$

for a periodically poled nonlinear crystal with a poling period Λ. The phase-matching function depends on the crystal length, as well as the dispersive properties of the nonlinear material, and determines how the available energy and momentum is distributed between the signal and idler photons. For propagation along a principal axis (non-critical phase matching), the longitudinal wave-vector components can be written as:

$$k_j^z(\omega_j, \mathbf{q}) = \sqrt{(\omega_j n_j(\omega_j)/c)^2 - |\mathbf{q}|^2} \tag{2.59}$$

Taylor expansion near $\Delta k = 0$

In many experimentally relevant scenarios, the wave vectors of the pump, signal, and idler photons are limited to a narrow range around the point of perfect collinear quasi-phase matching:

$$k_p^{z,0} - k_s^{z,0} - k_i^{z,0} - \frac{2\pi}{\Lambda} = 0 \tag{2.60}$$

where $k_j^{z,0} = n(\omega_j^0)\omega_j^0/c \equiv k_j^z(\omega_j^0, \boldsymbol{q}_j = 0)$. The frequencies that fulfill the collinear quasi-phase matching condition for a fixed pump frequency are known as the center phase-matched frequencies, where $\omega_s^0 + \omega_i^0 = \omega_p^0$ due to energy conservation. The collinear quasi-phase-matching point can be used as the starting point for a Taylor expansion of the longitudinal wave vectors k_j^z in terms of the frequency deviations from the central frequencies $\Omega_j = \omega_j - \omega_j^0$ ($\Omega_j \ll \omega_j^0$), and $\boldsymbol{q}_j$ ($|\boldsymbol{q}_j| \ll |\boldsymbol{k}_j|$):

$$k_j^z \sim k_j^{z,0} + \frac{\Omega_j}{u_j} + \frac{G_j\Omega_j^2}{2} - \frac{|\boldsymbol{q}_j|^2}{2k_j^{z,0}} \tag{2.61}$$

where $u_j = \partial k/\partial\omega^{-1}$ is the group velocity and $G_j = \partial/\partial\omega(1/u)$ is group velocity dispersion, evaluated at the respective central frequency. Note that the first-order spatial contribution $\frac{\partial k_j^z}{\partial \boldsymbol{q}_j}$ is zero for propagation along a principal axis (non-critical phase matching). This way we can significantly simplify the phase-matching function:

$$\begin{aligned}
\Delta k^z(\Omega_s, \Omega_i, \mathbf{q}_s, \mathbf{q}_i) &= \frac{|\mathbf{q}_s - \mathbf{q}_i|^2}{2k_p^{z,0}} && (2.62)\\
&+ \frac{\Omega_s + \Omega_i}{u_p} - \frac{\Omega_s}{u_s} - \frac{\Omega_i}{u_i} && (2.63)\\
&+ G_p\frac{(\Omega_s + \Omega_i)^2}{2} - G_s\frac{\Omega_s^2}{2} - G_i\frac{\Omega_i^2}{2}
\end{aligned}$$

where we have assumed that $k_p^{z,0} \sim 2k_{s,i}^{z,0}$.

Collinear SPDC with cw pump

A frequently encountered special case is collinear SPDC with a continuous-wave pump laser ($S_p(\Omega_s + \Omega_i) = \delta(\Omega_s + \Omega_i)$). For a cw pump the two-photon SPDC state (Eq. 2.55) reads:

$$|\Psi^{cw}\rangle \propto L\sigma \int d\Omega\, \mathrm{sinc}(\frac{\Delta k(\Omega)L}{2})\hat{a}_s^\dagger(\Omega)\hat{a}_i^\dagger(-\Omega)|vac\rangle \tag{2.64}$$

where $\Delta k(\Omega) \equiv \Delta k^z(\Omega, -\Omega, 0, 0)$ (Eq. 2.62). The probability of detecting a photon with a particular frequency deviation is given by the squared modulus of the mode function:

$$S(\Omega) \propto L^2\sigma^2\mathrm{sinc}^2(\frac{\Delta k(\Omega)L}{2}) \tag{2.65}$$

The spectral FWHM bandwidth ($\Delta\Omega_{FWHM}$) is readily obtained via the relation $\mathrm{sinc}^2(1.39) = 1/2$, i.e. solving:

$$\frac{\Delta k(\Delta\Omega_{FWHM})L}{2} = 1.39 \tag{2.66}$$

For type-II phase matching and non-degenerate type-0 and type-I phase matching, it is usually sufficient to consider the first-order approximation of (Eq. 2.62) and the frequency bandwidth thus reads:

$$\Delta\Omega_{FWHM} \sim \frac{2 \times 1.39}{LD} \tag{2.67}$$

where $D = 1/u_s - 1/u_i$ is the inverse group velocity mismatch of the signal and idler photons. For frequency-degenerate ($\omega_s = \omega_i = \omega_p/2$) type-0 and type-I phase matching the group velocities of signal and idler are equal. Consequently, the expansion of the phase mismatch must be extended to second order and the bandwidth is determined by the group velocity dispersion:

$$\Delta\Omega_{FWHM}^{degen} \sim \sqrt{\frac{2 \times 1.39}{LG}} \tag{2.68}$$

which results in a larger spectral bandwidth, and shorter coherence times.

2.3.3 Temporal correlations of SPDC biphotons

In addition to spectral correlations, the signal and idler photons can also exhibit strong correlations in their respective detection times. The correlation of the photon detection events in the signal and idler modes at times t_1 and t_2 at a fixed position $z = z_0$ is quantified using the second order intensity correlation function:

$$G^{(2)}(t_1, t_2) =< \hat{E}_s^-(t_1)\hat{E}_i^-(t_2)\hat{E}_s^+(t_1)\hat{E}_i^+(t_2) > \tag{2.69}$$

where the single-mode field operators for detection at time t are defined as

$$\hat{E}^-(t) = \frac{1}{(2\pi)^{3/2}} \int d\Omega\, \hat{a}^\dagger(\Omega) \exp\left(-i(\omega_0 + \Omega)t\right) \tag{2.70}$$

and $\hat{E}^+(t) = [\hat{E}^-]^\dagger$. Evaluating Eq. 2.69 for the two-photon state generated in cw-pumped collinear type-II SPDC (Eq. 2.64) yields the correlation of the detection times of the signal and idler photons:

$$G^{(2)}(t_1, t_2) \propto \left| \int d\Omega\, \mathrm{sinc}(\frac{D\Omega L}{2}) \exp\left(-i\Omega(t_1 - t_2)\right) \right|^2 \tag{2.71}$$

The range of Eq. 2.71 is inversely proportional to the two-photon spectral bandwidth ($\Delta\Omega_{FWHM}$). For a typical SPDC process the spectral bandwidth is of the order of 1nm, such that the signal and idler detection times are correlated to within approximately $1ps$. Note that the temporal structure of SPDC biphotons is usually not resolvable using direct detection with state-of-the-art single-photon detectors,

which typically exhibit timing jitters of the order of $> 0.5ns$, and interferometric techniques (Hong-Ou-Mandel interference [163, 172]) must be used. For a more detailed analysis refer to [133, 162].

In experiment, the temporal correlation can be used to identify the entangled photon pairs as detection events that occur simultaneously, i.e. within a certain timing window (coincidence window). When the average number of photon pairs emitted per timing window is small (< 0.1), and detector dark counts are significantly lower than the observed single-photon detection rates, these two-fold detection events can be attributed almost exclusively to the entangled photon pairs emitted by the source.

2.4 Polarization Entanglement in Bulk SPDC

Entanglement is a nonlocal coherence phenomenon, and the SPDC mode function (Eq. 2.55) naturally gives rise to entanglement in energy and momenta of signal and idler photons. However, achieving a pure polarization-entangled state generally requires additional effort; In general, polarization entanglement requires a bi-photon in a polarization product state, e.g. $|H\rangle_s|H\rangle_i$ to be *coherently* combined with a bi-photon with orthogonal polarizations $|V\rangle_s|V\rangle_i$. In other words, for the photons to be not merely correlated, but entangled in their polarization-degree of freedom requires that a constant phase relationship ($\exp(i\phi)$) between these two emission possibilities be maintained for all detected photon pairs. Only then can we write the two-photon state as:

$$|\Phi(\phi)\rangle = \frac{1}{\sqrt{2}}\left(|H\rangle_s|H\rangle_i + \exp(i\phi)|V\rangle_s|V\rangle_i\right) \tag{2.72}$$

When we are only interested in nonlocal polarization coherence, the phase relationship must be averaged over the degrees of freedom which are not resolved during the detection process. When the two emission processes are correlated with other degrees of freedom, this generally causes the coherence of the entangled state to be washed out, and results in a classically correlated mixed state.

In SPDC, correlations between polarization, momentum, and energy can lead to such dephasing effects which reduce the purity of the polarization-entangled state. Consider the total state resulting from superposition of two SPDC processes, each generating a pair of photons with a normalized mode function Φ_{HH} and Φ_{VV} ($\int |\Phi_{HH/VV}|^2 \mathbf{q}_s d\mathbf{q}_i d\Omega_s d\Omega_i$=1):

$$\begin{aligned}|\Phi_{\text{total}}\rangle = &\frac{1}{\sqrt{2}}\int d\mathbf{q}_s d\mathbf{q}_i d\Omega_s d\Omega_i \\ &\times \Phi_{VV}(\mathbf{q}_s, \mathbf{q}_i, \Omega_s, \Omega_i)|\mathbf{q}_s, \Omega_s\rangle|V_s\rangle|\mathbf{q}_i, \Omega_i\rangle|V_i\rangle \\ &+ \Phi_{HH}(\mathbf{q}_s, \mathbf{q}_i, \Omega_s, \Omega_i)|\mathbf{q}_s, \Omega_s\rangle|H_s\rangle|\mathbf{q}_i, \Omega_i\rangle|H_i\rangle\end{aligned} \tag{2.73}$$

In order to calculate amount of entanglement stored in the polarization subspace it will be more convenient to use the density matrix $\hat{\rho}_{\text{total}} = |\Phi_{\text{total}}\rangle\langle\Phi_{\text{total}}|$:

$$\begin{aligned}
&\hat{\rho}_{\text{total}} = \frac{1}{2}\int d\mathbf{q}_s d\mathbf{q}_i d\Omega_s d\Omega_i d\mathbf{q'}_s d\mathbf{q'}_i d\Omega'_s d\Omega'_i \times \\
&\Phi_{VV}(\Phi'_{VV})^*|\mathbf{q}_s,\Omega_s\rangle|V_s\rangle|\mathbf{q}_i,\Omega_i\rangle|V_i\rangle\langle\mathbf{q'}_s,\Omega'_s|\langle V'_s|\langle\mathbf{q'}_i,\Omega'_i|\langle V'_i| \\
&+\Phi_{VV}(\Phi'_{HH})^*|\mathbf{q}_s,\Omega_s\rangle|V_s\rangle|\mathbf{q}_i,\Omega_i\rangle|V_i\rangle\langle\mathbf{q'}_s,\Omega'_s|\langle H'_s|\langle\mathbf{q'}_i,\Omega'_i|\langle H'_i| \\
&+\Phi_{HH}(\Phi'_{VV})^*|\mathbf{q}_s,\Omega_s\rangle|H_s\rangle|\mathbf{q}_i,\Omega_i\rangle|H_i\rangle\langle\mathbf{q'}_s,\Omega'_s|\langle V'_s|\langle\mathbf{q'}_i,\Omega'_i|\langle V'_i| \\
&+\Phi_{HH}(\Phi'_{HH})^*|\mathbf{q}_s,\Omega_s\rangle|H_s\rangle|\mathbf{q}_i,\Omega_i\rangle|H_i\rangle\langle\mathbf{q'}_s,\Omega'_s|\langle H'_s|\langle\mathbf{q'}_i,\Omega'_i|\langle H'_i|
\end{aligned} \tag{2.74}$$

where $\Phi = \Phi(\mathbf{q}_s,\mathbf{q}_i,\Omega_s,\Omega_i)$ and $\Phi' = \Phi(\mathbf{q}'_s,\mathbf{q}'_i,\Omega'_s,\Omega'_i)$. The reduced polarization state of the signal and idler photons is obtained by performing the continuous partial trace (Eq. 2.27) over the frequency and momentum degrees of freedom:

$$\hat{\rho}_{\text{pol}} = \int d\mathbf{q}_s d\mathbf{q}_i d\Omega_s d\Omega_i \langle\mathbf{q}_s,\Omega_s|\langle\mathbf{q}_i,\Omega_i|\hat{\rho}_{\text{total}}|\mathbf{q}_s,\Omega_s\rangle|\mathbf{q}_i,\Omega_i\rangle \tag{2.75}$$

Using the orthogonality relations:

$$\langle\mathbf{q},\Omega|\mathbf{q}',\Omega'\rangle = \delta(\mathbf{q}-\mathbf{q}')\delta(\Omega-\Omega') \tag{2.76}$$

$$\langle i|j\rangle = \delta_{ij} \tag{2.77}$$

where $(ij = H,V)$, the reduced two-photon polarization state can be written as:

$$\begin{aligned}
&\hat{\rho}_{\text{pol}} = \frac{1}{2}\int d\mathbf{q}_s d\mathbf{q}_i d\Omega_s d\Omega_i \times \\
&\Phi_{VV}(\mathbf{q}_s,\mathbf{q}_i,\Omega_s,\Omega_i)\Phi^*_{VV}(\mathbf{q}_s,\mathbf{q}_i,\Omega_s,\Omega_i)\otimes|V_sV_i\rangle\langle V_sV_i| \\
&+\Phi_{VV}(\mathbf{q}_s,\mathbf{q}_i,\Omega_s,\Omega_i)\Phi^*_{HH}(\mathbf{q}_s,\mathbf{q}_i,\Omega_s,\Omega_i)\otimes|V_sV_i\rangle\langle H_sH_i| \\
&+\Phi_{HH}(\mathbf{q}_s,\mathbf{q}_i,\Omega_s,\Omega_i)\Phi^*_{VV}(\mathbf{q}_s,\mathbf{q}_i,\Omega_s,\Omega_i)\otimes|H_sH_i\rangle\langle V_sV_i| \\
&+\Phi_{HH}(\mathbf{q}_s,\mathbf{q}_i,\Omega_s,\Omega_i)\Phi^*_{HH}(\mathbf{q}_s,\mathbf{q}_i,\Omega_s,\Omega_i)\otimes|H_sH_i\rangle\langle H_sH_i|
\end{aligned} \tag{2.78}$$

The quality of polarization entanglement can be evaluated via the fidelity of $\hat{\rho}_{\text{pol}}$ with a maximally-polarization-entangled state (Eq. 2.23)[7]. With help of the orthogonality relations (Eq. 2.76), the fidelity with the $|\Phi^+\rangle\langle\Phi^+|$ state can be expressed as:

$$F = \frac{1}{2}\left[(1+O(\Phi_{VV},\Phi_{HH}))\right] \tag{2.79}$$

[7] Alternatively, one could calculate the purity $\text{Tr}(\hat{\rho}^2_{\text{pol}})$ of the reduced state.

where

$$O(\Phi_{VV}, \Phi_{HH}) = \Re\left(\int d\mathbf{q}_s d\mathbf{q}_i d\Omega_s d\Omega_i \Phi_{VV}(\mathbf{q}_s, \mathbf{q}_i, \Omega_s, \Omega_i)\Phi^*_{HH}(\mathbf{q}_s, \mathbf{q}_i, \Omega_s, \Omega_i)\right) \tag{2.80}$$

denotes the overlap integral of the two mode functions. The overlap integral is a measure of similarity, i.e. indistinguishability, of the two SPDC emission processes. In order to observe a maximally polarization-entangled state ($F = 1$), the two-photon pair emission processes must be indistinguishable ($O = 1$) in all degrees of freedom, other than their polarization[8]:

$$\Phi_{VV}(\mathbf{q}_s, \mathbf{q}_i, \Omega_s, \Omega_i) = \Phi_{HH}(\mathbf{q}_s, \mathbf{q}_i, \Omega_s, \Omega_i) \tag{2.81}$$

When the mode functions overlap perfectly the polarization of the vertically and horizontally polarized photon pairs are de-correlated from the spatio-temporal characteristics:

$$\begin{aligned} |\Psi_{\text{total}}\rangle \quad &= \tfrac{1}{\sqrt{2}} \int d\mathbf{q}_s d\mathbf{q}_i d\Omega_s d\Omega_i \Phi_{VV}(\mathbf{q}_s, \mathbf{q}_i, \Omega_s, \Omega_i)|\mathbf{q}_s, \Omega_s\rangle|\mathbf{q}_i, \Omega_i\rangle \\ &\otimes [|H_i\rangle|H_s\rangle + |V_i\rangle|V_s\rangle] \end{aligned} \tag{2.82}$$

When the mode functions are distinguishable ($O < 1$), entanglement between spatio-temporal wave function and polarization wave function leads to "which-polarization" information that diminishes the purity of the polarization state ($F < 1$). In particular, when the mode functions are perfectly distinguishable ($O = 0$) the nonlocal coherence is entirely washed out, and one observes a classically-correlated mixed state:

$$\hat{\rho}_{\text{pol}} = \frac{1}{2}\left[|H_s H_i\rangle\langle H_s H_i| + |V_s V_i\rangle\langle V_s V_i|\right] \tag{2.83}$$

Such a classically correlated state exhibits perfect polarization correlations in the H/V measurement basis, but no correlations in the conjugate measurement bases L/R and D/A. In the following we will see how the spatio-temporal wave function can be "disentangled" from the polarization wave function in two prototypical polarization-entangled photon sources based on SPDC in bulk nonlinear crystals.

2.4.1 Crossed-crystal configuration

A particularly intuitive approach for generating polarization entanglement is the so-called crossed-crystal (or "sandwich") configuration, first demonstrated by Kwiat

[8] This can also, entirely equivalently, be thought of in terms of distinguishability of the respectively polarized photon pairs in time and space [173].

et al. in 1999 [88]. In the original implementation, entanglement was achieved by overlapping non-collinear type-I SPDC emission cones from two orthogonally oriented nonlinear crystals, placed in sequence. A significant increase in efficiency can be obtained in a collinear variant of the crossed-crystal configuration with non-degenerate signal and idler wavelengths [89]. The non-degenerate signal and idler wavelengths allow the photons to be routed into distinct spatial modes using, for example, a dichroic mirror or an in-fiber wavelength division multiplexer (WDM).

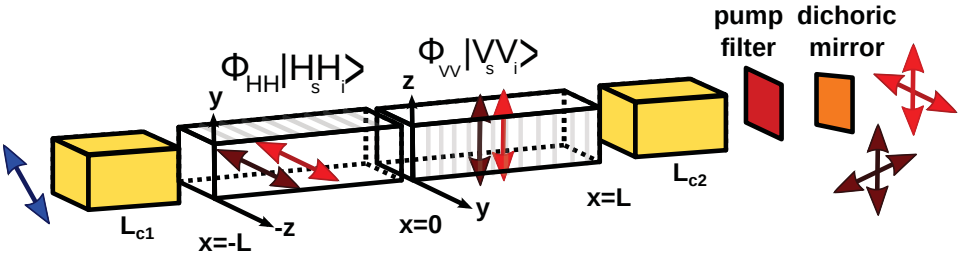

Figure 2.3: Generation of polarization entanglement in a crossed-crystal configuration. A pump photon is polarized diagonally, such that it can give rise to a photon pair in one of two periodically poled nonlinear crystals placed in sequence. The nonlinear crystals are rotated by 90 °, such that the two pair emission possibilities have orthogonal polarizations. Since the two SPDC emission processes are distinguishable by means of their spectral phase (or equivalently, their time of arrival at the detectors), birefringent compensation crystals (yellow) are necessary, in order to ensure a coherent superposition of the two emission processes.

In the collinear crossed-crystal scheme, two mutually orthogonally oriented nonlinear crystals of length L are placed directly one after the other. We choose the coordinate system such that the center interface separating the two crystals is located at a position $x = 0$ (Fig. 2.3). The crystals are quasi-phase matched for a type-0 SPDC process, with co-polarized signal and idler photons at non-degenerate center wavelengths, and pumped with a beam propagating along the x-direction.

At the input facet of the first crystal the pump has a spectral amplitude $S_p(\Omega_p)$ and a polarization state:

$$|\alpha_p\rangle = \frac{1}{\sqrt{2}}(|H\rangle + \exp(i\phi_0)|V\rangle) \tag{2.84}$$

The pump thus drives SPDC emissions from the first crystal ($\Phi_{HH}(\Omega_s, \Omega_i)|HH\rangle$) and second crystal ($\Phi_{VV}(\Omega_s, \Omega_i)|VV\rangle$) with equal magnitude. For the sake of brevity, let us restrict the signal and idler fields to a single spatial mode, such as a collinear plane-wave ($\mathbf{q_j} = \mathbf{0}$, for $j = p, s, i$). Spatial effects do not, therefore, influence the two-photon entanglement visibility. As a consequence of the crossed-crystal geometry, the pairs generated in the first crystal acquire an additional dispersive phase delay compared to the pairs emitted from the second. To understand this "which-crystal" information arises in more detail, we consider the mode function of the horizontally polarized photons at the output of the first crystal ($x = 0$):

$$\Phi_{HH}|_{x=0} \propto \overbrace{S_p(\Omega_p) \underbrace{\exp\left(i\left[\frac{\Omega_p}{u_p^z}\right]\frac{L}{2}\right)}_{\text{pump propagation to } x=-L/2} \text{sinc}(\frac{\Delta k^z L}{2})}^{\text{mode function at } x=-L/2} \times \underbrace{\exp\left(i\left[\frac{\Omega_s}{u_s^z}+\frac{\Omega_i}{u_i^z}\right]\frac{L}{2}\right)}_{\text{SPDC propagation to } x=0} \quad (2.85)$$

The exponential factor accounts for the propagation of the bi-photon, from the center of the crystal (see Eq. 2.55) to the exit facet of the crystal. The horizontally polarized photon pair then propagates through the second crystal (with a group velocity u^y), and the bi-photon state after traversing both crystals ($x = L$) reads:

$$\Phi_{HH}|_{x=L} \propto \Phi_{HH}|_{x=0} \times \underbrace{\exp\left(i\left[\frac{\Omega_s}{u_s^y}+\frac{\Omega_i}{u_i^y}\right]L)\right)}_{\text{SPDC prop. to } x=L} \quad (2.86)$$

Similarly, the mode function of the vertically polarized pair at $x = L$ reads:

$$\Phi_{VV}|_{x=L} \propto \overbrace{\underbrace{S_p(\Omega_p)\exp\left(i\left[\frac{\Omega_p}{u_p^y}\right]L\right)}^{\text{pump propagated to } x=0} \overbrace{\exp\left(i\left[\frac{\Omega_p}{u_p^z}\right]\frac{L}{2}\right)}^{\text{pump propagation to } x=L/2} \text{sinc}(\frac{\Delta k^z L}{2})}^{\text{mode function at } x=L/2} \times \underbrace{\exp\left(i\left[\frac{\Omega_s}{u_s^z}+\frac{\Omega_i}{u_i^z}\right]\frac{L}{2}\right)}_{\text{SPDC propagation to } x=L} \quad (2.87)$$

Comparing the mode functions after passing through both crystals ($x = L$), we see that the bi-photons generated in the first crystal acquire an additional spectral phase relative to the pairs emitted from the second:

$$\text{Arg}\{\Phi_{HH}|_{x=L}\} - \text{Arg}\{\Phi_{VV}|_{x=L}\} = \left[\left(\frac{\Omega_s}{u_s^y}+\frac{\Omega_i}{u_i^y}\right)-\frac{\Omega_s+\Omega_i}{u_p^y}\right]L \quad (2.88)$$

where we have used the fact that $\Omega_p = \Omega_s + \Omega_i$. When integrated over the detected bandwidth, this phase-dependence diminishes the purity of the polarization-entangled state. Of course it would be possible to restrict the spectral bandwidth by placing narrowband spectral filters, and therefore avoid the de-phasing issue as we have done for the spatial case (by projecting into a single spectral mode). This, however, would lead to a dramatic, and ultimately unnecessary, decrease in the number of detected photon pairs. A much more elegant solution is to place dispersive, birefringent compensation crystals in the path of the pump and SPDC photons.

Compensation crystals

The compensation of the additional phase (Eq. 2.88) can be broken down into two steps. First we determine the length of the post-compensation crystal that compensates for the additional phase due to the group-velocity mismatch between the signal and idler photons. Then we choose a precompensation crystal, which compensates for the additional phase due to the propagation of the pump photons through the first crystal[9]. For the first step we assume that the pump driving the SPDC process is cw. The remaining phase-difference to be compensated for is then:

$$\mathrm{Arg}\left\{\Phi_{HH}|_{x=L}\right\} - \mathrm{Arg}\left\{\Phi_{VV}|_{x=L}\right\} = \left(\frac{1}{u_s^y} - \frac{1}{u_i^y}\right)\Omega L \tag{2.89}$$

where $\Omega \equiv \Omega_s = -\Omega_i$. In order to compensate, we place a crystal of length L_{c2} with the inverse birefringent dispersion in the path of the signal and idler photons. The compensation crystal is oriented with its extraordinary axis parallel to the horizontal polarization, and the ordinary axis in line with the vertical polarizations. When propagating in this crystal, the horizontally polarized signal and idler photons thus travel with group velocities of the ordinary beam u_s^o and u_s^o, and the vertically polarized signal and idler with group velocities of the extra-ordinary u_s^e and u_s^e, respectively. Hence the phase shift accumulated after the compensator reads:

$$\begin{aligned}\mathrm{Arg}\left\{\Phi_{HH}|_{x=L+L_{c2}}\right\} - \mathrm{Arg}\left\{\Phi_{VV}|_{x=L+L_{c2}}\right\} &= \left(\frac{1}{u_s^y} - \frac{1}{u_i^y}\right)\Omega L \\ &+ \left(\frac{1}{u_s^o} - \frac{1}{u_i^o}\right)\Omega L_{c2} - \left(\frac{1}{u_s^e} - \frac{1}{u_i^e}\right)\Omega L_{c2}\end{aligned} \tag{2.90}$$

Perfect phase compensation is achieved for when the length of the compensation crystal is chosen to be:

$$L_{c2} = \frac{\left(\frac{1}{u_s^y} - \frac{1}{u_i^y}\right)L}{\left(\frac{1}{u_s^e} - \frac{1}{u_i^e}\right) - \left(\frac{1}{u_s^o} - \frac{1}{u_i^o}\right)} \tag{2.91}$$

The length of the precompensation crystal L_{c1} can then be obtained similarly, by adding the additional phase delay due to the post-compensation crystal to Eq. 2.88:

$$L_{c1} = \frac{\left(\frac{1}{u_i^y} - \frac{1}{u_p^y}\right)L + \left(\frac{1}{u_i^o} - \frac{1}{u_i^e}\right)L_{c2}}{\left(\frac{1}{u_p^e} - \frac{1}{u_p^o}\right)} \tag{2.92}$$

[9]Note again, that this analysis in terms of distinguishing spectral phase information is entirely equivalent to considering distinguishing timing information in the temporal domain, where it becomes a problem of matching the average arrival times of the down-converted photons.

Notice that this compensation technique requires a compensation crystal that not only exhibits birefringence, but different dispersion of the crystallographic axes, i.e. $\left(\frac{1}{u_s^e} - \frac{1}{u_i^e}\right) \neq \left(\frac{1}{u_s^o} - \frac{1}{u_i^o}\right)$, such as yttrium orthovanadat (YVO_4). This requirement can be relaxed - allowing the use of calcite, for example - by placing the two compensation crystals, not before and after the down-converting crystals, but in the respective signal and idler paths (after separating the frequency degenerate photons via a dichroic mirror). Note that this requires different lengths of compensating crystal, which can be calculated similarly to the above discussion.

2.4.2 Sagnac configuration

The dephasing in the crossed-crystal configuration is a result of the different dispersion experienced by the two orthogonally polarized pair emission possibilities. This can be avoided in, for example, an interferometric setting, where the two orthogonally oriented nonlinear crystals are each placed in one arm of a Mach-Zehnder interferometer, and then combined on a polarizing beam splitter. While no compensation crystals would be required, this would require sub-wavelength balancing of the two paths of the interferometer in order to maintain a fixed phase-relation between the two emission possibilities over longer timescales. A more elegant solution was demonstrated by Kim et al. [174]; by bi-directionally pumping a single nonlinear crystal, placed at the center of a Sagnac loop, the phase-delays are auto-compensated, without the need for active interferometric stabilization.

In the Sagnac scheme, a type-II nonlinear crystal is placed at the center of a polarization Sagnac interferometer, consisting of a polarizing beam splitter and a half-wave plate (which both work for pump, signal, and idler wavelengths), as depicted in Fig. 2.4. A diagonally polarized pump beam is incident on the polarizing beam splitter, which directs the horizontal pump component into the clockwise propagation direction inside a Sagnac loop. The pump beam then produces a pair of orthogonally polarized photons in a state $\Phi_{HV}(\Omega_s, \Omega_i)|H_s\rangle|V_i\rangle$. The SPDC photons pass the half-wave plate oriented at 45°, which flips the polarization of the down-converted photons while leaving the spectral phase distribution unchanged ($\Phi_{HV}(\Omega_s, \Omega_i)|V_s\rangle|H_i\rangle$). The polarizing beam splitter then transmits the horizontally polarized photon and reflects the $|V_s\rangle$ photon into the spatial mode 1 and photon $|H_i\rangle$ into mode 2. The vertically polarized pump component is reflected into the counter-clockwise propagation direction of the Sagnac loop, and is flipped such that it enters the nonlinear crystal with its polarization parallel the phase-matched axis, where it can produce a pair of photons in the counter-clockwise propagation direction ($\Phi_{HV}(\Omega_s, \Omega_i)|H_s\rangle|V_i\rangle$). The superimposed state of these two pair-generation possibilities, after the PBS, then naturally factors into spectral-phase and polarization subspaces:

$$\begin{aligned}\left|\Psi^{(2)}_{\text{Sagnac}}\right\rangle &= \tfrac{1}{\sqrt{2}} \int d\mathbf{q}_s d\mathbf{q}_i d\Omega_s d\Omega_i \Phi_{HV}(\mathbf{q}_s, \mathbf{q}_i, \Omega_s, \Omega_i)|\mathbf{q}_s, \Omega_s\rangle|\mathbf{q}_i, \Omega_i\rangle \\ &\otimes [|H_i\rangle|V_s\rangle + \exp(i\phi)|V_i\rangle|H_s\rangle]\end{aligned} \tag{2.93}$$

The Sagnac scheme thus produces a maximally polarization-entangled state, without the need for additional compensation crystals[10]. The relative phase ϕ of the entangled state can be set by adjusting the relative phase of the pump polarization. The Sagnac scheme can also be implemented with type-0 or type-I nonlinear crystals. In this case, however, both counter-clockwise and clockwise SPDC emissions are emitted into the same output port of the PBS, and must be separated via an additional dichroic element (see Chapter 7).

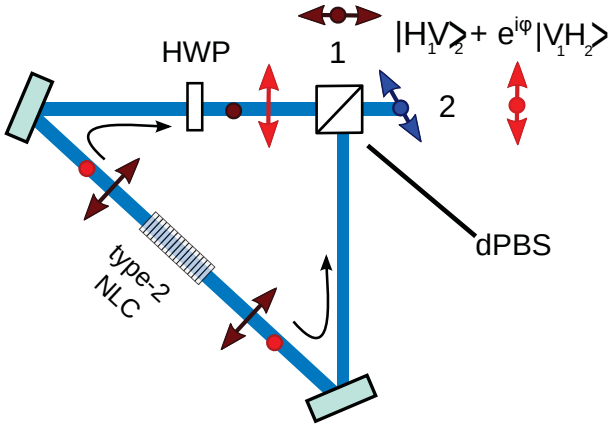

Figure 2.4: Generation of polarization entanglement in a Sagnac loop configuration. A diagonally polarized pump photon is incident on a polarizing beam splitter, such that it can give rise to a photon pair either the clockwise or counter-clockwise arm. The half-wave plate (HWP) oriented at 45° flips the polarization of the signal and idler photons, such that they overlap in the output ports of the beam splitter. Since the two SPDC emission processes are indistinguishable, no additional compensation crystals are necessary.

2.5 Higher-Order Pair Emission Effects in SPDC

In the discussion thus far we have considered only the two-photon contribution of the SPDC process. This was motivated by the assumption that the pump field was sufficiently weak. Now let us also consider the higher-order terms in the expansion of the time evolution operator (Eq. 2.47), which lead to the simultaneous emission of multiple photon pairs. Multiple-pair emission can be used to produce multi-photon entangled states which are an essential resource for the implementation of numerous applications in quantum information processing [162, 163, 177]. However, in experiments that require two-photon entanglement the higher-order pair emissions reduce the visibility of experimentally observed correlations, as

[10] It is also worth noting that, for non-separable mode functions (Eq. 2.55), the state in Eq. 2.93 naturally exhibits hyper-entanglement [86, 175], that is, entanglement in several degrees of freedom, without the need for additional compensation. Hyper-entangled states can be used to encode higher-dimensional quantum information, and promise significant advantages in the implementation of quantum communication protocols [176].

will be outlined in the following. For a detailed discussion of multi-photon entanglement and multiple-pair effects in two-photon experiments, see e.g. Refs. [154, 162, 163, 177–180] and [179, 181–184], respectively.

2.5.1 Multi-pair emission in SPDC

First, let us consider an SPDC source which emits signal and idler photons into a single spatial and spectral mode. The single-mode interaction Hamiltonian for a type-II polarization-entangled photon source reads:

$$\hat{H}_I = g(\hat{a}^\dagger_{V,s}\hat{a}^\dagger_{H,i} - \hat{a}^\dagger_{H,s}\hat{a}^\dagger_{V,i}) + H.c. \tag{2.94}$$

where $H.c.$ denotes the Hermitian conjugate, and g is the nonlinear coupling constant ($g \propto \sqrt{P_0} \times \chi^{(2)}$, where P_0 denotes the pump power). The time evolution of the signal and idler modes due to the interaction is given by $|\Psi\rangle = \exp(-i\hat{H}_I t)|vac\rangle$, and the resulting multi-photon state can be written as [160, 166, 182]:

$$|\Psi_{SPDC}\rangle = \cosh(\tau)^{-2} \sum_{n=0}^{\infty} \sqrt{n+1}\tanh^n\tau|\Phi_n\rangle \tag{2.95}$$

with $\tau = gt$, and the n-photon-pair states:

$$|\Phi_n\rangle = \frac{1}{\sqrt{n+1}} \sum_{m=0}^{n} (-1)^m |(n-m)_H, m_V\rangle_s |m_H, (n-m)_V\rangle_i \tag{2.96}$$

The probability of generating n pairs ($P_n = |\langle\Phi_n|\Psi_{SPDC}\rangle|^2$), expressed in terms of the average number of photon pairs ($\mu = \sum_{n=0}^{\infty} = P_n \times n = 2\sinh^2(\tau)$), reads:

$$P_n = \frac{\frac{\mu}{2}}{1 + (\frac{\mu}{2})^{n+2}}(n+1) \tag{2.97}$$

For low average pair rates the probability of producing an n-photon pair state scales as $\mu^n \propto (P_{PUMP} \times (\chi^{(2)})^2)^n$. Consequently, the probability of generating multiple photon pairs is rather low for typical nonlinearities and cw pump powers. Therefore, experiments involving multi-photon entanglement generally employ pulsed pump lasers with high peak powers.

In limiting our discussion so far to a single mode for the signal and idler, we have assumed that the entangled photon source generates n *indistinguishable* photon pairs from the conversion of n pump photons. In other words, the multi-photon entangled state (Eq. 2.96) is generated from a single, coherent SPDC process.

When discussing multi-photon entangled states one generally distinguishes between continuous-wave and pulsed operation. For pulsed sources (e.g. [185–188]),

multiple-pair emissions can be considered indistinguishable in time if their coherence time (t_{coh}) is longer than the pulse length of the pump field driving the SPDC process. For cw-pumped SPDC sources, the photon pairs can only be considered quantum-mechanically indistinguishable if their coherence time is longer than the coincidence window (t_c, see 2.3.3) used to identify photon-pair detections ($t_{coh} > t_c$) [68, 69]. This can, for example, be achieved by employing extremely narrowband spectral filters [70], which results in a significant decrease in the observed pair rates. An alternative approach is cavity-enhanced SPDC, where the nonlinear crystal is placed inside a resonant cavity, which leads to a reduction of the bandwidth of the SPDC photons [71–73]. For a detailed discussion of multi-photon entangled states, see Refs. [154, 162, 163, 178–180]

For the cw-puped sources presented in this thesis, however, the coherence time of signal and idler photons is small compared to the coincidence window. Consequently, multiple photon pairs emitted within the electronic coincidence window can be distributed over $t_c/t_{coh} >> 1$ temporal modes. The emission thus consists of n-distinguishable photon pairs, which exhibit a Poissionian photon-number distribution [182]:

$$P_n \simeq e^{-\tilde{\mu}} \frac{\tilde{\mu}^n}{n!} \tag{2.98}$$

where $\tilde{\mu}$ denotes the average number of pairs *per coincidence window*.

2.5.2 Coincidence detection with threshold detectors

In experiment, the emission of a specific photon-number state is verified in post-selection, i.e by detecting exactly n photon pairs in the setup. This is commonly accomplished via a coincidence measurement with $2n$ detectors, where each detector registers a single photon each. Threshold detectors, such as Si SPADs do not discriminate between different numbers of photon numbers. When n photons impinge on a threshold detector it produces a macroscopic electronic response, with a probability:

$$P_n^{detection} = 1 - (1 - \eta)^n \tag{2.99}$$

where η is the detection efficiency. In absence of additional uncorrelated background noise, such a coincidence measurement verifies that *at least* $2n$ photons were present in the optical setup. The higher-order emissions, however, can also result in the registration of an $2n$ photon coincidence. As the average pair-emission rate increases these so-called accidental coincidences lead to an unavoidable reduction of the n-pair entanglement visibility. This degradation is inherent to all entangled photon sources based on SPDC, and cannot be completely mitigated unless single-photon number resolving detectors [128, 129, 189] with perfect collection efficiencies are employed [125, 126].

For the cw-pumped sources presented in this thesis, the emission of multiple distinguishable pairs per coincidence window leads to a reduction in the quality of

two-photon entanglement before coherent multi-pair effects become relevant. In the following we discuss the impact of accidental coincidences on the experimental two-photon entanglement visibility in high-loss free-space links.

2.5.3 Multi-pair effects in presence of loss and background counts

Let us assume that our SPDC source generates distinguishable photon pairs, each in $|\Phi^+\rangle$ state, at an an average rate of R_0 pairs per second. The photons are distributed to Alice (A) and Bob (B) via two links with transmissions η_A and η_B, respectively. The polarization correlations are assessed using polarizers located in front of the respective single-photon detectors. The module efficiency of the receivers and polarization optics is η_C. The photon pairs are detected with two threshold detectors, each with a dark count rate D, a detection efficiency η_D, and a timing jitter t_d. The photon pairs are identified using an electronic coincidence window $t_c > t_d$.

When the polarizers are parallel the detectors register a coincidence rate of:

$$R^{(2)}_{parallel} \simeq \frac{1}{2}\eta_h \eta_C^2 \eta_D^2 \eta_A \eta_B R_0 + R^{(acc)} \tag{2.100}$$

where $\eta_h < 1$ denotes the heralding efficiency of the source (coincidence-to-singles ratio, See Chapter 4) and $R^{(acc)}$ is the rate of accidental coincidences. The additional factor $\frac{1}{2}$ is due to the polarizer blocking half of the photon pairs emitted by the source. The number of accidental coincidences is approximately:

$$R^{(acc)} \simeq R^{(1)}_A \times R^{(1)}_B \times t_c \tag{2.101}$$

where $R^{(1)}_A$ and $R^{(1)}_B$ are the number of single-photon detections registered at Alice and Bob's detectors, respectively:

$$R^{(1)}_A \simeq \frac{1}{2}\eta_C \eta_D \eta_A R_0 + D \tag{2.102}$$

$$R^{(1)}_B \simeq \frac{1}{2}\eta_C \eta_D \eta_B R_0 + D \tag{2.103}$$

If we assume that the source emits an ideal $|\Phi^+\rangle$ state, and that neither the transmission channel nor the detection module adversely affect the polarization correlations (Eq. 2.26), the coincidence count rate for crossed polarizers can be attribute solely to accidental coincidences:

$$R^{(2)}_{crossed} \simeq R^{(acc)} \tag{2.104}$$

The visibility of the experimentally observed two-photon interference fringes is thus:

$$V = \frac{R^{(2)}_{prallel} - R^{(2)}_{crossed}}{R^{(2)}_{parallel} + R^{(2)}_{crossed}} = \frac{\frac{1}{2}\eta_h \eta_C^2 \eta_D^2 \eta_A \eta_B R_0}{\frac{1}{2}\eta_h \eta_C^2 \eta_D^2 \eta_A \eta_B R_0 + 2R^{(acc)}} \tag{2.105}$$

In absence of background counts this can be simplified to:

$$V \simeq \frac{1}{1+\mu_0/\eta_h} \tag{2.106}$$

where $\mu_0 = R_0 \times t_c$ is the average number of photon pairs emitted in the source. The length of the coincidence window thus imposes the practical upper bound on the emitted pair rates (R_0) for which the entangled correlations can still be observed with high visibility. This clearly demonstrates that high pair-detection rates require low-timing-jitter single-photon detectors. As an alternative to using shorter coincidence windows, multiplexing the signal and idler photons using auxiliary correlations in other degrees of freedom can also reduce accidental coincidences [183, 190–193]. Equation 2.106 also shows that it is important that the source have a high heralding efficiency (coincidence-to-singles ratio, see Chapter 4).

Chapter 3

Spectral Characterization of SPDC in Periodically Poled $KTiOPO_4$

The generation of polarization-entangled photons with high brightness and visibility requires a reliable, robust, and efficient pair-production process. The current workhorse for the production of polarization-entangled photon pairs is spontaneous parametric down-conversion (SPDC) in second-order nonlinear crystals (see Chapter 2). Over the last decade, a number of bright sources generating photon pairs via type-0, type-I, and type-II quasi-phase matching in periodically poled potassium titanyl phosphate ($KTiOPO_4$ or KTP [194]) have been demonstrated. However, a direct comparison between the results achieved for different phase-matching configurations in terms of efficiency is problematic, as they were obtained with different optical setups and detection equipment.

In this chapter I discuss the basic spectral properties of type-0 and type-II quasi-phase-matched SPDC in ppKTP and present a conclusive comparison in terms of pair-generation efficiency, using the same optical setup. In light of applications in harsh environmental operating conditions, such as space, the suitability of using a free-running laser diode to pump the SPDC process is also evaluated. This chapter covers material published in Publication **A** and Publication **C**.

3.1 Quasi-Phase Matching in ppKTP

Efficient SPDC requires the signal and idler fields generated in different regions of the nonlinear crystal to interfere constructively along the propagation direction. This condition is known as the so-called phase-matching condition (Eq. 2.60). In anisotropic nonlinear materials phase matching can be achieved using birefringence to compensate the phase mismatch due to dispersion. This technique is known as birefringent phase matching (BPM), and can be achieved in both collinear and non-collinear type-I and type-II configurations [195]. In general,

birefringent phase matching is achieved by angle tuning the crystal, which severely constrains the choice of the nonlinear coefficient and propagation geometry. Furthermore, birefringent phase matching requires the polarization of at least one of the fields to be extraordinary, which results in Poynting vector walk-off [196, 197]. As the beams propagate through the crystal, this walk-off leads to a decrease in beam overlap, and thus significantly limits the maximum useful length of the nonlinear crystal.

A recently developed alternative approach is to compensate the phase mismatch by periodically modulating the crystal's nonlinearity. This technique, known as quasi-phase matching [196–198], can be used to compensate for arbitrary phase mismatch, as long as the required short poling periods can be readily engineered. Perfect quasi-phase matching requires a harmonic modulation of the crystal's nonlinearity with a period ($\Lambda = 2\pi/\Delta k$). In practice, however, quasi-phase matching is achieved by periodical inversion of the material's nonlinear coefficient, which leads to a reduction of the effective nonlinearity by a factor of $2/(\pi m)$, where m is an odd integer that denotes the phase matching order.

The additional degree of freedom introduced by the poling period significantly simplifies phase matching, and allows crystals to be designed to produce SPDC photon pairs for almost arbitrary wavelengths and operating temperatures, while using the material's largest nonlinear tensor coefficient to mediate the interaction. Furthermore, the interaction can be tailored such that pump, signal, and idler propagate collinearly along a principal axis of the nonlinear crystal. This eliminates spatial walk-off (non-critical phase-matching) and allows for the usage of longer nonlinear crystals as well as efficient coupling into single-mode fibers.

The entangled photon sources presented in the later chapters of this thesis are designed to generate photon pairs at wavelengths in the near infrared. The wavelength region around $\sim$810nm is considered optimal for free-space communication applications, taking into account atmospheric transmission, beam divergence over long-distance links, detector efficiency and the availability of compact LD pump sources (see section 1.2.3). A number of nonlinear materials, such as KTP, lithium niobate (LN), or beta barium borate (BBO) have previously been used to generate photon pairs in this wavelength region. Throughout this thesis we use KTP, due to its large nonlinearity, high transparency for pump wavelengths around 405nm, and its low susceptibility to photo-refractive damage. Furthermore, it has been shown that KTP can sustain the proton and gamma radiation and thermal vacuum fluctuations expected in space [199].

For collinear propagation along the crystallographic x-axis, KTP has three nonzero second-order tensor coefficients d_{ijk} [194], allowing for collinear type-0 ($Z_pZ_sZ_i$), type-I ($Z_pY_sY_i$), and type-II ($Y_pY_sZ_i$) quasi-phase-matched SPDC, by appropriate choice of the poling period.

Table 3.1 lists the required poling period for collinear phase-matching from 405nm to 810nm at room temperature, as well as the respective nonlinear coefficients. Note the interesting coincidence that the poling period required for first-order type-II QPM is very close to the required poling period for third-order QPM

Table 3.1: Required poling period (Λ) and nonlinear coefficients (d_{ijk}) for collinear SPDC in x-cut ppKTP [205, 206].

configuration	Λ [μm]	d_{ijk} [pm/V]
type-0 ($z_p z_s z_i$)	3.43	$\mathrm{d}_{zzz} \sim 18.5$
type-I ($z_p y_s y_i$)	1.96	$\mathrm{d}_{zyy} \sim 4.7$
type-II ($y_p y_s z_i$)	10	$\mathrm{d}_{yyz} \sim 3.9$

of the type-0 process. Hence, in type-II pair-sources in KTP, a background originating from the higher-order type-0 process can be expected. For standard applications this is usually considered an undesirable feature which could, however, be of interest in, for example, polarization-independent frequency conversion processes. Coincident phase-matching of higher order type-0 and type-I processes, on the other hand, could be used to directly generate polarization-entangled photons from a single crystal [200].

In the following sections we compare the theoretical and experimental performance, such as pair rates, spectral bandwidth, and temperature tuning characteristics for SPDC photon pairs generated in x-cut flux-grown ppKTP crystals pumped by a 405-nm fiber-coupled continuous-wave laser diode. In terms of spectral characteristics, type-0 and type-I SPDC [201, 202] typically show comparable temperature dependence and bandwidths, as both involve co-polarized signal and idler photons. This is contrasted by the spectral characteristics of the type-II process, in which the generated photons are orthogonally polarized [203, 204]. Since ppKTP crystals for type-I SPDC show similar spectral characteristics to type-0 SPDC, but have a smaller nonlinear coefficient and are harder to fabricate due to the shorter poling period (see Table 3.1), type-I SPDC is omitted from the following comparison.

3.2 Comparison of Type-0 and Type-II SPDC in ppKTP

In order to compare type-0 and type-II SPDC in ppKTP in theory and experiment, the pair-generation efficiency of a 20-mm type-0 and type-II sample were compared in the same optical setup; the crystals were mounted side-by-side and could be interchanged using a translation stage (see Fig. 3.2). The pump beam was focused to a Gaussian beam waist of 150 μm at the center of the crystal, and the signal and idler photons were separated using a polarizing beam splitter (type-II) or a dichroic mirror (type-0). The photon pairs were then collected using single-mode fibers with a collection waist of 80 μm. For the assessment of the spectral characteristics (Fig. 3.1), the photons were guided to a high-resolution single-photon spectrometer. For the measurement of the pair rates the single-mode fibers were connected to two silicon-based single-photon detectors, and photon pairs were identified via their arrival times, using a coincidences measurement with a fast FPGA-based timing logic.

The theoretical spectral bandwidth and the center wavelengths were calcu-

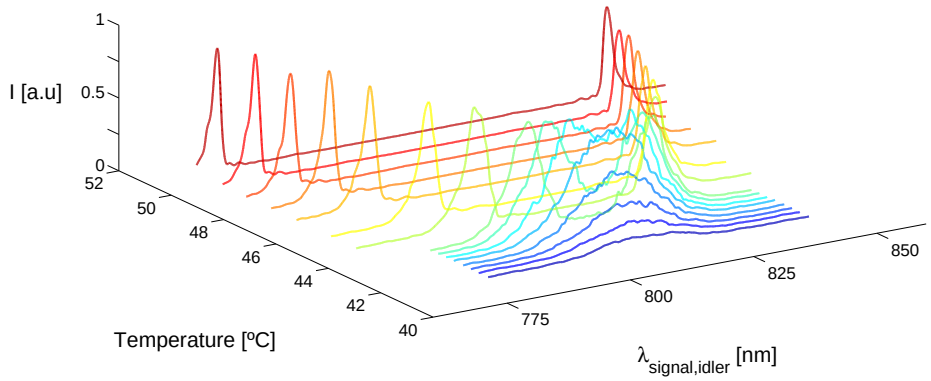

Figure 3.1: Experimentally observed normalized SPDC spectra for 20-mm ppKTP crystal (poling period=3.425μm) pumped with a 405.4 nm CW laser diode for varied phase-matching temperatures.

lated using the full wavelength dependence of the phase-matching function (no first-order approximation). There exist a number of material coefficients for the temperature- and wavelength-dependence of the refractive indices in KTP [207–212]. The best agreement with the experimental data was obtained using the wavelength dependence from Ref. [207], the temperature dependence of the refractive indices from Ref. [210], and the thermal expansion coefficients from Ref. [213].

3.2.1 Temperature-dependent spectral properties

The center wavelengths ($\lambda^0 = 2\pi c/\omega^0$) that fulfill the phase-matching condition ($\Delta k = 0$) are depicted in Fig. 3.3 as a function of temperature. Notice that the temperature dependence of the center wavelengths for type-II SPDC:

$$|\frac{\partial \lambda_s}{\partial T}|_{810nm}^{type-II} \sim 0.2nm/K \tag{3.1}$$

is more robust with regard to temperature changes compared to the type-0 process:

$$|\frac{\partial \lambda_s}{\partial T}|_{780nm}^{type-0} \sim 3nm/K. \tag{3.2}$$

The FWHM bandwidth in cw-pumped collinear SPDC (Fig. 3.4) is determined by crystal length and group velocity mismatch of signal and idler photons (Eq. 2.67) and thus generally decreases with wavelength non-degeneracy ($\lambda_s^0 - \lambda_i^0$). Consequently, a large bandwidth is observed for the co-polarized signal and idler photons in type-0 and type-I SPDC close to degeneracy ($\lambda_s^0 = \lambda_i^0 = \lambda_p^0/2$). For the type-II process, on the other hand, the group velocities of orthogonally polarized signal and idler typically differ significantly at wavelength degeneracy, resulting in a comparatively small bandwidth. Note that while the large bandwidth of the type-0

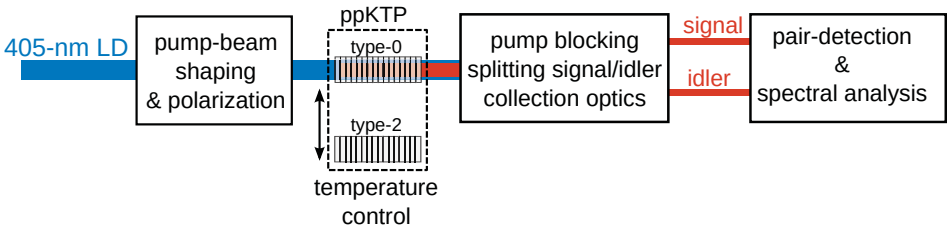

Figure 3.2: Schematic of experimental setup for comparison of spectral/efficiency characteristics of type-0 and type-II SPDC in 20mm of ppKTP.

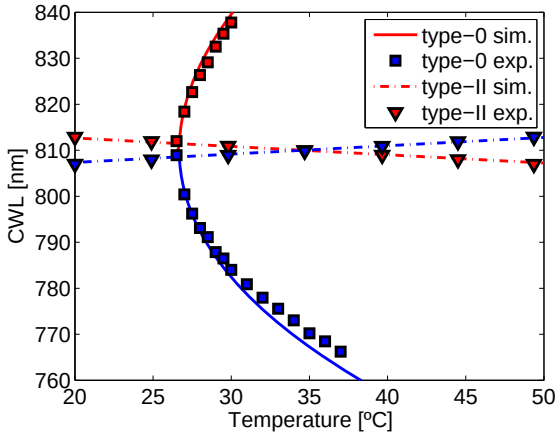

Figure 3.3: Spectral characteristics of type-0 and type-II SPDC in 20mm of ppKTP: The phase-matched cwl of signal (blue) and idler (red) of type-0 SPDC (squares) show a much stronger temperature dependence than type-II SPDC (triangles). The theoretical curves were calculated using the material coefficients for KTP [207, 210], whereby the poling period was tuned to coincide with the degenerate phase-matching point.)

process close to degeneracy (Eq. 2.68) is disadvantageous for most standard applications (e.g. quantum cryptography), this region could be useful for achieving ultra-short temporal correlations (section 2.3.3, [214, 215]) and improving resolution in, for example, quantum optical coherence tomography [216, 217], quantum ranging, or clock synchronization with dispersion cancellation [218].

For both type-0 and type-II SPDC, the spectral bandwidths depicted in Fig. 3.3 are in good agreement with the values calculated using the refractive indices from the Sellmeier material coefficients for KTP [207]. The experimentally observed temperature dependence of the center wavelengths, however, differs from the calculated behavior, most likely due to the inaccuracy of the refractive-index temperature derivatives [210] at the pump wavelength.

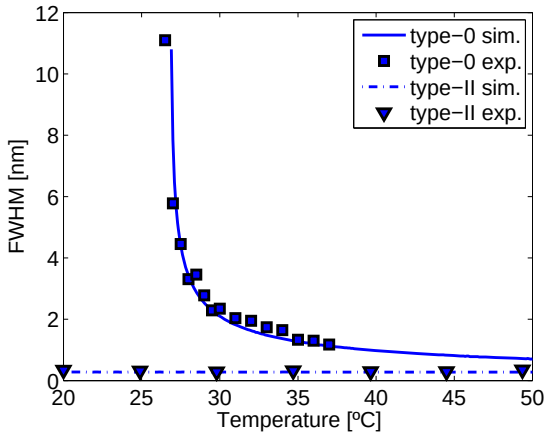

Figure 3.4: Spectral characteristics of type-0 and type-II SPDC in 20mm of ppKTP: The FWHM bandwidth of the type-0 SPDC shows a stronger temperature dependence than the type-II process. For a relative comparison of bandwidth, see also Tab. 3.2. The theoretical curves were calculated using the material coefficients for KTP ([207, 210]), whereby the poling period was tuned to coincide with the degenerate phase-matching point.)

Table 3.2: Performance characteristics of SPDC in ppKTP.

configuration	λ_s, λ_i	$\Delta\lambda_s$	R_c/P_0 [Mcp/mW]	$(dR_c/d\lambda)/P_0$ [Mcp/mW/nm]
type-0	784nm,839nm	$\sim$2.3nm	1	0.46
type-II	810nm,810nm	$\sim$0.3nm	0.008	0.026

3.2.2 Pair-generation efficiency

Aside from the differences in spectra and temperature-tuning characteristics, the pair-generation efficiency between type-0 and type-II SPDC also differs significantly due to the different nonlinear coefficients (Tab. 3.1). The pair-generation efficiency was quantified in terms of the spectral brightness $((dR_c/d\lambda)/P_0)$, that is, the number of generated pairs per mW of pump power (P_0) and per nm of generated bandwidth ($\Delta\lambda$), or the total pair-rate ($R_c \approx (dR_c/d\lambda) \times \Delta\lambda$). For type-0 SPDC the observed spectral brightness was approximately 20 times higher than for type-II QPM (see Tab. 3.2), in good agreement with the expected behaviour due to the different nonlinear coefficients $(d^2_{\mathrm{zzz}}/d^2_{\mathrm{yyz}})$. In agreement with Eq. 2.65, the observed peak spectral brightness is almost independent of wavelength degeneracy and bandwidth, except for the type-0 process and temperatures below the wavelength-degeneracy point where the type-0 collinear QPM condition is no longer fulfilled. The total pair rate of type-0 SPDC, however, peaks close to the degeneracy point and is two orders of magnitude higher than that of the type-II sample, due to the significantly larger bandwidth.

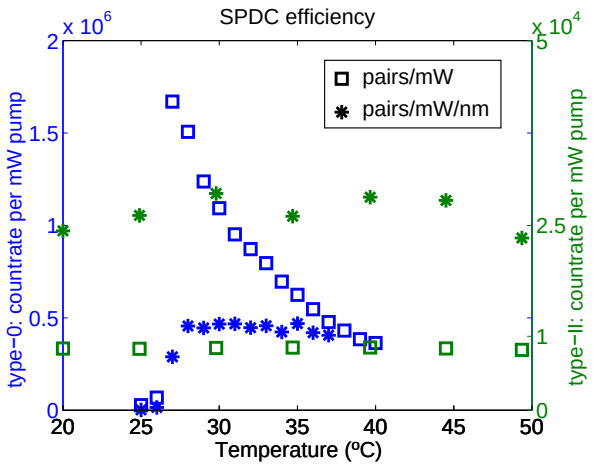

Figure 3.5: Pair-generation efficiency in type-0 (blue) and type-II (green) SPDC: The spectral brightness [Mcps/mW/nm] remains almost constant over observed temperature range for both QPM configurations (once the phase-matching condition for type-0 is met at T=26.5 °C). Since the total pair rate [Mcps/mW] is proportional to the temperature-dependent bandwidth (Fig. 3.3), it decreases strongly with temperature for type-0 SPDC.

3.3 SPDC with a Multi-Mode Pump

The suitability of employing multi-mode free-running (FR) cw pump laser diodes (FWHM bandwidth $\sim$ 1nm) for SPDC has not yet been extensively investigated, since single-mode lasers (FWHM $<$500 MHz) are readily available in most quantum optics laboratories. However, for applications in space, the increased compactness and relaxed stabilization requirements, as well as higher possible pump powers, could make FR LD pumped SPDC a very attractive option. In order to evaluate the feasibility of using FR LD pumps for applications in quantum communication and cryptography, let us first analyze the expected impact on spectral properties and efficiency of the SPDC process.

3.3.1 Theory of SPDC with a multi-mode pump

Consider an FR LD consisting of several spectral modes ω_p^ν, centered around ω_p^0:

$$s(\omega_p) \sim \sum_\nu I^\nu \delta(\omega_p - \omega_p^\nu) \tag{3.3}$$

where I_ν is the weight of the ν-th pump mode in the pump spectrum. Since the frequency modes of an FR LD have no fixed phase relationship, the total resulting SPDC spectrum of the signal (idler) photons $S(\omega_{s(i)})$ is obtained by incoherently summing the spectral intensity distributions $S_\nu(\omega_{s(i)})$ of SPDC from all phase-matched longitudinal pump modes (see Fig. 3.6):

$$S(\omega_{s(i)}) = \sum_\nu I^\nu S_\nu(\omega_{s(i)}) \tag{3.4}$$

Each of these contributions $S_\nu(\omega_{s(i)})$ is centered about $\omega^\nu_{s(i)}$ and has a spectral bandwidth ($\Delta\Omega_\nu$). Additionally, when the pump consists of several discrete (or continuous) spectral modes, the spacing of the spectral peaks of down-converted signal (idler) photons ($\omega^{\nu+1}_{s(i)}, \omega^\nu_{s(i)}$), which were generated by neighboring pump modes ($\omega^{\nu+1}_p, \omega^\nu_p$) is increased with respect to the initial spectral mode-spacing of the pump photons. The spacing of the phase-matched center wavelengths of the signal (idler) photons with respect to the pump modes, can be approximated as:

$$\left(\omega^{\nu+1}_{s(i)} - \omega^\nu_{s(i)}\right) \approx \frac{\partial\omega_{s(i)}}{\partial\omega_p}|_{\omega^\nu_{s(i)}} \left(\omega^{\nu+1}_p - \omega^\nu_p\right) \tag{3.5}$$

where, approximating the phase mismatch to first order (Section 2.3.2), we have:

$$\frac{\partial\omega_{s(i)}}{\partial\omega_p}|_{\omega^\nu_{s(i)}} = \frac{1/u_p - 1/u_{s(i)}}{1/u_s - 1/u_i} \tag{3.6}$$

where $u_{s,i,p}$ denote the group velocities for signal, idler, and pump, respectively. Depending on the phase-matching characteristics of the nonlinear material, a small pump bandwidth can result in an extremely large spectral SPDC bandwidth.

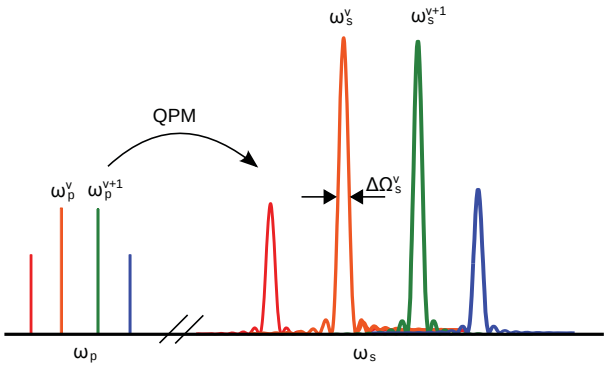

Figure 3.6: Mapping for spectral properties of FR pump to SPDC spectra.

For ppKTP and signal and idler wavelengths of 780nm and 840nm respectively, the effect is significantly larger for type-0 QPM and type-I QPM, than for type-II QPM (Tab. 3.3). Consequently, in addition to the spectral bandwidth of individual modes being larger (see Fig. 3.3), the stronger pump-wavelength dependence of the center wavelengths leads to a significantly increased spectral bandwidth for type-0 and type-I SPDC. Figure 3.7 and Figure 3.8 depict the spectra for type-0 and type-II QPM in KTP with a cw pump consisting of four longitudinal modes.

While the larger bandwidth is a disadvantage to standard quantum optics applications, it might have potential application in metrology, since it allows a person to infer the pump spectrum with high resolution, by measurement of the signal and idler with a low-resolution spectrometer [219]. As a numerical example, the large

Table 3.3: Pump-frequency derivatives of phase-matched center frequencies for different phase-matching configurations in ppKTP.

configuration	$\frac{\partial \omega_s^0}{\partial \omega_p}$	$\frac{\partial \omega_i^0}{\partial \omega_p}$
type-0	~ 33	~ 34
type-I	~ 57	~ 58
type-II	~ 2	~ 3

type-I amplification factor would allow resolving the pump spectrum to < 4 pm, using a spectrometer with a resolution of only 1 nm!

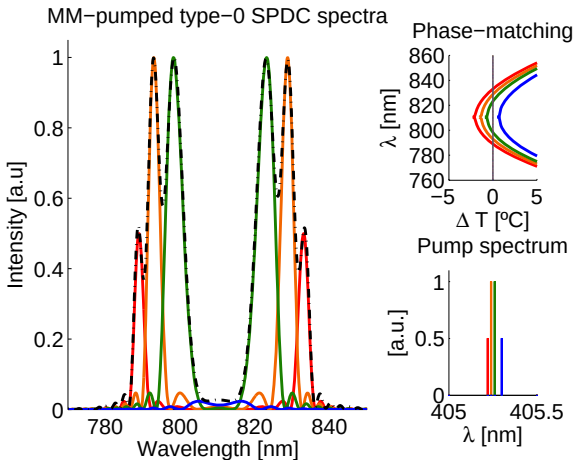

Figure 3.7: Qualitative explanation of type-0 SPDC spectra with a multi-mode pump: At the reference temperature $\Delta T = 0$, multiple spectral modes of the pump are phase-matched at different center-wavelengths, resulting in a broad-band SPDC response (dashed black envelope). The longest wavelength of the pump is not phase-matched.

In addition to the spectral characteristics, the total flux of photon pairs generated is also affected when using an FR LD; The rate of photon pairs generated by the ν-th pump mode is proportional to the respective down-conversion bandwidth ($R_c^\nu \propto I^\nu \Delta\Omega_s^\nu$), which can vary strongly over the pump bandwidth, in particular for type-0 SPDC. In this case the total pair-rate $R_c \propto \sum_\nu I^\nu \Delta\Omega_s^\nu$ can significantly differ from that achieved with a single-frequency pump of the same total power $I = \sum_\nu I^\nu$. For type-II SPDC with typical FR LD bandwidths of $\sim$ 1nm, however, the down-conversion bandwidth remains almost constant for the different pump modes, and the total pair rates can be expected to be of similar magnitude as when using a single-mode pump.

3.3.2 Experimental results

In order to corroborate these theoretical findings, an experimental comparison between the spectral properties and efficiency of single-mode and multi-mode pumping was performed. For the experimental comparison to take place under otherwise

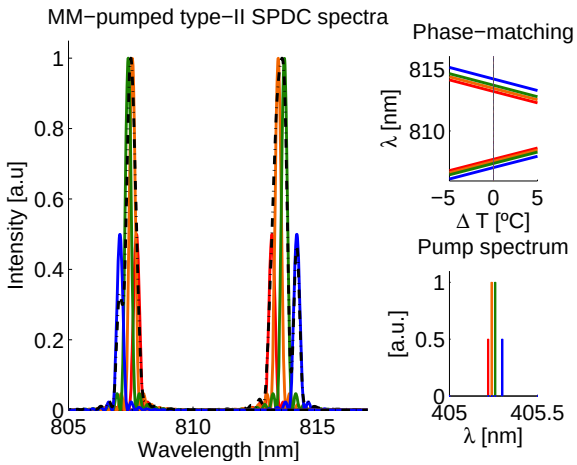

Figure 3.8: Qualitative explanation of type-II SPDC spectra with a multi-mode pump: At the reference temperature $\Delta T = 0$, multiple spectral modes of the pump are phase-matched at different center-wavelengths, resulting in a broad-band SPDC response (dashed black envelope). In contrast to the type-0 SPDC, for the type-II process all pump components contribute to the observed SPDC signal. Nevertheless, due to the QPM characteristics of type-II SPDC in ppKTP, the resulting SPDC bandwidth is still significantly smaller than that of the type-0 process.

equal conditions, multi-mode and single-mode operation were achieved by detuning the temperature of the same LD. The pump spectra (inset in Fig. 3.10) were monitored using a high-resolution optical spectrum analyzer, and the SPDC spectra were measured using a diffraction-grating-based, tunable filter (FWHM passband 0.4nm). The experimental observations were in good agreement with the qualitative analysis of the previous paragraph. Two examples of multi-mode-pumped SPDC spectra are depicted alongside the single-mode-pumped spectrum as a reference in Figs. 3.9 and 3.10, for type-0 and type-II SPDC, respectively. Figures 3.9 and 3.10 also include the SPDC spectra calculated for the multi-mode pump profiles which were measured with the optical spectrum analyzer. The peaks resulting from the pump's most pronounced spectral modes can be identified in the spectra of both type-0 and type-II SPDC. Note that the best agreement between calculated and experimental spectra was obtained using poling periods that slightly deviated from the manufacturer's specifications. The difference in the relative weights of calculated and experimental SPDC peaks is the result of wavelength-dependent losses, due to chromatic aberrations in the collection optics and the wavelength-dependent efficiency of the spectrometer.

The pair rates measured for type-0 SPDC with a multi-mode pump were significantly lower than those measured with the single-mode pump, even when the temperature was chosen to phase-match the entire pump bandwidth. This difference in efficiency was in part due to the aforementioned chromatic aberrations in the single-mode collection optics. Additionally, for type-0 SPDC the short wavelength spectral components of the pump lead to a smaller down-converted bandwidth (due

to larger non-degeneracy of the generated signal and idler for fixed crystal temperature) and thus contribute less pairs to the total broadband SPDC signal, as outlined in the previous paragraph. In addition to the decreased efficiency, another point of practical interest is the achievable entanglement visibility. Since the SPDC spectrum is distributed over a very large spectral range for the type-0 ppKTP crystal, polarization mode dispersion could make it difficult to achieve high-visibility polarization entanglement.

As expected, type-II SPDC did not show such a strong change in efficiency and spectral properties.

In conclusion, a type-II phase-matched crystal pumped with a high-power FR LD could provide a more robust choice for applications in out-of-the-lab operating conditions. High-visibility polarization entanglement using FR laser diodes has been demonstrated for BBO [89], and we expect that these results can be extended to ppKTP. The criticality of required compensation techniques, as well as the suitability of various entanglement-producing configurations (crossed-crystal [88], double-pass [220], Sagnac-loop [174]) for the case of FR-LD-pumped ppKTP is to be assessed in further studies. These results on the spectral characteristics are complemented by the investigation into the coherence properties of multi-mode cw pumped SPDC [221] and could be of great interest for applications in (quantum-) metrology.

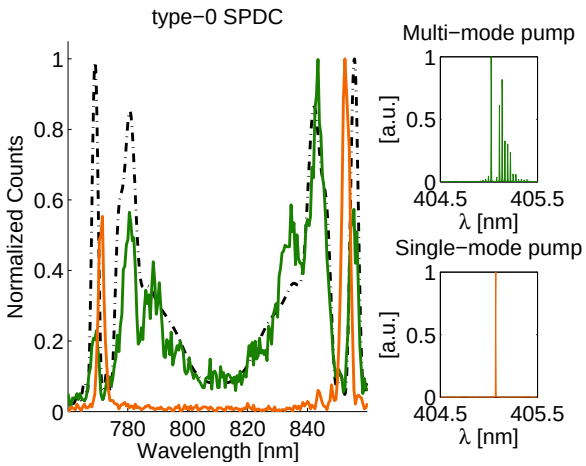

Figure 3.9: Normalized SPDC spectra with multi-frequency- (experiment: green, theory: dashed black), and single-frequency pump (experiment: orange) for type-0 QPM in 11mm ppKTP. The differences between theory and experiment are the result of wavelength-dependent loss in the single-mode collection optics and spectrometer. For a multi-frequency pump, the type-0 SPDC spectrum covers a spectral range that is too broad for many applications, and would require strong spectral filtering.

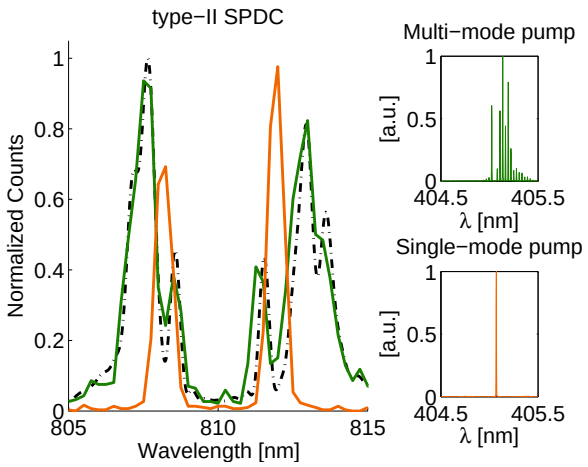

Figure 3.10: Normalized SPDC spectra with multi-frequency- (experiment: green, theory: dashed black), and single-frequency pump (experiment: orange) type-II QPM in 15mm ppKTP. The differences between theory and experiment are the result of wavelength-dependent loss in the single-mode collection optics and spectrometer. For a multi-frequency pump, type-II SPDC spectrum is relatively robust with respect to the large pump bandwidth and could still be feasible option for e.g. free-space quantum communications and other standard quantum optics applications.

3.4 Conclusions

In this chapter we discussed the main spectral properties and efficiency of pair generation in ppKTP via SPDC with a 405-nm cw pump. A comprehensive comparison between type-II and type-0 QPM configurations in terms of efficiency, as well as temperature- and pump-wavelength-dependent spectral properties was performed. As expected from the different nonlinear coefficients, type-0 SPDC in ppKTP is significantly more efficient than the type-II process. However, type-II QPM in ppKTP is more robust with respect to temperature drifts. Furthermore, type-II QPM is affected less by larger pump bandwidth, and allows us to generate comparatively narrow SPDC bandwidth, even when pumping with a free-running cw laser diode. The use of an FR pump could thus be particularly attractive, due to relaxed requirements in terms of current and temperature stabilization, compactness, and the generally higher powers compared to cw operation.

We, therefore, see that both type-0 and type-II SPDC have their own characteristic merits. For a ground-based quantum communication terminal, where there is still some temperature stability (while not necessarily laboratory conditions), a type-0 SPDC source seems most appropriate, due to the higher possible pair rates. Also, the higher degree of wavelength tunability can be seen as an advantage in such applications. Furthermore, the larger spectral bandwidth, and correspondingly ultra-short temporal correlations, could be of interest for ultra-precise quantum ranging experiments. In the harshest of operation conditions, however, such as space flight operation for example, the increased temperature stability and the

possibility of using a free-running laser diode pump are factors that favor a type-II ppKTP SPDC source.

Chapter 5

Entangled Photon Source for Quantum Communications

Over the last few years, the European Space Agency (ESA) has shown great interest in the development of quantum communication terminals for applications in space, and funded a number of research projects to meet this end. This chapter summarizes the main results of the EQU0 project (ESA Contract No:22542/09/NL/SFe), in which the Optoelectronics group at ICFO oversaw the design, engineering, and testing of an entangled photon source (EPS) which addresses the critical requirements of free-space experiments, and ultimately space flight operation. The experimental evaluation of the source delivered to ESA was published in Publication **A**.

5.1 Performance Requirements

The main performance characteristics the source had to fulfill are summarized in Table 5.1. The EQU0 project was focused on achieving high brightness (pairs/s or bit rate) as well as high visibility (strong correlation, i.e. low quantum bit error ratio). Additionally, the source was required to meet the added constraints of robustness and compactness; the hardware and driving electronics had to be fitted on a compact breadboard, for its use in out-of-the lab experiments 5.1. Furthermore, the source was fiber coupled in order to ensure minimum beam diffraction over free-space links, and provide a versatile plug-and-play interface, which would allow the source to be exchanged between experiments without the need for realignment. The operational wavelength range was determined, taking into account the combined effects of beam diffraction, atmospheric transmission, and the high detection efficiency of low-timing-jitter SPADs (see Chapter 1).

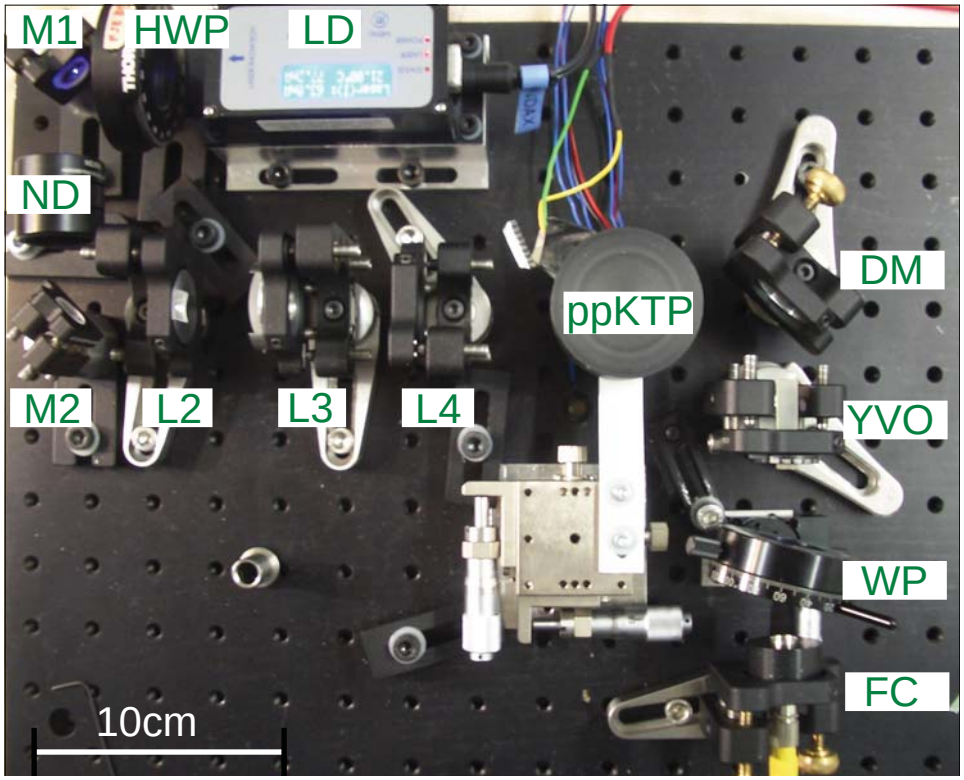

Figure 5.1: Photo of the compact EQU0 entangled photon source, delivered to the European space agency. The source was fitted onto a compact breadboard, and consisted of a 405-nm laser diode module (LD), a 405-nm half-wave plate (HWP), a neutral density filter to adjust the pump power (ND), two beam-steering mirrors (M1,M2), beam-shaping optics (L2,L3,L4), two temperature-controlled ppKTP crystals (ppKTP), a dichroic mirror (DM), an yttrium orthovanadate compensation crystal (YV0), a wave plate (WP), and a compact fiber coupler (FC). The signal and idler photons were separated into two spatial modes using a fiber-based wavelength division multiplexer (WDM - not depicted). For details on the functionality refer to the following sections.

Optical Requirements	Requirement	Goal
Wavelength	TBD	750nm - 850nm
Optical Bandwidth	$< 10nm$	$< 3nm$
Pump type	laser diode	-
Type of entanglement	TBD	Polarization
Visibility	$> 90\%$	$> 95\%$
Spectral brightness	> 40 kcps/mW/nm	> 10 Mcps/mW/nm
Optical Interface	single-mode fiber	-
Environmental Requirements	Requirement	Goal
Operational temperature range	20$\pm$ 5 deg C	-
Operational relative humidity range	50$\pm$ 20 %	-
Vacuum environment	N/A (ambient pressure)	-
Radiation	N/A	-
Physical Requirements	Requirement	Goal
Total mass	$\leq$15 kg	$\leq$5 kg
Total size	$\leq$ 500 x 500 x 100 mm^3	$\leq$ 250 x 250 x 100 mm^3
Total power consumption	$\leq$30 W (peak)	$\leq$20 W (peak)

Table 5.1: Statement of Work (SOW) performance requirements for EQU0 entangled photon source.

5.2 Crossed-Crystal Configuration

Over the last two decades, numerous schemes for polarization entanglement of photon pairs generated by SPDC have been proposed and demonstrated. Amongst these, so-called common-path configurations stand out, as they do not require active interferometric path stabilization (see also section 6.1). In a common-path configuration the pump beam that drives the secondary SPDC emission propagates along the same optical path as the primary pair-emission process, and optical path-length fluctuations are effectively auto-compensated.

For the EQU0 project, our approach was based on collinear non-degenerate down-conversion emission from crossed crystals (see section 2.4.1), as demonstrated in [89], pumped by a 405-nm cw LD. With respect to [89], which utilized type-I SPDC in BBO, here we used the more efficient type-0 process in ppKTP.

The crossed-crystal (or “sandwich”) scheme uses two mutually orthogonally oriented ppKTP crystals for type-0 QPM from 405-nm (pump) to 783nm (signal) and 837 nm (idler), placed in sequence. The pump beam is polarized diagonally with respect to the two crystallographic z-axes, such that an SPDC process is equally likely to occur in the first crystal (in state $|H_sH_i\rangle$) or in the second one (in state $|V_sV_i\rangle$). Polarization entanglement is observed if the two emission processes are indistinguishable in all other degrees of freedom .

5.3 Technical Realization of EPS

Compact pump source

After consulting numerous manufacturers, the Ondax SureLock 405-nm volume-holographic-grating-stabilized laser diode was the best suited option in terms of price, spectral bandwidth, and maximum output power. The radiation spectrum obtained with a high-resolution spectrum analyzer is depicted in Figure 5.2. The small footprint of 100x40 mm^2 enables easy integration of the laser module into the EPS breadboard. Since the output beam height is only 19 mm, an aluminum pedestal was manufactured to adjust the beam height to 50 mm. The main limitation is that neither output power nor center wavelength are tunable. For single mode operation (lindwidth $<$ 160 MHz), the module is locked to an output power of 40mW and a center wavelength of 405.4nm. The collimated output beam (900 μm x 400 μm) shows almost perfect Gaussian beam profile, with an $M^2 \sim 1$.

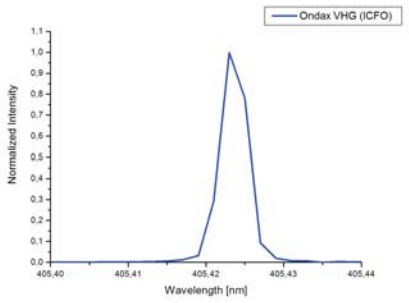

Figure 5.2: Spectrum of Ondax pump laser, acquired with optical spectrum analyzer.

Pump and collection optics

In addition to high entanglement visibility, special emphasis was put into optimization of the brightness (pairs/s) of the source. According to theoretical considerations discussed in Chapter 4, the optimal pump waist size for a 20-mm-long ppKTP crystal is $\sim$16μm, and the optimal output coupling mode waist is $\sim$24μm. The design goals were to enable low M^2 focusing of the pump, thus maintaining Gaussian single mode beams, while also matching the requirements for compactness and robustness.

The pump beam was set to a linear polarization of $\sim$45°using a zero-order half-wave plate with its optical axis oriented at 22.5°. The wave plate was placed directly after the output of the pump laser. In order to achieve a spot size close to the theoretical optimum ($\sim$19 μm) at the center of the ppKTP crystals, while maintaining a compact configuration, the ellipticity of the collimated LD output (0.45x0.2 mm^2) was corrected using a 2:1 telescope, consisting of two cylindrical lenses (L2,L3). The then circular and collimated pump beam was focused to the

center interface of the two crossed ppKTP crystals via a spherical lens (L4) with a focal length of f =75mm. The SPDC was reflected to the output fiber coupler via a dichroic mirror. The output coupler consisted of a single aspheric lens (L5) with a focal length f =11mm in an adjustable-focus mount (Fig. 5.4). The setup was arranged in a compact folded geometry.

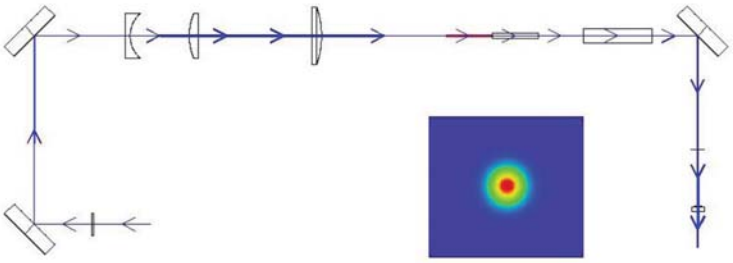

Figure 5.3: 2-D image of Zemax modeled design. Inset circular beam shape at crystal center.

Figure 5.4: Custom-made miniature output coupler with adjustable focus, manufactured by qutools GmbH. The distance between the aspheric lens and the fiber tip could be adjusted using a spanner wrench (bottom left).

Nonlinear crystals

The source uses two 20-mm ppKTP crystals with a poling period of 3.425 μm, specified for type-0 collinear phase-matching from 405 nm to 783nm (signal) and 837 nm (idler) at approximately 30°C. A total of 6 flux-grown ppKTP crystals were acquired from Raicol Crystals Ltd., and compared in terms of efficiency and spectral characteristics. Even though the ppKTP crystals were grown from the same batch and poled using the same poling mask, the comparative measurements revealed significant differences in terms of efficiency and spectral characteristics. Furthermore, for each sample, the efficiency was dependent on the lateral position

of the pump beam in the crystal (see Fig. 5.5). The peak efficiency of the two crystals used in the source differed by a factor of approximately two, depending on the location of the pump beam in the crystal. This difference in efficiency had to be compensated in order to achieve balanced SPDC emission from the two crystals, as required for the generation of a maximally polarization-entangled state. This was achieved by rotating the pump polarization toward the z-axis of the less efficient of the two crystals, which led to an overall decrease in efficiency.

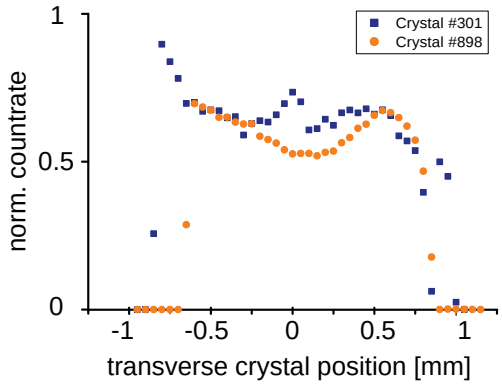

Figure 5.5: Coincidence count rate as the pump beam is scanned transversally through two PPKTP crystals. The spatial non-uniformity is clearly visible.

Spectral filtering

In order to achieve high entanglement visibility, it is critical that the spectra of SPDC emission from the two ppKTP crystals be completely indistinguishable (see Chapter 2). The two crystals chosen as a result of the comparative efficiency measurements, however, phase-matched at different center wavelengths when kept at equal temperature. Further analysis showed that the spectrum produced by each crystal varied as the beam was displaced along the crystal aperture; the center wavelength of the spectrum could be shifted by up to 2 nm as the crystal was laterally displaced along the pump beam.

The maximally achievable entanglement visibility in the presence of spectral which-crystal information can be estimated via the overlap integral of the spectral intensity profiles. Note that the spectral intensity overlap (as opposed to the amplitude overlap in section 2.4) gives only a loose upper bound on the visibility, as it does not account for inhomogeneity in the spectral phase profiles of the two SPDC emissions.

In order to increase the spectral overlap the crystals were maintained at a temperature difference of 0.25°C. However, even for equal center wavelengths the respective spectra were clearly distinguishable (see Fig. 5.6), and the spectral overlap was merely $\sim 91\%$. In order to mitigate the remaining spectral differences, a narrow-band spectral filter with a center wavelength of 783nm and an FWHM pass-

band of $\sim$ 3nm was placed after the WDM in the signal path of the polarization analyzer. The spectral intensity overlap after filtering increased to $> 99\%$. Note that the narrow IF filter is placed only in the signal path, since, when measured in coincidence, filtering one arm with a narrow IF effectively filters the entangled pair (due to the anti-correlation of the signal and idler spectra).

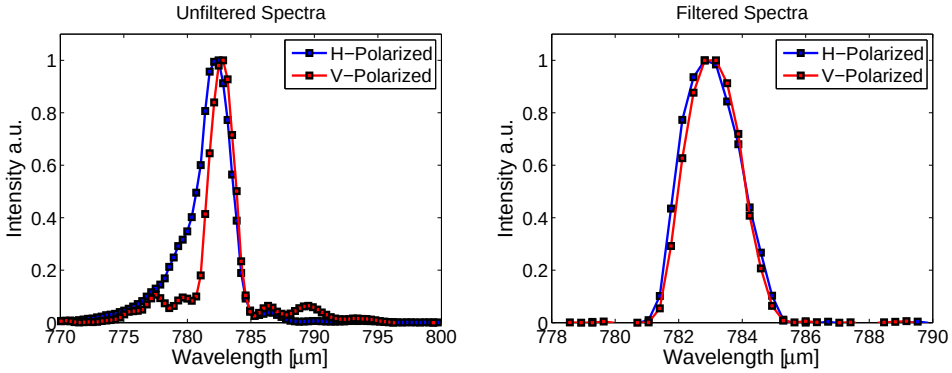

Figure 5.6: SPDC spectra of horizontally and vertically polarized signal photons before and after filtering with a 3.5 nm FWHM IF filter. The spectra were recorded with the crystals maintained at phase-matching temperatures of 28.3 °C (H-Polarization) and 28.1 °C (V-Polarization). The spectral intensity overlap integrals were calculated to 91 % and >99% for the unfiltered and filtered SPDC profiles, respectively.

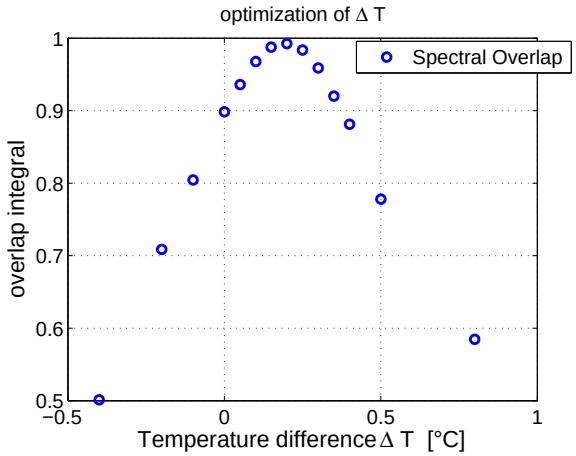

Figure 5.7: Spectral overlap integral calculated from filtered spectral data (upper bound for the entanglement visibility) as a function of crystal temperature difference.

Double oven

A compact double-oven assembly that allowed for individual temperature control of the two nonlinear crystals was manufactured by qutools GmbH (Fig. 5.8). The

oven consisted of two copper bases which were separated by a 1-mm gap of air. These bases were attached to the hot face of two Peltier elements, whose cold face was connected to a heat sink which was formed by a solid aluminum base. The aluminum base was mounted on top of a pillar mount with adjustable height. The temperature of the two ovens were read out via two 10 kΩ thermistors, and the temperature was set using two compact custom-made temperature controllers, each with a long-term temperature stability of $<$0.1 °C. The ppKTP crystals were held in place by applying light pressure to a thin aluminum slab, which pushed the crystals against the copper base. A removable cover could be placed on top of the oven, to protect the crystals and ensure better thermal stability.

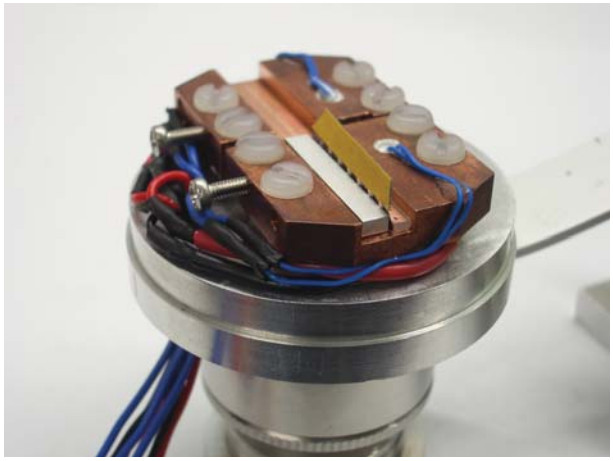

Figure 5.8: A custom double-oven, manufactured by qutools GmbH, allowed for separate temperature control of the ppKTP crystals. Foto courtesy of Pavel Trojek, qutools GmbH.

Phase plate

The relative phase of the entangled state was set using a 200μm-thick piece of YVO_4 crystal, which was angle-tuned by rotation about its optical axis. The optical axis was aligned parallel to the Z-axis of one of the PPKTP crystals. Due to birefringence, this results in a relative change in the optical path length for horizontally and vertical polarized photons. The wave plate can be located in either the SPDC or pump path, since the relative phase of the pump polarization is directly transferred to that of the entangled state. For a crystal with a thickness d, the relative phase (ϕ) introduced as a function of the angle of incidence on the crystal (δ) reads:

$$\phi(\delta, d) = \frac{2\pi}{\lambda_p} \frac{n_e - n_o}{\cos(\delta)} d \tag{5.1}$$

where λ_p denotes the pump wavelength, and n_e and n_o denote the extra-ordinary and ordinary index of refraction, respectively. The range of angle tuning required

for a full 360°phase retardation is approximately 8°. Note that high-quality AR-coating of the wave plate is critical in order to avoid etalon effects (fluctuations in the transmitted power due to interference) and polarization-dependent losses.

Figure 5.9: A 200μm-thick YVO_4 with an aperture of 1×1cm^2 was fixed inside a miniature rotation mount, such that the optical axis could be aligned with respect to that of the nonlinear crystals (i.e. perpendicular to the optical table). The wave plate was fixed on a miniature rotation platform, and the relative phase of the entangled state was adjusted by angle tuning the wave plate about its optical axis.

Compensation crystal

As a consequence of the crossed-crystal geometry, the $|H_sH_i\rangle$ pairs generated in the first crystal acquire an additional wavelength-dependent phase shift relative to the $|V_sV_i\rangle$ pairs emitted from the second ($|\Psi\rangle = |V_sV_i\rangle + e^{i\phi(\lambda_s,\lambda_i)}|H_sH_i\rangle$). The compensation of this relative phase, by placement of birefringent compensation crystals, was already discussed in Chapter 2. Here we follow essentially the same approach, but take into account the full wavelength dependence of the refractive indices, using the Sellmeier material coefficients for KTP and YVO_4 (no first-order approximation). The accumulated phase difference of horizontally and vertically polarized signal and idler photons at the output of the second crystal reads:

$$\phi(\lambda_s,\lambda_i) = \phi_p + \phi_s^H + \phi_i^H - (\phi_s^V + \phi_i^V) = \phi_p + 2\pi L\left(\frac{n_y(\lambda_s)}{\lambda_s} + \frac{n_y(\lambda_i)}{\lambda_i}\right) \quad (5.2)$$

For two 20-mm ppKTP crystals pumped by 405-nm cw laser, this leads to strong variations of the relative phase depicted in Fig. 5.10. In order to counteract this de-phasing effect, a YVO_4 crystal is inserted after the down-conversion

crystals. The optical axis of the YVO_4 is oriented parallel to the phase-matched axis of the ppKTP crystal, whereby the relative alignment of the optical axis of the compensation crystal is critical. In order to have better control over the angular orientation and alignment, the compensation crystal was mounted in a miniature rotation mount which was fixed to a tip-tilt kinematic mirror mount (Fig. 5.11). For a length of 30.01 mm, the difference in dispersion between the ordinary and extraordinary indices of refraction of YVO_4 leads to a wavelength-dependent phase $\phi_C(\lambda_s, \lambda_i)$. Adding the phase shift introduced by the compensation crystal:

$$\phi_C(\lambda_s, \lambda_i) = 2\pi \times L_{YVO} \left[\frac{n^{(o)}(\lambda_s)}{\lambda_s} + \frac{n^{(o)}(\lambda_i)}{\lambda_i} - \left(\frac{n^{(e)}(\lambda_s)}{\lambda_s} + \frac{n^{(e)}(\lambda_i)}{\lambda_i} \right) \right] \tag{5.3}$$

flattens the wavelength-dependent phase over a broad spectral range.

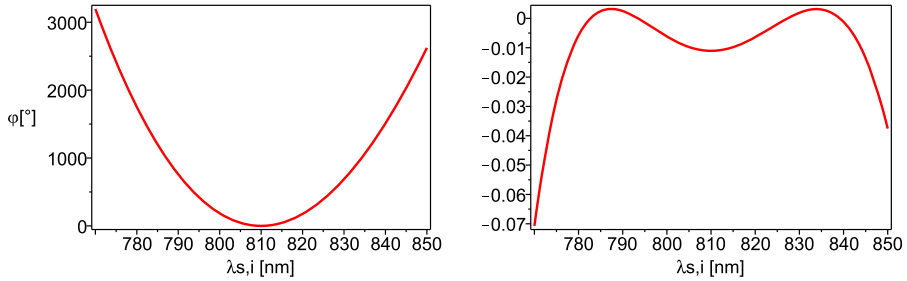

Figure 5.10: (left) Strongly varying phase dependence for 2x20 mm PPKTP due to additional chromatic dispersion experienced by photon pairs emitted in first crystal. (right) Flattened dependence after compensation with 30 mm YVO_4 crystal, with negligible variation over broad spectral range; note the difference in scale.

Mechanical design

The entire entangled photon source (Fig. 5.12) was fitted on a compact 30cm×45 cm aluminum breadboard with a 25-mm tapped hole grid. The beam height was set to 50mm, and the optical components were mounted on 25-mm-high pillar posts and secured with clamping forks. This way long-term stability could be ensured, while at the same time permitting the flexible fine-tuning required for alignment. All degrees of freedom required for efficient fiber coupling were accessible; the dichroic mirror and a custom-made fiber collimator were mounted on a kinematic mirror mount. The compact custom-made fiber collimator contains an aspheric lens with adjustable focus. The lens position was adjusted by rotating the aspheric lens in the aluminum housing, using a spanner wrench (Fig. 5.4).

Figure 5.11: Custom-made miniature mount for YVO_4 compensation crystal. Foto courtesy of Pavel Trojek, qutools GmbH.

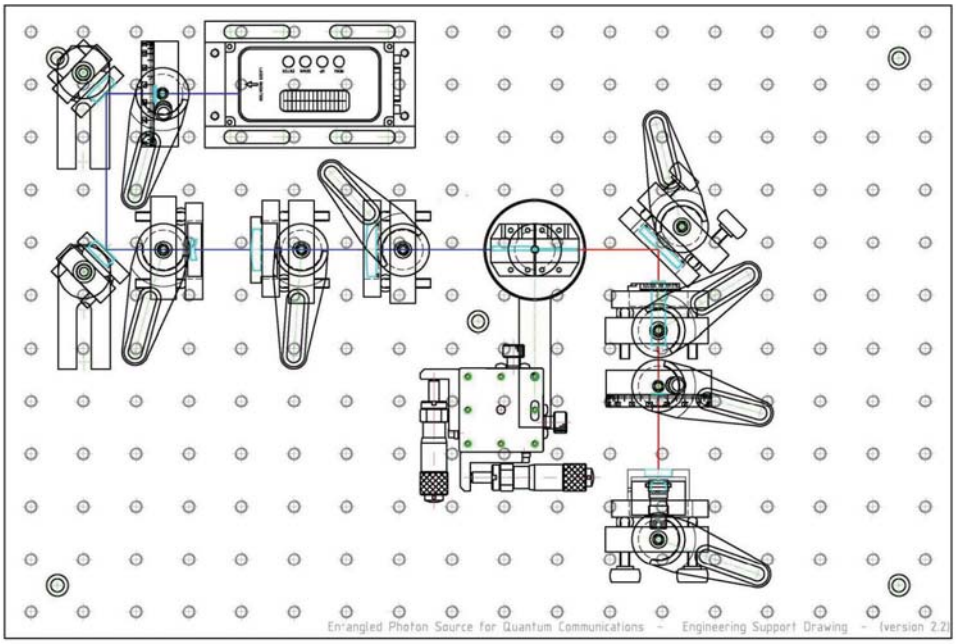

Figure 5.12: Mechanical design of the entangled photon source, accommodated on a compact breadboard. Design file courtesy of Pavel Trojek, qutools GmbH.

Wavelength division multiplexer

The signal and idler photons were both coupled into the same single-mode fiber, and then separated using and in-fiber wavelength division multiplexer (WDM). Compared to splitting the photons with a dichroic mirror prior to fiber coupling, the use of an in-fiber WDM significantly simplifies the alignment process, and leads to a more compact footprint. The WDM, acquired from FONT Canada, reaches its maximum isolation ($>$20 dB) between signal and idler channels at wavelengths of 765 nm and 850 nm, respectively. As pointed out in the previous paragraphs, the achievement of a high degree of polarization entanglement required an additional narrow-band interference filter. This filter had a center wavelength of 783nm and a bandpass of $\sim$ 3nm. For wavelengths of 783 nm and 839 nm, the isolation of the WDM was reduced to $\sim$ 10dB. This imperfect splitting ratio of the WDM leads mainly to a loss of coincidences and does not affect the entanglement visibility, since the IF filter prevents coincidences of photons that exit the wrong output port.

An interesting alternative would be a WDM using polarization-maintaining single-mode fibers. This option was not pursued as we could not find a provider for such a WDM for wavelengths around 810nm. Additionally, due to the different group velocities for fast and slow axes in PM fibers, such a device would introduce additional which-polarization timing information. However, this does not pose a fundamental limitation and could be compensated for, e.g. by splicing equal lengths of PM fiber with its fast and slow axis interchanged (i.e. rotated by 90°). In particular for wavelengths in the telecom window, where the range of high-quality fibered components is much more plentiful, such an option could indeed be highly practical.

Setup overview

The schematic setup of the source as built and tested is depicted in Fig. 5.13. The astigmatic output beam of the laser diode is attenuated using a neutral density filter, and focused to a circular beam waist of approximately 19μm at the center interface of the two 20-mm crossed ppKTP crystals using lenses L2-L4. The pump polarization is set to approximately 45°using a HWP, which was then fine-tuned to balance the coincidence counts for the two nonlinear crystals. The two crystals are mounted on a double-oven and maintained at temperatures of equal phase-matching conditions. The SPDC photons inherit a mode with a waist size of 24 μm and propagate collinearly with the pump laser. A dichroic mirror (DM) transmits 99% of the pump light and reflects the SPDC photons through the compensation crystal. An additional 200μm-thick YVO_4 plate is angle-tuned about its optical axis to set the relative phase of the polarization-entangled photons. The phase plate could alternatively be placed in the pump path (AR-coating is critical in both cases). A color-glass long-pass filter isolates the remainder of the pump photons and rejects stray light. The SPDC photons are coupled to single mode fiber, guiding the photons to a wavelength division multiplexer which splits the signal and idler

photons with non-degenerate wavelengths into two output fibers. The photons are then further filtered via an interference filter with a FWHM of 3.5 nm, placed in the collimated beam in the polarization analyzer module.

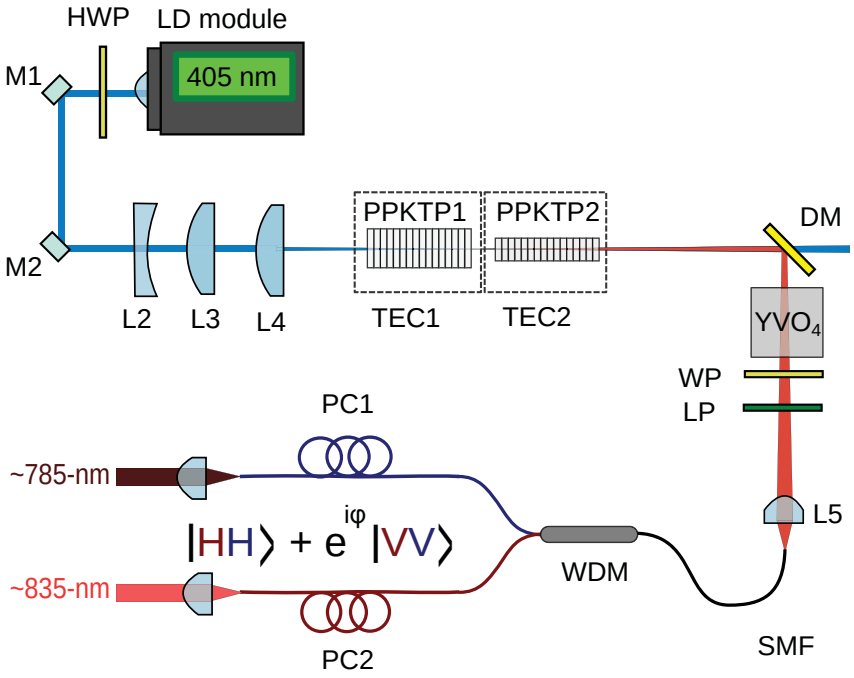

Figure 5.13: Schematic experimental setup. The pump LD is corrected for ellipticity and focused to the center interface of two thermally controlled (TEC1,TEC2) PPKTP crystals. The SPDC generated in the crystals is separated from the pump photons via a dichroic mirror (DM) and passes a YVO compensation crystal and phase plate, before being coupled into an SMF that guides the photons to the output ports of a WDM. The source, including driving electronics, are mounted on a compact 40×30 cm^2 breadboard. The WDM output fibers are connected to free-space polarization analyzers, consisting of a quarter wave plate (QWP) and a polarizer (POL), where further filtering occurs via an interference filter (IF) and long-pass filters (LP). The photons are then detected via multi-mode fiber (MMF) coupled silicon SPADs.

5.4 Performance Verification Setup

Optical setup

In order to assess the compliance of the EPS with the contractual performance requirements (Table 5.1), the two output fibers of the WDM were connected to two

single-channel polarization analyzers. Each fiber was coiled in a "bat-ear" polarization controller, in order to undo any change of the polarization state introduced by residual birefringence or twisting of the single-mode fibers. The signal and idler photons were outcoupled using a fiber collimator, connected to the respective output ports of the WDM. The polarization-correlations were assessed using a zero-order QWP (designed for 780nm and 850nm, respectively) and a thin-film polarizer (Codixx VIS/NIR) mounted in motorized rotation stages. For measurements at high pair rates, neutral density filters were added, in order to avoid saturating or damaging the single-photon detectors. After traversing the free-space polarization analyzer, the photons were detected via multi-mode fiber-coupled single-photon avalanche diodes (Perkin Elmer AQRH). The photon-pair-detection events were identified via a fast electronic AND gate (see next paragraph) and the detection-rates were transferred to the PC via USB. The motorized rotation mounts (M1-M4) were controlled via a LabView interface, where both correlation function and quantum state tomography were performed via automated measurement procedures (Fig. 5.14). A long-pass filter (LP) was inserted into the idler and signal paths to block stray light and an interference filter (IF) was added into the signal path to increase the correlation visibility.

Photon-pair detection

In the experimental test setup, two actively quenched single-photon avalanche diodes (Perkin Elmer AQRH) generate 35-ns TTL pulses upon detection of a signal or idler photon. The rising-edge of the TTL pulses is identified using either a fast field programmable gate array (FPGA) or a time-to-digital converter (TDC-qutools quTAU). Although both the FPGA and TDC have a temporal resolution of $<$ 100ps, the shot-to-shot timing jitter the TTL pulse generates in the Si-SPADs ($\sim 0.5ns$) limits the minimum coincidence window to $\sim$1-2ns.

5.5 Experimental Results

For all the experimental tests of the EPS, the VHG Ondax laser diode was run at full pump power ($\sim$37 mW). In order to avoid saturation of the detectors, this was attenuated by $\sim$30 dB for the low-power measurements. This attenuation was removed in steps of 10 dB for measurements at higher pump powers. For measurements at higher pump powers, attenuators were inserted symmetrically into the signal and idler paths of the polarization analyzer, since, due to the high number of pairs generated, saturation of the single- photon detectors ($\sim$ 2 Mcps saturation) would occur for pump powers above $\sim$100 μW.

5.5.1 Detected brightness at low pump power

With the polarizers removed from the polarization analyzer, but the spectral filters in place, we detect a total coincidence rate of R_c = 16 kcps and a signal singles rate

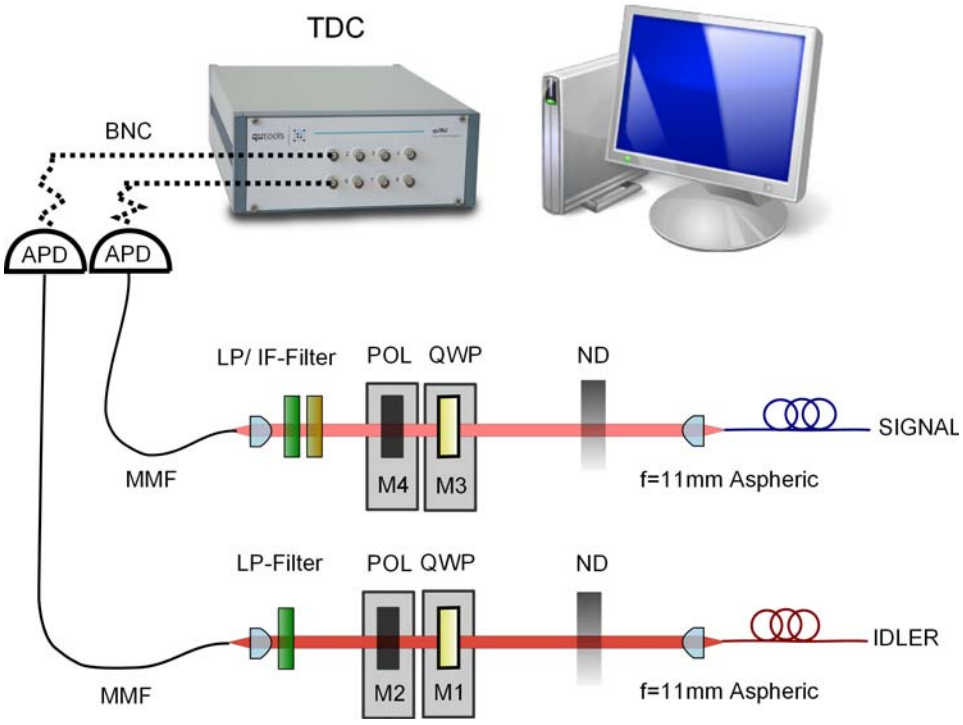

Figure 5.14: Schematic of EPS test-setup. Neutral density filters add loss, simulating real link situations. After polarization analysis via a QWP and thin-film polarizer (POL), the photons are coupled to multi-mode fibers and guided to the SPADs (APD). Coincidence measurements are performed via a fast electronic AND gate and transferred to the PC via USB. The motorized rotation mounts (M1-M4) were controlled via a LabView Interface.

of R_s =89 kcps at a pump power of 0.025 mW. Together with a measured FWHM of 2.3 nm, these values amount to a *detected* pair rate of 640 kcps/mW and a detected spectral brightness of 278 kcps/mW/nm at a conditional coincidence ratio $\frac{R_c}{R_s} \sim 0.18$ and $\frac{R_c}{R_i} \sim 0.10$. At the time of publication this was the highest reported normalized detected pair rate and spectral brightness for this type of system.

Notice that these pair rates were significantly lower than the ∼9 Mcps/mW obtained in a single-crystal configuration. Three main factors contributed to this lower efficiency: Firstly, the results in Chapter 4 were obtained for the most efficient region of the most efficient crystal; all other crystals were less efficient (at most 50% efficiency). Secondly, the spectral bandpass filter, required for high entanglement visibility, added approximately 50% loss. Finally, balancing the two SPDC processes required the pump to be focused at the center interface of the HH and VV pairs. The emitted SPDC mode of the HH and VV photon pairs are not centered at the position of the pump waist, but shifted toward the center of the respective crystals. This led to imperfect fiber coupling of the SPDC emitted from the both crystals, and thus lower pair rate and heralding efficiency.

5.5.2 Visibility and fidelity

The quality of the polarization entanglement was characterized by measurement of signal-idler coincidences $N(\theta_A, \theta_B)$ (Fig. 5.15) for various combinations of measurement angles of the linear polarizers (θ_A for the signal and θ_B for the idler photon). In the case of an ideal maximally entangled $|\Phi^+\rangle$ state and ideal polarizers, varying the angle θ_B leads to correlation functions (2.26) with perfect fringe visibility ($V = 1$) for all angles θ_A (and vice versa). In the presence of experimental imperfections, the experimental visibility can be extracted by a least-mean square fit to:

$$N(\theta_A, \theta_B) = \frac{N_0}{2}\left(1 - V\sin(\theta_B - \theta_A)\right) \tag{5.4}$$

where the fitting parameter V corresponds to the visibility and N_0 is a normalization factor. Fixing θ_B to $0^\circ, 90^\circ, 45^\circ$,and -45°, we obtained visibilities of $V_H = 99.5\%, V_V = 99.3\%, V_D = 97\%, V_A = 96.2\%$, where the pump power at the crystal input facet is 0.025 mW in all cases.

To more completely assess the degree of entanglement a quantum state tomography was performed, and the experimental density matrix was reconstructed using a linear state reconstruction technique. For low pump powers (0.025 mW) the reconstructed density matrix had a Bell-state fidelity of 0.983 ± 0.005. Accidental coincidences were negligible at such low pump powers. The main factors contributing to the imperfect visibility were remaining which-crystal information due to non-identical SPDC spectra of the two crystals (overlap integral ∼99%, see Fig. 5.6) and imperfect timing compensation, as well as a weak polarization dependence of the WDM splitting ratio ($\sim 10\%$ variation with input polarization).

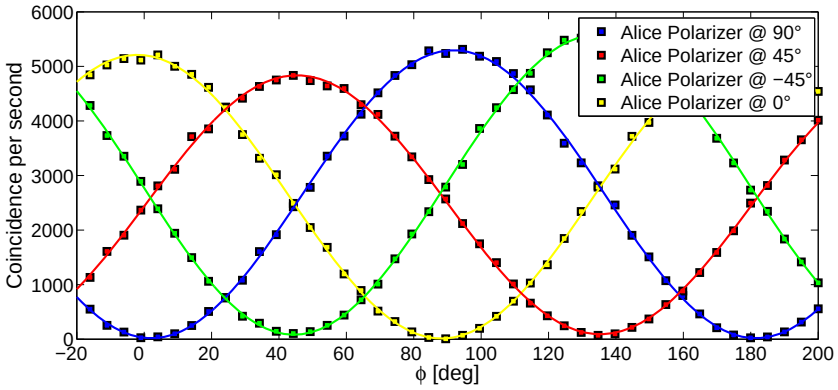

Figure 5.15: Correlation functions obtained for diagonal D/A (red/green) and H/V (yellow/blue) measurement basis. Pump power 0.025 mW. (Square experimental data-points, line: best fit). The visibilities calculated from the fits to raw data (no correction for accidental coincidence counts) were H/V 99.5%/99.3%, D/A 97.0%/96.2%

5.5.3 Multi-pair effects at high flux rates

Scaling from the detected brightness at low pump powers, we can infer that, at 40mW pump power, we could detect a coincidence rate larger than 20 Mcps. With the typical saturation rate of 10 Mcps for commercial silicon SPADs, the total singles count rates of $2 \times R^{(2)}/\eta \sim 200$ Mcps would already require an array of about 60 detectors in order to detect the large number of pair coincidences, while not exceeding ∼30% of each detectors' saturation level. In addition to this immense logistic requirement, there is a fundamental limitation, due to multi-pair emission in SPDC (section 2.5).

For the 2.4 ns coincidence window implemented in the analyzing detection electronics, the visibility dropped below 80% at a pump power of $\sim$ 2.2 mW ($\sim$ 50 Mpairs/second at the output of the crystals inferred from estimated losses). Hence, while higher pair rates are possible using higher pump powers, the accidental coincidences obtained with our detection electronics would reduce the entanglement visibility below the threshold required for many applications. Figure 5.16 depicts the decrease of fidelity for high pair rates obtained for high pump powers (theory calculated using open access Matlab toolbox for quantum photonics [244]).

Higher useful pair rates can only be achieved by using smaller coincidence windows, achievable with low-timing-jitter SPADs, such as those reported in Ref. [245]. However, even with a coincidence window of only 100 ps, the observed visibility would decrease to $\sim$ 80% when pumped at the full 40mW of the compact Ondax LD. This clearly demonstrates that significant advancements in terms of useful entangled photon pair rates generated via SPDC requires further improvements in the field of detector technology and timing electronics.

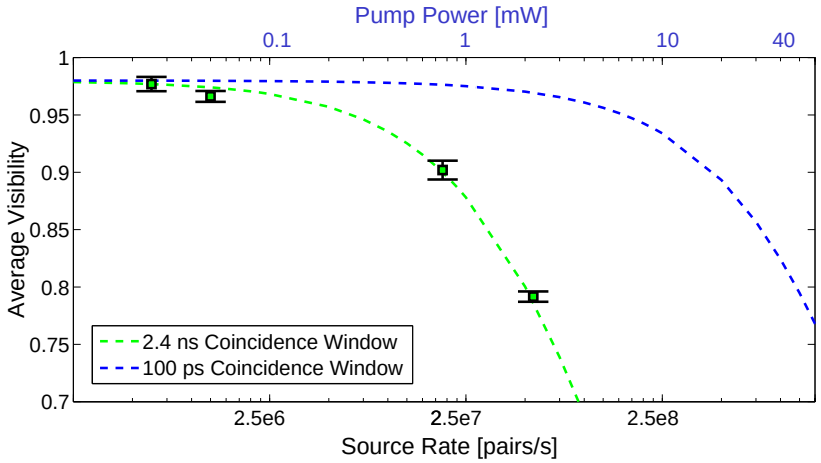

Figure 5.16: Polarization correlation visibility obtained from full tomographic density matrix reconstructions at 0.025 mW, 0.05 mW, 0.78 mW and 2.2 mW respectively. The measurements at 0.78 mW and 2.2 mW were conducted with attenuation added to both paths of the polarization analyzer (Fig. 5.13) to avoid SPAD saturation. The bottom scale denotes the estimated number of photon pairs at the crystal output. We evaluate the impact of multi-pair emissions via a Matlab simulation of the SPDC photon pair number, utilizing a quantum optics toolbox. The green line indicates the modeled behavior for pair generation rates scaled to higher pump powers. The visibility of the emitted state was set to 98% to account for other experimental imperfections, as outlined in the previous section. Even for a coincidence window of 100 ps (dotted blue line), the simulation shows that a visibility above 90 % is no longer maintainable for pump powers above 20 mW.

5.6 Conclusions

A compact and robust source of polarization-entangled photons was assembled and characterized. The source is based on a collinear crossed-crystal scheme, with non-degenerate signal and idler photons generated in two crossed 20-mm ppKTP crystals. A detected pair rate of 640 kcp/mW, a spectral brightness of 278 kcp/mW/nm and a Bell state fidelity of 98% were achieved (see comparative table in Appendix A), which lead to the sucessful closing of the ESA EQU0 project. The compact footprint of the source, in combination with the ruggedness of the configuration, make the EQU0 source an ideal device for future field experiments on quantum communications and fundamental tests of quantum entanglement, and well-suited for mobile and space applications.

A critical point was balancing the efficiency and spectral properties of the two nonlinear crystals; due to technical issues in the crystal poling procedure, differences in the spectral SPDC characteristics in all ppKTP samples tested were observed. This added complexity to the experimental setup and made individual temperature control of the two nonlinear crystals (double-oven), and spectral filtering necessary, in order to achieve high entanglement visibility. Furthermore, balancing the pair rate produced from the two crystals resulted in an overall reduction in terms of pair rate and heralding efficiency. These issues were addressed in a further iteration of the EPS (see next chapter).

Chapter 6

Ultra-bright Folded Sandwich Entangled Photon Source

In this chapter, I report on an evolution of the EQUO entangled photon source, which combines features of the Sagnac loop and crossed-crystal (or "sandwich") configurations. The novel "folded sandwich" geometry uses a single nonlinear crystal combined with a wave plate in a linear double-pump-pass interferometric arrangement. Due to a common-path configuration of down-converted and pump photons, there is no requirement for active path-length stabilization of the interferometer. At the same time, the double pass recycles the first-pass pump power, and allows locating the pump focus for both passes at the center of the nonlinear crystal, thus promising higher efficiency. The implementation of the folded sandwich source, with a number of additional technical improvements with respect to the EQU0 source, led to unprecedented normalized pair-detection rates, a higher heralding efficiency, and a higher degree of polarization entanglement with improved long-term phase stability.

This chapter is based on material published in Publication **B**.

6.1 Folded sandwich configuration

In the folded sandwich configuration (Fig. 6.1), a pair of co-polarized photons is generated via SPDC in a type-0[1] non-degenerate collinear phase-matching configuration in, for example, ppKTP. Polarization entanglement at the non-degenerate wavelengths can be achieved by bi-directional pumping of the nonlinear crystal in a linear interferometric arrangement [246–248]. The photons emitted in the first pass (in state $|V_{\lambda_s} V_{\lambda_i}\rangle$) are reflected back into the nonlinear crystal via a mirror and appropriately designed focusing optics. A specifically tailored wave plate (WP) placed between crystal and mirror introduces a quarter-wave retardation for the SPDC photons, and a half-wave or full-wave retardation for the pump pho-

[1] The scheme can also be implemented using non-degenerate type-I and type-II configurations.

tons. The wave plate is oriented at 45°, such that the double-pass transforms the first-pass SPDC photons to $|H_{\lambda_s} H_{\lambda_i}\rangle$, while leaving the pump polarization unaffected. The SPDC generated in the second pass of the pump through the nonlinear crystal is emitted in the state $|V_{\lambda_s} V_{\lambda_i}\rangle$, and a polarization-entangled state ($|\Psi(\phi)\rangle \propto |V_{\lambda_s} V_{\lambda_i}\rangle + e^{i\phi(\lambda_s,\lambda_i)}|H_{\lambda_s} H_{\lambda_i}\rangle$) results if a fixed relative phase relationship $\phi(\lambda_s, \lambda_i)$ is maintained over the detected SPDC bandwidth. After passing through the nonlinear crystal for the second time, the SPDC photons are then extracted from the linear interferometer via a dichroic mirror (DM1). The nondegenerate signal and idler photons can then be transformed into two distinct spatial modes using either a dichroic mirror (DM2) or fiber-based wavelength-division multiplexer.

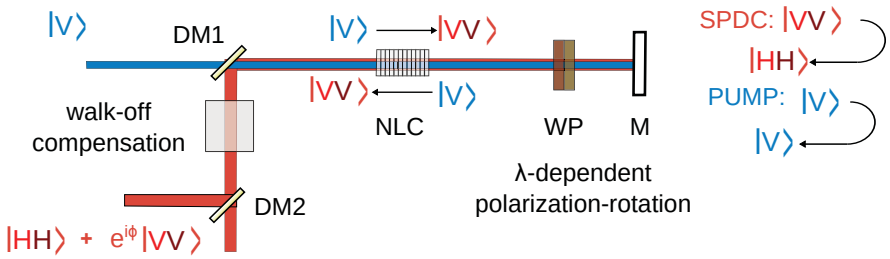

Figure 6.1: The principle of operation can be understood as a sandwich configuration, in which - instead of using a second orthogonally oriented crystal - the SPDC from a single nonlinear crystal (NLC) is transformed to the orthogonal polarization (i.e. “folded sandwich”).

Any spatial which-crystal information the photons may carry after SPDC emission is effectively erased via the projection into the single spatial mode of a coupling fiber (not depicted in Fig. 6.1). Since the same crystal is used to generate both horizontally and vertically polarized pairs, there is no distinguishing which-polarization information due to distinct spectral intensity profiles [236]. However, distinguishing information remains in the spectral phase. In the folded sandwich configuration, this which-polarization information can be compensated for analogously to the manner described for the sandwich scheme. The only minor difference is the additional phase shift due to the chromatic dispersion in the waveplate ($2 \times \phi_{wp}(\lambda_s, \lambda_i)$).

Phase stability in common-path configuration

The main advantage of so-called common-path configurations, such as the folded sandwich configuration, is that there is no requirement for active path-length stabilization. To see why this is the case, we consider a small change of the length (δL) of the linear interferometer formed between the exit facet of the nonlinear crystal and the mirror M. The additional phase acquired by the SPDC photons generated

in the first pass due to the change in propagation distance is:

$$\phi_{SPDC} = 2(n_s\omega_s + n_i\omega_i)\delta L \tag{6.1}$$

On the other hand, the pump photons that drive the second-pass emission, which propagate along the same optical path as the first-pass SPDC, acquire an additional phase:

$$\phi_{pump} = 2(n_p\omega_p)\delta L \tag{6.2}$$

In the absence of dispersion (i.e. $n_p = n_s = n_i$) the additional phases are equal

$$\phi_{pump} = \phi_{SPDC} \tag{6.3}$$

due to energy conservation. Since the total phase of the signal and idler photons generated in the second pass is inherited from the pump photons [174], path-length fluctuations in the linear interferometer do not result in a change of the relative phase of the entangled state. The same auto-compensation of path-length fluctuations is observed in the Sagnac-loop and sandwich configurations.

6.2 Technical Realization

In terms of the technical realization, the folded sandwich EPS uses many of the components already discussed in the previous chapter. For components which were already part of the EQU0 source, I will only discuss the relevant modifications, or omit them if there were none.

Pump and collection optics

In order to ensure optimal initial beam quality and more flexibility in choosing the pump beam parameters, laser emission (cwl $\sim$ 405.4nm) of the Ondax volume holographic grating stabilized laser diode was coupled into 405-nm single-mode fiber. The fiber-coupling assembly was mounted on a miniature breadboard in order to facilitate interchanging between experimental setups, and a fiber-coupling efficiency of 65$\%$ was achieved, without correcting the elliptical beam profile of the Ondax LD module. The output power of the Ondax module was ~ 40 mW prior to fiber-coupling, corresponding to a maximal fiber-coupled power of ~ 26mW in the source. Note that power handling at the input surface of the SMF is critical for 405-nm light, and the pump power was kept well below the maximum value. Note, however, that high-power single-mode fibers are available in the 405-nm region (e.g. SUK Hamburg). The fiber-coupled pump beam was then collimated via an aspherical lens ($f = 4.5mm$), and focused to a waist size of $w_p \sim 69\mu m$ at the center of the nonlinear crystal, using an $f = 200mm$ lens. This beam waist was chosen as a trade-off between pair rate, heralding efficiency, and alignment

tolerances. After traversing the nonlinear crystal, the pump laser was relayed to the center of the crystal at unit magnification, using a spherical mirror. The SPDC photons were collected using either single-lens or dual-lens imaging systems. The more convenient of the two turned out to be the two-lens imaging system, consisting of a collimation lens and a fiber coupler. This reduces beam aberrations of the collected mode, and simplifies the placement of the compensation crystal since it is located in the collimated beam [2].

Temperature-stabilized compensation crystal

The double-pass configuration was implemented using both a 20-mm and a 11.48-mm ppKTP sample, which required 31-mm, and 18.5-mm YVO_4 compensation crystals, respectively. The long-term stability of the phase of the entangled state was improved with respect to the EQU0 EPS, by placing the compensation crystals in a temperature-controlled oven. The thermal path-length dependence of extra-ordinary and ordinary polarized photons in 18.5-mm of YVO_4 led to a phase shift of π for a temperature change of $\sim 2.4^{\circ}$C (calculated using the temperature-dependent birefringence of YVO_4 reported in [249]), which was in good agreement with the experimental data (Fig. 6.2). This means that in order to maintain a fidelity above 99.5 % requires stabilization to $\pm$ 0.1°C. Similarly, temperature-dependent path-lengths in KTP [210] result in a required stability of the down-conversion crystal of $\pm$ 0.05°C.

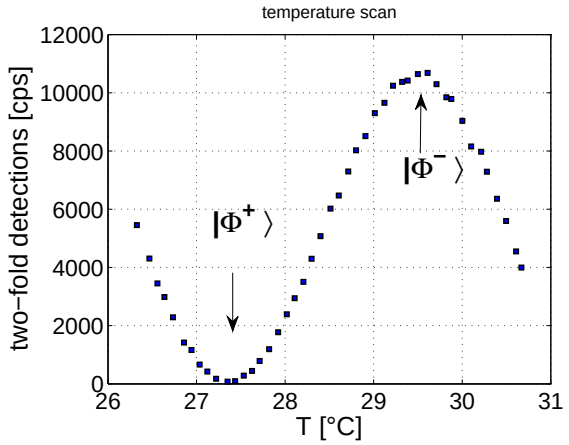

Figure 6.2: Coincidence counts for crossed linear polarizers in signal and idler arms (θ_A=45°, $\theta_B = -45^{\circ}$) as the relative phase ϕ is modified by temperature-tuning YVO_4 compensation crystal.

[2] In a single-lens collection system the compensation crystal introduces a longitudinal shift of the beam waist position, and thus requires re-alignment.

Special wave plate

In the ideal case, the double-pass scheme calls for a device that introduces a $\frac{\lambda}{2}$ retardation for the SPDC, but a λ retardation at the pump wavelength λ_p. The performance at the SPDC wavelengths is more critical, as it affects the achievable entanglement visibility; if the photons are not flipped by 90°, they are no longer polarized along one of the nonlinear crystal's crystallographic axes, which would lead to chromatic de-polarization effects for typical SPDC bandwidths. For a cw pump, no dispersive de-polarization is to be expected after the passage through the nonlinear crystal. Thus, any deviation from the optimal behaviour at 405nm is merely reflected in the efficiency of the second pass, but not the entanglement visibility.

Achromatic QWP: The polarization rotation of the $|V_{\lambda_s} V_{\lambda_i}\rangle$ photons to $|H_{\lambda_s} H_{\lambda_i}\rangle$ was implemented via the double pass through a standard achromatic quarter-wave plate (AC-QWP), oriented at 45° with respect to the ppKTP's z-axis. Figure 6.3 depicts the calculated retardation over the SPDC wavelength range for an AC-QWP consisting of 726 μm quartz and 571 μm MgF_2. The standard AC-QWP for this wavelength range is anti-reflection coated at 750 nm - 850 nm. In order to avoid power fluctuations due to interference, the wave plate was additionally AR-coated at 405nm. For normal incidence the AC-QWP purchased introduced a retardation of $\frac{0.93\lambda}{4}$ (tested at 850 nm and 785 nm using a polarimeter), slightly different from the required $\frac{\lambda}{4}$ retardation. This could, however, be mitigated by a 3°tilt about the wave plate's optical axis. At this angle, the imperfect wave plate indeed introduced the required retardation.

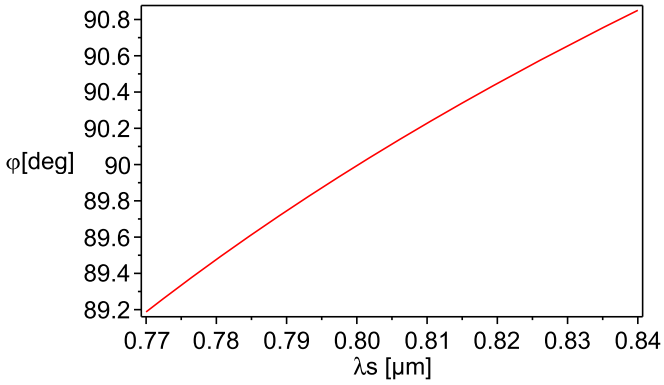

Figure 6.3: Retardation angle over SPDC wavelength range of interest, for the zero-order achromatic QWP consisting of 726 μm quartz and 571 μm MgF_2 cemented with orthogonally oriented optical axis, as built by Altechna. At 405-nm, the device acts as a $\lambda/7$ WP.

Maximizing vertical pump component in both passes: At 405nm, the AC-QWP acts as a $\sim \frac{\lambda}{7}$-wave plate, as opposed to a full-wave plate required to use the full pump power to drive SPDC in both first and second pass. Hence, the vertical

pump polarization is transformed to an elliptical polarization after the double-pass through the wave plate. Since only the vertically polarized pump component is phase matched for SPDC, the efficiency of the second pass is reduced. Any improvement of the wave plate's performance at 405nm would come at the cost of decreased performance as a QWP in the NIR. However, by appropriate choice of the parameters α and ϕ of the pump polarization $|\phi_p\rangle = \alpha|V\rangle + \sqrt{1-\alpha^2}e^{i\phi}|H\rangle$, it is possible to pre-compensate for the polarization transformation introduced in the double pass through the AC-QWP, and thus maximize the component polarizer vertically for the second pass. A combination of HWP and birefringent plate rotatable about its optical axis (variable-phase plate - vWP) allows both of these parameters independently.

Figure 6.4 depicts the power of the vertical pump component for first- and second pass through the ppKTP crystal, as a function of phase (ϕ) and amplitude (α). Evidently, the power of the vertical polarization in the first pass (purple surface plot in Fig. 6.4) is not affected by the relative phase. However, the vertically polarized pump power driving SPDC in the second-pass (rainbow-colored surface plot in Fig. 6.4) depends on both α and ϕ, due to the double pass through the $\frac{\lambda}{7}$ wave plate oriented at 45°. For the optimal input polarization it is possible to utilize $\sim$ 80% of the pump power to drive SPDC in both passes. Note that using this strategy, even in the worst-case scenario, in which the AC-QWP acts as a QWP at λ_p, half of the pump power can be used to pump both the first- and second-pass. Figure 6.5 depicts the transformations introduced by various birefringent elements in the optical setup, which determine the vertically polarized pump component that drives the second-pass SPDC emmission, and contribute to the overall phase of the entangled state[3].

Dichroic mirror

As an alternative to the fiber-based WDM, a dichroic mirror was used for splitting the signal and idler photons into two separate spatial modes. Note that if this is done before coupling to a single-mode fiber, the filters must have imaging surface quality. Also note that these filters might introduce a wavelength-dependent phase shift, when used too close to the transition-edge. The dichroic mirror (Chroma z785 RDC) has imaging quality and a specified reflectance of $> 95\%$ at 785 nm, and a transmittance of $\sim 90\%$ 805 - 1100 nm, for an angle of incidence of 45°. The transition-edge of the filter could be shifted from 805nm by tuning the angle of incidence, and the best performance for signal and idler photons generated symmetrically around 810nm was obtained for an angle of 42°-43°. For phase-matched center wavelengths of 790 nm and 831 nm, the filter exhibits an isolation of > 16 dB, corresponding to about 2.5% of light coupling into the wrong output port.

[3]This mitigation strategy requires the pump-beam to maintain a well-defined polarization state after the propagation through the birefringent nonlinear crystal, which acts as a (very) high-order wave plate. The vertically and horizontally polarized pump components thus travel at different group velocities through the nonlinear crystal, and would be subject to polarization mode dispersion for

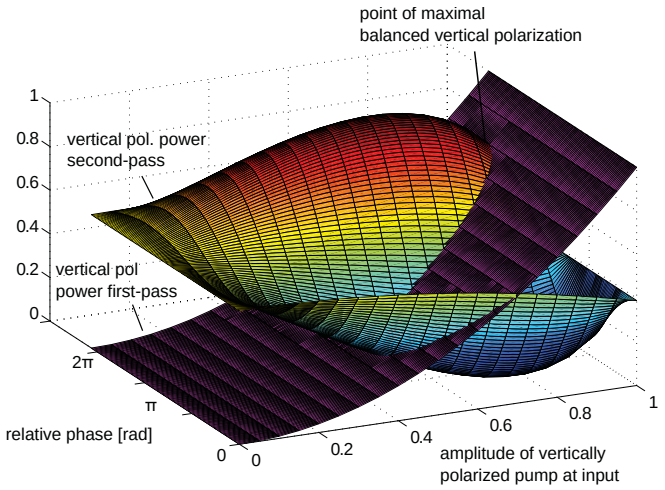

Figure 6.4: Phase-matched (vertically polarized) pump power in first- and second-pass through the ppKTP crystal, as a function of α and the relative phase ϕ of the initial polarization state $|\phi_p\rangle = \alpha|V\rangle + \sqrt{1-\alpha^2}e^{i\phi}|H\rangle$ of the pump photons. At the optimal working point, 80% of the pump power can be used to drive both first- and second-pass SPDC emission with equal power.

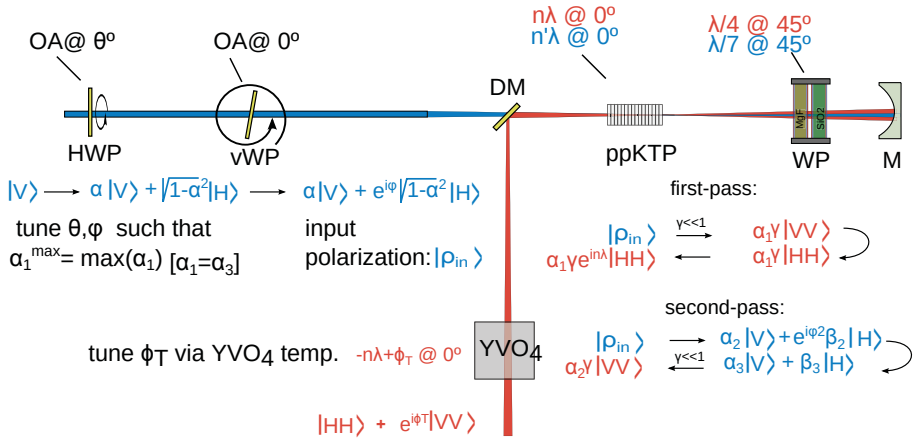

Figure 6.5: Polarization transformations introduced by various elements in the folded sandwich configuration. Due to the additional polarization-transformation of the pump photons, introduced by the AC-QWP, it is important to know the polarization state at each stage in order to achieve high efficiency in the double-pass EPS.

Experimental setup

The double-pass scheme was implemented with 20-mm and an 11.48-mm type-0 ppKTP crystals, in the experimental setup depicted in Fig. 6.6. The nonlinear crystal was mounted on an oven (TEC1), consisting of a Peltier element, a 10kΩ Thermistor, and a commercial temperature controller, with a specified long-term temperature stability of $\pm 0.002^{\circ}$C (Wavelength Electronics PTC2.5K-CH). The temperature was set to phase match a collinear non-degenerate type-0 SPDC process, from 405.4 nm (pump) to $\sim$784 nm (signal) and $\sim$839 nm (idler). The output beam of a fiber-coupled volume holographic stabilized continuous wave laser diode (LD) (Ondax Inc.), with a cwl of 405.4 nm, was attenuated and focused to the center of the nonlinear crystal. The SPDC photons generated in the first pass propagated together with the pump through the AC-QWP, and were directed back to the crystal via a broadband reflection coated spherical mirror (M). The SPDC generated in both passes was spatially overlapped, locating the center of curvature of the spherical mirror at the crystal center, and extracted from the interferometer via a highly reflective ($R >$99% 750nm-850nm) dichroic mirror (DM1) that transmitted the pump photons[4]. Dispersive de-phasing effects due to the double pass were reversed via the YVO_4 compensation crystal, which was mounted on a custom designed oven (TEC2 - with same specifications as TEC1). The phase of the entangled state is set by temperature-tuning the compensation crystal (Fig. 6.2), which is particularly practical for automated procedures, but requires rather long settling times. Therefore, the phase of the entangled state could alternatively be hand-tuned using a phase plate placed in the SPDC path. Note that, since the phase plate in the pump beam would also affect the second-pass pump power (see section above), the phase plate must be located in the SPDC path, in order to decouple the balancing of first-pass and second-pass SPDC emission from the relative phase of the entangled state.

A color-glass long-pass filter (LPF) blocked remaining pump photons and stray light, before the photons were coupled into a single-mode fiber. The fiber-matched mode had a Gaussian beam waist of $\sim 45\mu m$ at the crystal center. The signal and idler photons were separated via a dichroic mirror, which was located in the polarization analyzer (Fig. 6.7)

6.3 Experimental Performance

The polarization correlations were assessed by measurement of signal-idler coincidences detected after two polarization analyzers, consisting of a quarter-wave plate (QWP) and a thin-film polarizer, each mounted on a motorized rotation mount. After traversing the analyzer modules, the signal and idler were coupled into multimode fibers and guided to two single-photon avalanche diodes (SPAD) with a de-

[4]The pump field propagates back into the input mode when the source is optimally aligned. For operation at high pump powers an optical isolator is necessary, in order to avoid destabilizing, potentially damaging feedback into the laser source.

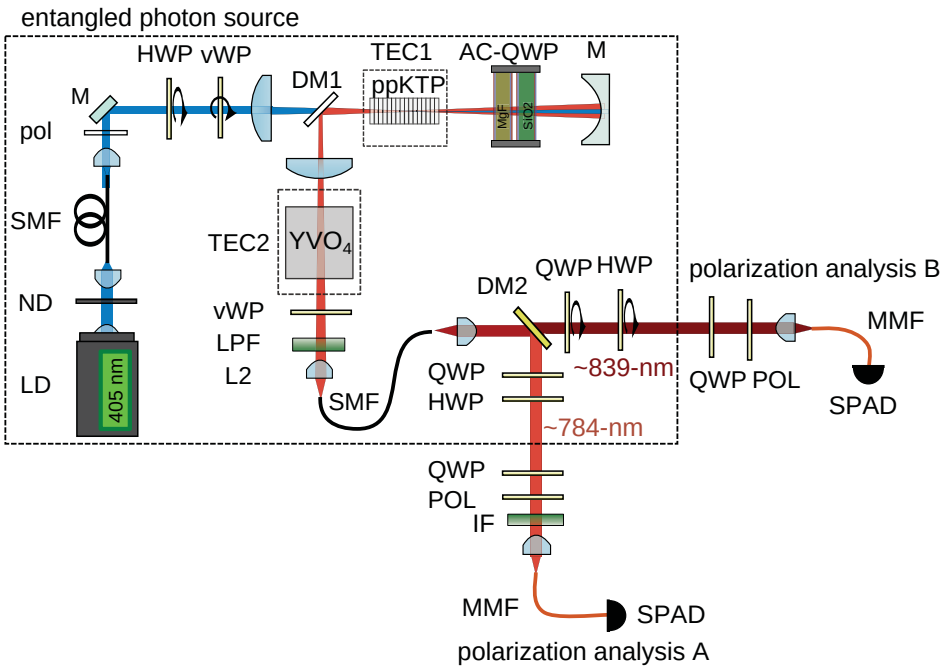

Figure 6.6: Experimental realization of the "folded sandwich" source of polarization-entangled photons. For details refer to main text.

tection efficiency of ∼50% (∼300 cps dark counts), where coincident measurement events were recorded via a fast FPGA-based coincidence counting logic with its coincidence window set to 3.2 ns. The normalized pair-detection rate and entanglement were first assessed at low pump powers, at which accidental coincidences and SPAD saturation effects were negligible.

Results with 11.48-mm ppKTP

With the 11.48-mm ppKTP crystal we detected a peak total coincidence rate (polarizers removed) of R_c = 11.8 kcps and singles rates of R_s =61 kcps, and R_i =88 kcps, at a pump power of 10.4 μW incident on the crystal. This corresponds to a detected pair rate of 1.1 Mcps/mW, a detected spectral brightness of 0.39 Mcps/mW/nm (signal FWHM after IF ∼2.9 nm), and an experimental heralding efficiency of $\eta_s \sim 0.19$ and $\eta_i \sim 0.13$ for the signal and idler, respectively.

The visibilities (V) of the observed correlation functions were obtained as the best-fit parameter to the theoretically expected two-photon detection probability (Eq. 5.4). The polarization correlations observed for the 11.48-mm ppKTP crystal are depicted in Fig. 6.9. Fixing θ_B to $0°, 90°, 45°$,and $-45°$, resulted in best-fit visibilities of $V_H^{FIT} = 98.8\%, V_V^{FIT} = 99.1\%, V_D^{FIT} = 98.7\%, V_A^{FIT} = 98.8\%$, where the pump power at the crystal input facet was 0.028 mW in all cases. The fidelity with the ideal Bell state was evaluated using Eq. 2.38. At a pump power of 0.01 mW we obtain $V_{H/V} = 99.4 \pm 0.1\%$, $V_{D/A} = 98.8 \pm 0.2$ %, $V_{L/R} =$

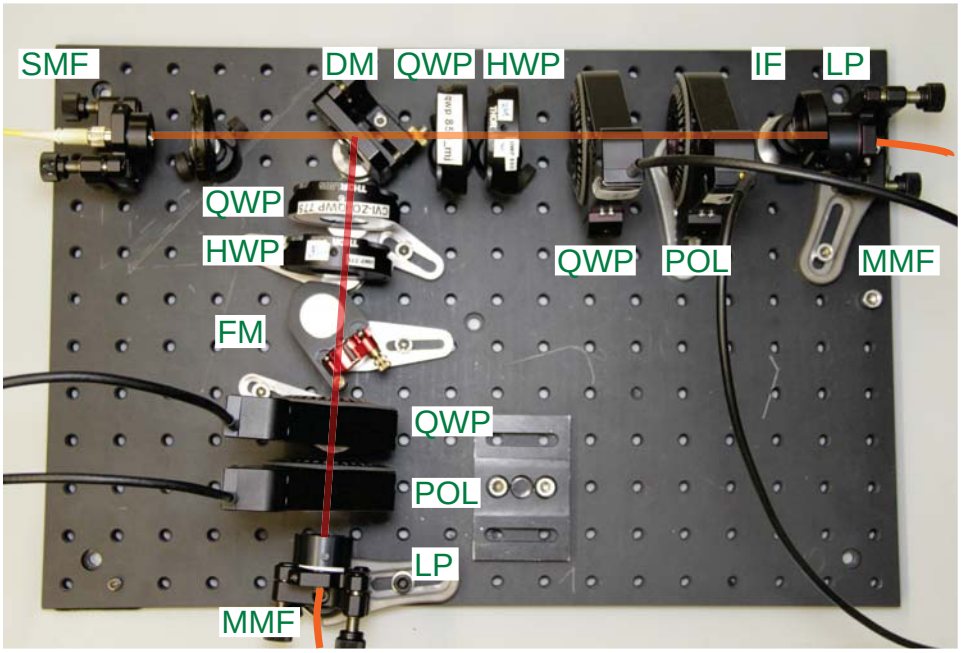

Figure 6.7: Wavelength splitting and polarization analysis mounted on a portable breadboard. The signal and idler photons exit the single-mode fiber (SMF) and are collimated using a custom collimation package. The dichroic mirror (DM) reflects the signal photon and transmits the idler photon. A quarter-wave plate (QWP) and half-wave plate (HWP) undo the polarization transformation introduced by the single-mode coupling fiber. A flip-mirror is inserted, in order to redirect the signal photons to another experiment. The first set of wave plates are to be considered part of the EPS, as the relative phase of the entangled state is set at this point. The polarization correlations are then assessed using a quarter-wave plate (QWP) and a thin-film polarizer (POL) mounted in a commercial motorized rotation mount. Ambient background light is blocked using a long-pass filter (LP) mounted on the output multi-mode-fiber (MMF) coupling assembly. Additionally, interference filters (IF) are placed in either the signal or the idler paths.

$98.7 \pm 0.2\%$, corresponding to a fidelity F$= 99.2 \pm 0.3\%$.

At higher pump powers, the limitations of the detection system employed led to a decrease in fidelity and normalized pair-detection rate (see prev. chapters). For low detector count-rates, the scaling of experimental pair rates is linear with the pump power. At higher pair rates, the lower detection efficiency due to saturation effects leads to a decrease in two-fold rates. Figure 6.8 depicts the resulting deviation of observed two-fold rates from model calculations with ideal, saturation-free detectors. Additionally, the limited timing resolution of the detection system (3.2ns) leads to an increased number of accidental coincidences, which result in a lower raw fidelity for high pump powers. Note that these effects are limitations of the detection system employed and could be mitigated utilizing faster detectors; with an array of detectors with a timing resolution $\sim$500 ps [245], we could have directly measured the full 1.1Mcps at a fidelity above 97%.

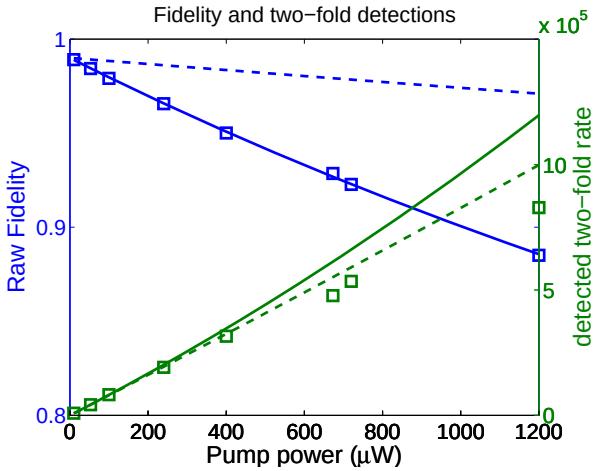

Figure 6.8: Total rate of coincidences and raw state-fidelity, as a function of pump power. All experimental data (squares) was acquired with polarizers in place ($T \sim$0.9). The two-fold-rate was obtained by summing the coincidence-detections C_{ij} over all polarizer positions in the H/V basis ($\sum_{ij=H/V} C_{ij}$). The simulations were conducted for a coincidence window of 3.2ns (solid lines), as used in the experimental setup, as well as 500ps (dashed lines). The scaling of experimental pair rates to higher pump powers is linear for low pair rates. At higher pair rates, detector saturation effects lead to a deviation from the modeled behavior and the observable fidelity drops, due to accidental coincidences.

Results with 20-mm ppKTP[5]

With the polarizers removed we detected a normalized pair rate of 3 Mcps/mW and a spectral brightness of 1 Mcps/mW/nm [250]. Note that for the 20-mm crystal, the spectral bandwidth was not directly measured, and the spectral brightness was

[5]The values reported in this subsection were obtained in collaboration with Carlos Abellan, as part of his MSc. Thesis [250].

Table 6.1: Performance characteristics of folded sandwich EPS with 20-mm and 11.48-mm ppKTP crystals.

crystal	$\Delta\lambda_s$	Mpairs/mW	Mpairs/mW/nm	Fidelity
11.48mm	$\sim$2.9nm	$\sim$1.1	$\sim$0.39	99.2 %
20mm	$\sim$3nm	$\sim$3	$\sim$1	98.3 %

normalized with respect to the FWHM passband of IF ($\sim$3 nm). The true spectral brightness normalized with respect to the spectral bandwidth of the SPDC photons was thus higher, but was not measured, as there was no single-photon spectrometer available at the time.

The best-fit visibilities (V) of the observed correlations were $V_H^{FIT} = 0.987 \pm 0.0011$, $V_D^{FIT} = 0.984 \pm 0.0014$, $V_V^{FIT} = 0.988 \pm 0.0012$ and $V_A^{FIT} = 0.979 \pm 0.0014$ (pump power 0.02 mW). Additionally, a full tomographic reconstruction of the experimental density matrix was performed using a maximum likelihood procedure [250]. For low pump powers the reconstructed density matrix had an overlap fidelity of $F = 0.983 \pm 0.004$ with the ideal Bell state. The fact that the fidelity is somewhat lower than that obtained with the 11.45-mm sample was most likely the result of imperfect compensation of temporal walk-off with the longer crystal. The main experimental results obtained with the 11.48-mm and 20-mm type-0 ppKTP samples are summarized in Tab. 6.1.

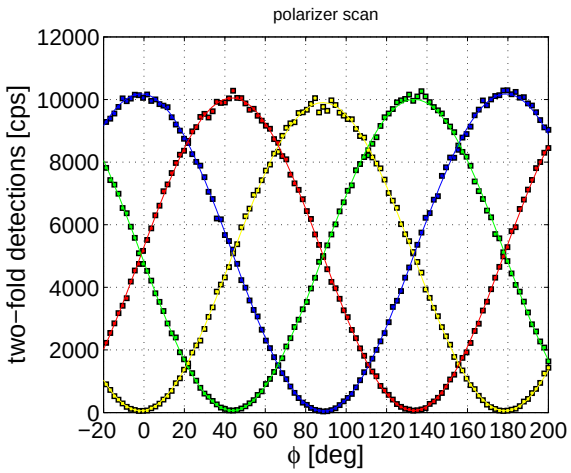

Figure 6.9: Two-photon polarization correlations for folded sandwich EPS with 11.48-mm ppKTP. Coincidence counts per second, as a function of polarizer orientation θ_A in the signal arm, for θ_B=0°(blue), 90°(yellow), 45°(red), and $-45°$(green). Square: experimental data, line: best fit. The fringe visibilities (V) were obtained as the best-fit parameter to the theoretically expected two-photon detection probability (see Chapter 5, Eq. 5.4). For θ_B = $0°, 90°, 45°$,and $-45°$, we obtained visibilities of $V_H^{FIT} = 98.8\%, V_V^{FIT} = 99.1\%, V_D^{FIT} = 98.7\%, V_A^{FIT} = 98.8\%$, where the pump power at the crystal input facet was 0.028 mW in all cases.

Limited visibility without IF

Without the IF-filter (placed in the signal arm of the polarization analyzer), the visibility observed with the 11.48-mm ppKTP crystal decreased to 84% in the D/A-basis (H/V 99.3%). The intensity spectra of the two passes were effectively identical (see Fig. 6.10); which-crystal information was contained in the phases, and was most likely the result of imperfect timing compensation.

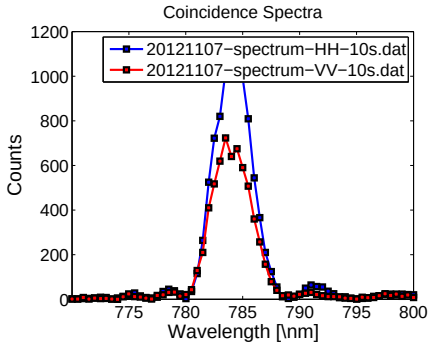

Figure 6.10: SPDC spectra of horizontally and vertically polarized signal photons before filtering with a 3.5 nm FWHM IF filter. The spectral shape observed for horizontal and vertical photons were almost identical (up to a scale factor); the normalized spectral overlap was $>$99% for both the unfiltered and filtered SPDC profiles.

Verification of the phase stability

The phase stability of the configuration was experimentally verified for the 11.48-mm crystal via measurements of the fidelity over time. The source showed good temporal stability, making long-term operation viable with periodic calibration on a time-scale of hours (see Fig. 6.11). The stability could be even further improved by correcting for drifts of the pump cwl [89, 251], via a pre-compensation crystal placed in the pump path. In order to assess the mechanical stability requirements for the length of the double-pass cavity, we performed fidelity measurements for varied positions of the retro-reflecting mirror (M). The result (Fig. 6.12) shows that the phase remains constant for small displacements ($<100\mu$m). For larger displacements of the mirror, a phase shift resulting from dispersion in air and geometric effects of the interacting Gaussian beams [252], as well as increasingly unbalanced fiber-coupling efficiency of first- and second-pass pair-emissions, lead to a decrease in fidelity with the initial state.

6.4 Conclusions

In this chapter, I have presented a novel source of polarization-entangled photons. The “folded sandwich” scheme is an evolution of the well-known sandwich scheme, which was used for the EQU0 EPS. The implementation of the folded

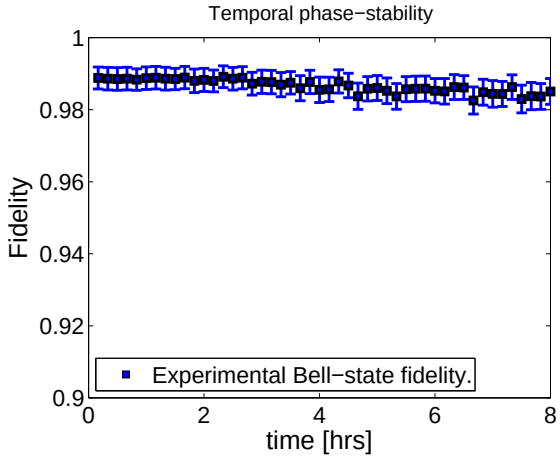

Figure 6.11: Bell-state fidelity over time under laboratory conditions with 11.48-mm pp-KTP. The long-term stability is limited by a drift of the center wavelength of the pump laser.

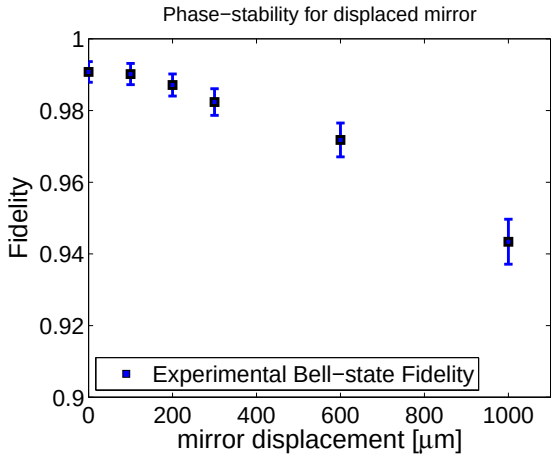

Figure 6.12: Bell-state fidelity observed with 11.48-mm ppKTP crystal as the cavity length is increased, via displacement of mirror M. The relative phase of the entangled state remains constant for large displacements of the cavity mirror. The decrease in fidelity is due to the imbalanced first-pass and second-pass photon generation probability, as the beam waist of the reflected pump and SPDC is displaced from the crystal center.

sandwich source with a number of additional technical improvements, such as temperature stabilization of the compensation crystal, resulted in better entanglement visibility and better long-term stability. Furthermore, the possibility of locating the beam waist of pump- and collection-modes at the center of the nonlinear crystal, and the double usage of the pump power resulted in unprecedented normalized pair-detection rates (see Tab. 6.1 and comparative table in Appendix A.).

Chapter 7

High-Heralding-Efficiency Sagnac Source of Entangled Photons

Ultra-bright sources of entangled photon pairs with high heralding efficiency are an important step in the pursuit of high-bit-rate entanglement-based quantum key distribution, as well as an enabling tool for loss-sensitive quantum optics experiments. In this chapter, I present a robust single-mode fiber coupled source of polarization-entangled photons that exhibits both high brightness and heralding efficiency. The source is based on SPDC from a 20-mm-long ppKTP crystal, bi-directionally pumped by a 405-nm laser diode in a Sagnac interferometer [174, 248]. The source can be operated in both degenerate type-II (signal and idler at $\sim$ 810 nm), and non-degenerate type-0 (signal at $\sim$784nm, idler at $\sim$839nm) quasi-phase-matching configurations, and a high degree of polarization entanglement was achieved for both phase-matching configurations. In contrast to the previously demonstrated sources, the focus parameters of this source were optimized with respect to heralding efficiency, leading to non-maximal source brightness.

7.1 High-heralding-efficiency Sagnac source

The sources demonstrated in the previous chapters exhibit normalized pair rates up to several Mcps per mW of pump power. Even for moderate pump powers, the pair rates generated call for detectors that meet highly demanding specifications. The un-attenuated detection would require an array of single-photon detectors with low timing jitter, in order to limit the effect of accidental coincidences (see Chapter 5).

A strategy that allows for the highest useful pair rates in light of such limitations is the improvement of the source's heralding efficiency (i.e. increasing the number of detected pairs for a given singles rate).

In an ideal source and detection system, the detection of the idler (signal) photon should herald the presence of its conjugate photon with unit probability.

In practice, however, detector efficiency, transmission losses, and spatially multi-mode SPDC emission lead to a large overhead of detected single-photons whose partner is never detected, but which nonetheless contribute to the detector saturation and accidental coincidences. Consequently, reducing the number of single-photon detections for a given pair rate (i.e. improving the heralding) leads to higher manageable pair rates. As discussed in chapter 4, optimizing the source's heralding efficiency in bulk SPDC leads to lower total pair-collection efficiency. However, as long as the efficiency is sufficiently high, and limited pump power is not an issue, the decrease in pair rate can be mitigated by increasing the pump power.

In addition to such practical considerations, sources with a high heralding efficiency [89,184,241,253,254] are also of fundamental importance to loop-hole-free test of quantum theory [11,149,255], device independent quantum key distribution, and other loss-sensitive experiments.

7.2 Technical Implementation

The symmetric Sagnac interferometer configuration, discussed in section 2.4.2, is particularly well-suited for simultaneously achieving high brightness and heralding efficiency. In contrast to other schemes, such as the sandwiched crystal scheme (in which the pump waist is located at the center interface of two crossed crystals), the symmetric geometry of the interferometer allows for the beam waists of pump- and collection modes to be focused at the center of the nonlinear crystal. This optimizes spatial overlap of SPDC emission and the fiber-matched collection modes, which is particularly important when using long periodically poled nonlinear crystals.

Achieving a perfectly symmetric Sagnac loop in practice is challenging; both the clockwise and counter-clockwise propagation modes must overlap with the spatial modes of the collection optics and all beam waists should be located at the crystal center [252]. Also, the mechanical degrees of freedom (mirror angles etc.) used to align the counter-clockwise and clockwise propagation modes of pump and collection modes are coupled. Therefore, optimizing the efficiency of a Sagnac source requires an iterative alignment procedure, which is significantly more cumbersome than that of the sandwich and folded sandwich sources.

A significant advantage of the Sagnac scheme is the auto-compensating nature of the configuration, which made it possible to switch between operation in non-degenerate type-0 [256] and type-II QPM [90] configurations without adding specifically tailored walk-off compensation crystals, as required, for instance, in sandwiched crystal, or folded sandwich configurations.

Optimal focus parameters

In chapter 4 we discussed the dependence of heralding efficiency and pair rate of an entangled photon source on the choice of beam parameters of the pump and collection modes. We saw that the source brightness was optimized for different

focus parameters than the heralding efficiency, and that, in designing a source, a trade-off between the two quantities had to be made. We also saw how the heralding efficiency could be improved in a more beneficial trade-off with pair rate, by using spectral filters with a pass-band smaller than the natural SPDC bandwidth. While such filters (with near top-hat spectral profile) indeed exist for the typical bandwidths ($\sim 2-3nm$) observed in type-0 SPDC with a 20-mm ppKTP crystal (see Chapter 3), it requires overlapping two filters, each matching one of the non-degenerate wavelengths. For the bandwidths of the degenerate type-II, such narrow filters are not yet available as off-the-shelf commercial products, and would have to be custom-made at significant cost. Consequently, while non-optimal regarding the trade-off between pair rate and heralding efficiency, optimizing the heralding efficiency by choosing a large pump waist, as opposed to spectral filtering, offers a larger degree of flexibility in the operating wavelengths.

We chose the largest pump waist that could be accommodated by the 1x2mm2 aperture of our 20-mm-long ppKTP crystal (pump beam waist: $w_p \sim 150\mu$m; collection fiber modes: $w_s \sim 80\mu$m). While optimal for heralding efficiency, this came at the cost of brightness, which was a factor ~ 0.1 of the peak brightness achievable for smaller waist combinations. For this geometry we determined the loss due to single-mode fiber coupling to be less than 10%, by comparing the heralding efficiencies obtained with the Nufern HP780 single-mode fibers used in the experiment and multi-mode fibers.

Crossed-faced periscope

The Sagnac configuration (see Chapter 2) requires the polarization of pump (SPDC) photons to be flipped when passing through the interferometer in the counter-clockwise (clockwise) propagation direction. This polarization transformation can be achieved in various ways, such as a Fresnel Rhomb, or a dual-wavelength half-wave plate (dHWP) oriented at 45°. Since the dHWP is necessarily a higher-order wave plate, it consequently has a small operational wavelength range. As in the folded sandwich source, the functionality of the wave plate is more critical at the SPDC wavelength, where imperfect implementation of the polarization flip would reduce the entanglement visibility, as opposed to the pump, where it affects only the efficiency of the SPDC process. Alternatively, one could use an achromatic NIR half-wave plate - however, while this would not affect the achievable visibility, the efficiency would be reduced, as the pump polarization would not be flipped perfectly. The Fresnel Rhomb, on the other hand, is a bulky optical element, and the dispersion introduced in the long internal optical path would have required two Rhomboids to be placed before and after the nonlinear crystal, in order to avoid which-polarization timing information due to dispersive walk-off. Instead, we used a cross-faced periscope (P1) to flip the polarization of pump and SPDC photons. The polarization flip introduced by a cross-faced periscope is achieved by flipping the coordinate system and is thus independent of the wavelength. This requires the crystal to be placed in a different plane than the polarizing beam split-

ter. The required displacement of the beam height was achieved using an additional parallel-faced periscope (P2), which left the polarization state of the pump and SPDC photons unchanged [256, 257]. This way the pump beam enters the crystal with a polarization parallel to the phase-matched axis for both clockwise and counter-clockwise propagation directions, and temporal indistinguishability between the orthogonally-polarized signal and idler photons, which arises due to birefringent (type-II) and dispersive (type-0) walk-off in the ppKTP crystal, is ensured.

Experimental setup

In the experimental setup (Fig. 7.1), a 405-nm grating-stabilized single-frequency laser diode was coupled into a single-mode fiber, and focused to a beam waist $w_p \sim 150\mu$m at the center of either a 20-mm-long type-0 or type-II ppKTP crystal. Note that, for optimal alignment of the Sagnac loop, the entire pump power is reflected back to the laser source. Consequently, an optical isolator (Faraday rotator with $> 50dB$ isolation, not depicted) was added to the fiber-coupled laser assembly, in order to prevent unwanted feedback into the laser diode.

The crystals were mounted side-by-side on a temperature controller (TEC) and could be exchanged using a translation stage. For the type-0 crystal the temperature was set to 30°, in order to quasi-phase match the collinear non-degenerate type-0 SPDC process with center wavelengths of ∼784 nm (signal) and ∼839 nm (idler). For the type-II sample the temperature was set to 35 °C, to phase-match a degenerate type-II SPDC process around 810nm.

The crystals were placed at the center of a Sagnac interferometer, which consisted of a dual-wavelength polarizing beam splitter cube (dPBS - anti-reflection coated at 810nm and 405nm), two periscopes (P1,P2), and two additional beam-steering mirrors (broadband highly reflective).

With either the type-0 or the type-II ppKTP sample placed in the pump beam, the signal and idler photons generated in the nonlinear crystal were isolated from the pump photons via a highly reflective dichroic mirror (DM1) and each coupled into a Nufern 780HP single-mode fiber, using an f=18.4-mm aspheric lens.

Note that in the type-II configuration, signal and idler photons exit through distinct exit ports of the dPBS, whereas in the type-0 configuration, SPDC from both propagation modes is emitted back into the pump mode. Correspondingly, in the type-0 configuration the signal and idler were split using a dichroic mirror (DM2) with its transition edge at 810nm. The dichroic mirror (DM2) and a beam-steering mirror (M2) were mounted on flip-mirror mounts, to facilitate switching between the two modes of operation (after changing from one mode of operation to the other, the output couplers required some slight re-alignment).

When the relative magnitude of the horizontally and vertically polarized pump components are set accordingly, photon pairs are equally likely to be generated in either clockwise or counter-clockwise emission modes, and a polarization-entangled state of the form $|\Phi(\phi)\rangle = \frac{1}{\sqrt{2}}\left(|V_{\lambda_s}V_{\lambda_i}\rangle + e^{i\phi}|H_{\lambda_s}H_{\lambda_i}\rangle\right)$ or $|\Psi(\phi)\rangle = \frac{1}{\sqrt{2}}\left(|V_{\lambda_s}H_{\lambda_i}\rangle + e^{i\phi}|H_{\lambda_s}V_{\lambda_i}\rangle\right)$

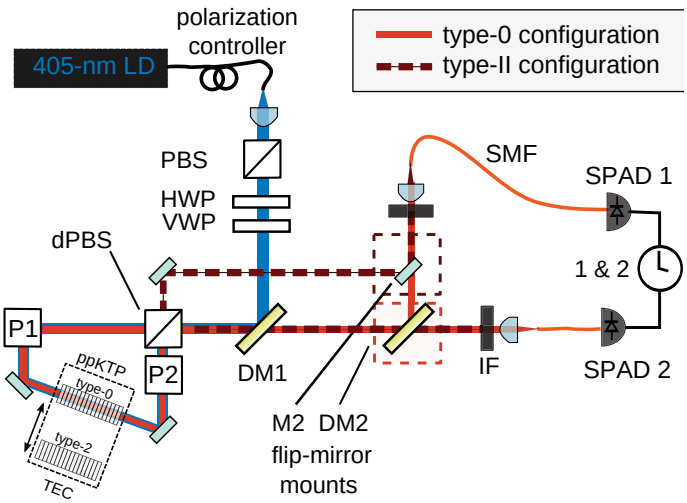

Figure 7.1: Schematic set-up of the Sagnac interferometer: A 405-nm cw laser diode, with its polarization-state set by combining a polarizing beam splitter (PBS), half-wave plate (HWP) and variable-wave plate (VWP), is focused to the center of one of two ppKTP crystals (type-0/II), placed at the center of the Sagnac loop. The Sagnac interferometer consisted of a dual-wavelength polarizing beam splitter (dPBS), two periscopes (P1,P2) and broad-band high-reflection coated mirrors. The down-converted photons traverse interference filters (IF) and are coupled into single-mode fibers (SMF). Dichroic mirror (DM2) and mirror (M2), mounted on flip-mirror mounts, allowed switching between type-0 and type-II configurations. The photon pairs were detected using two SPADs and two-fold pair-detection events were identified using a fast coincidence counting logic (&).

results for the type-0 and type-II QPM, respectively. Equal pair-emission probabilities were ensured by setting the polarization of the incoming pump beam to balance the respective coincidence rates via a half-wave plate (HWP). The relative phase of the entangled state ϕ was then set by tilting a variable wave plate (VWP), which was located in the pump path, about its optical axis. The VWP consisted of 100μm YVO_4.

7.3 Experimental Performance

The signal and idler photons were detected via two fiber-coupled single-photon avalanche detectors (SPADs) and two-photon detections were identified using an FPGA-based AND gate with the coincidence window set to $\sim$4.5ns. The Bell-state fidelity was evaluated using Eq. 2.38. For both ppKTP samples the fidelity was assessed at low flux-rates, such that the impact of accidental coincidences on the fidelity was negligible [182, 184, 220].

Type-II QPM configuration

For a pump power of 1.7 mW incident on the type-II crystal, there was a broadband background from fluorescence. These background counts were uncorrelated in time and lead only to background singles, but not coincidence counts. In order to obtain a high heralding efficiency, interference filters centered at 810nm with a 3nm FWHM passband (significantly larger than the SPDC bandwidth of ~ 0.3 nm) were inserted into the paths of both signal and idler photons. With the interference filters in place we detected a coincidence rate of R_c = 12.4kcps and singles rates of R_s =34 kcps and R_i =31 kcps, corresponding to a detected pair rate of 0.007 Mcps/mW and a detected spectral brightness of 0.02 Mcps/mW/nm. Without correcting for background counts, losses, or detection inefficiency, we measured an overall signal (idler) heralding efficiency of $\eta_s = R_c/R_i = 0.40$ ($\eta_i = R_c/R_s = 0.37$). The heralding efficiencies achieved while bi-directionally pumping the Sagnac loop (Tab. 7.2), were approximately 10% lower than when pumping only in the clockwise direction (Tab. 7.1), due to imperfect alignment of the clockwise and counter-clockwise propagation modes. Note that this alignment issue has since been resolved, and the source yields essentially the same heralding efficiencies for bi-directional and uni-directional pumping.

The high degree of polarization entanglement was confirmed at low flux-rates, where we measured visibilities $V_{H/V} = 99.7\pm0.1\%, V_{D/A} = 98.9\pm0.2\%, V_{L/R} = 98.9 \pm 0.2\%$, corresponding to F$= 99.4 \pm 0.2\%$. The visibility observed for both type-0 and type-II quasi-phase-matching configurations was remarkably stable over time (several hours under laboratory conditions).

Type-0 QPM configuration

Operating in a type-0 QPM configuration, the source is capable of significantly higher pair rates. However, owing to the larger spectral bandwidth, clockwise and counter-clockwise SPDC emission acquired slightly different phase characteristics over the entire bandwidth (possibly due to group-velocity dispersion in mirrors and dPBS). A high degree of polarization entanglement could still be achieved by placing an interference filter (FWHM$\sim$3.5nm) and a thin birefringent compensation crystal (100μm YVO_4) in the signal path. At low pair rates we obtained $V_{H/V} = 99.7 \pm 0.1\%, V_{D/A} = 98.3 \pm 0.2\%, V_{L/R} = 98.4 \pm 0.2\%$, which corresponds to F$= 99.1 \pm 0.2\%$.

With the polarizers removed from the setup, we detected a coincidence rate of R_c = 19 kcps and singles rates of R_s =63 kcps and R_i =62 kcps, at a pump power of 0.03 mW, which corresponds to a normalized detected pair rate of 0.5 Mcps/mW and a detected spectral brightness of 0.22 Mcps/mW/nm.

The heralding efficiency was lower in the type-0 configuration, since the dPBS was specifically designed for 810nm and 405nm, and not for triple-wavelength operation, as required for non-degenerate type-0 SPDC. The limited extinction of the dPBS resulted in a slightly higher loss and correspondingly a lower heralding

config.	λ_s, λ_i	$\Delta\lambda_s$	Mcp/mW	Mcp/mW/nm	η_s, η_i
type-0	784nm,839nm	$\sim$2.3nm	1	0.46	0.45 , 0.35
type-II[1]	810nm,810nm	$\sim$0.3nm	0.008	0.026	0.45 , 0.39

[1] Spectral interference filters centered at 810nm (FWHM $\sim$ 3nm) were inserted, to reduce detected singles coming from fluorescence.

Table 7.1: Performance characteristics of non-degenerate type-0 and degenerate type-II SPDC in uni-directionally pumped Sagnac-loop. We consider the full width at half maximum bandwidth (FWHM) of the generated photons ($\Delta\lambda$), the detected pair rate per mW of incident pump power, the spectral brightness in pairs per mW and per nm of bandwidth, and heralding efficiencies η_s (η_i) of signal (idler) photons.

efficiency (see Tabs. 7.2 and 7.1).

7.4 Conclusions

In this chapter I reported on a bright, high-heralding-efficiency source of polarization-entangled photons based on SPDC from a single 20-mm ppKTP crystal in a Sagnac interferometer. In contrast to the sources presented in the previous sections, the source was optimized with respect to heralding efficiency, which lead to non-record pair generation rates due to the trade-off in the focusing conditions. The source could be operated in both type-0 and type-II phase-matching configurations, by making only minor modifications to the optical setup. The brightness and heralding efficiency achieved for both configurations is compared to other state-of-the art sources in Fig. 7.3 and Fig 7.2. As expected from the different nonlinear coefficients, type-0 SPDC in ppKTP was significantly more efficient than type-II, allowing for both high brightness and heralding efficiency. However, due to losses in the optical components (which were designed for down-converted photons at 810nm) the heralding efficiency for degenerate type-0 QPM was lower than for non-degenerate type-0 SPDC.

A high degree of polarization entanglement could be achieved for both operations in type-0 and type-II quasi-phase-matching configurations. The emitted state had a fidelity of more than 99% with an ideal Bell state and was stable over several hours under laboratory conditions.

The realization of a compact Sagnac interferometer EPS, which can sustain strong vibrations and thermal fluctuations, is the subject of an ongoing study funded by the European Space Agency.

Table 7.2: Low-flux performance characteristics of the entangled photon source for type-0 and type-II QPM in bi-directionally pumped configurations, with balanced clockwise and counter-clockwise SPDC emission. All data were obtained with interference filters in place. Type-0 SPDC is more efficient in terms of spectral brightness and normalized pair rate, where the difference is even stronger due to the larger bandwidth. The heralding efficiencies of signal and idler photon were higher for type-II SPDC, mainly due to losses in the optical components that were designed for down-converted photons at 810nm.

config.[1]	$\Delta\lambda_s$	Mcp/mW	Mcp/mW/nm	η_s, η_i	Fidelity[2]
type-0[3]	$\sim$2.3 nm	0.5	0.22	0.31, 0.31	$99.1 \pm 0.2\%$
type-II	$\sim$0.3 nm	0.007	0.02	0.40, 0.37	$99.4 \pm 0.2\%$

[1] Polarizers removed from setup for efficiency measurements.

[2] Thin-film polarizers and achromatic quarter-wave plates were inserted for the fidelity measurement.

[3] Compared to the configuration used in Table 1, an interference-filter centered at 785-nm (3.5nm FWHM) was added in the signal arm.

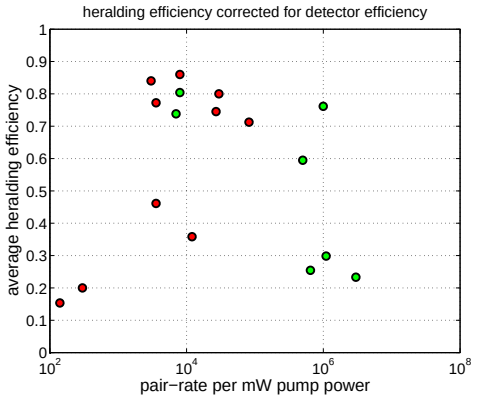

Figure 7.2: Average heralding efficiency $\sqrt{\eta_s \eta_i}$, with correction for detector efficiency, versus normalized pair-detection rate for state-of-the-art entangled photon sources based on bulk SPDC. The green data represent heralding efficiencies obtained in the sources presented in this thesis, the red data correspond to the state of the art sources. The publications from which the data was extracted are listed in Appendix A.

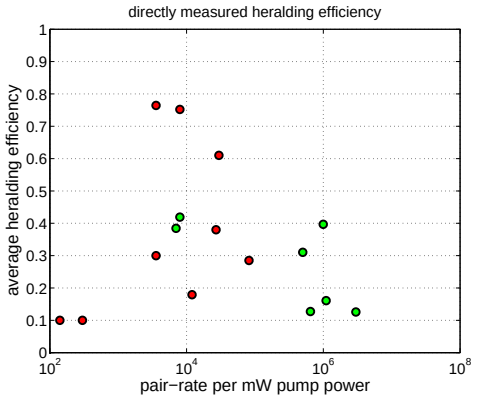

Figure 7.3: Average heralding efficiency $\sqrt{\eta_s \eta_i}$, without (bottom) correction for detector efficiency, versus normalized pair-detection rate for state-of-the-art entangled photon sources based on bulk SPDC. The green data represent heralding efficiencies obtained in the sources presented in this thesis, the red data correspond to the state of the art sources. The publications from which the data was extracted are listed in Appendix A.

Chapter 8

Summary and Outlook

A key challenge for the realization of quantum experiments in space and the demonstration of quantum communication protocols over satellite links is the development of robust, compact, and space-proof sources of entangled photons with both high brightness and entanglement visibility.

The fundamental aim of this thesis was to push the limits of sources of entangled photons in terms of pair-generation efficiency and to control the photon pairs' spectral and spatial characteristics. Special emphasis in the design of the entangled photon sources was placed on using simple and rugged configurations with a compact footprint, as well as using only components that can be further integrated and are compliant with the severe requirements of space flight and operation in space.

The sources presented in this thesis were based on the process of spontaneous parametric down-conversion (SPDC) in periodically poled potassium titanyl phosphate (ppKTP). In order to explore the limits of the SPDC process in terms of efficiency, a sound understanding of the SPDC pair-generation process was necessary. To this end, a detailed study of the spectral and spatial properties of photon pairs generated via SPDC in ppKTP in both type-0 and type-II quasi-phase-matching configurations was conducted. The main focus therein was set on the optimization of the spectral efficiency (Chapter 3) and the fiber-coupling efficiency (Chapter 4). The results of these studies were corroborated experimentally, and subsequently used to achieve unprecedented efficiency in sources of entangled photons (see comparative Table in Appendix A).

In the course of this thesis, three highly efficient sources of polarization-entangled photon pairs were developed and characterized:

The first source (Chapter 5) is based on a crossed-crystal (also "sandwich") configuration, and was developed as part of the ESA-funded EQUO project. Special emphasis in this project was placed on maintaining a compact footprint: all of the source components, including pump laser and driving electronics, were mounted on a compact breadboard, which was subsequently delivered to ESA (the hardware remained at ICFO on the basis of a loan agreement). Out of the sources presented in this thesis, the type-0 crossed-crystal source is the most straight-

forward to implement in terms of the alignment procedure, and is also the most straightforward approach when it comes to further integration. The efficiency and the quality of the entangled state, however, are limited by problems associated with the use of two nonlinear crystals, mainly due to differences in both spectral characteristics and efficiency that vary for distinct nonlinear crystals. Furthermore, good temperature stabilization is critical due to the strongly temperature-dependent spectral characteristics of the type-0 SPDC process (see Chapter 3), as well as the temperature dependence of the phase of the entangled state. Improving the temperature stability of the phase by using athermal compensation crystal configurations needs to be the subject of further research. An alternative that is still to be characterized in terms of temperature stability is a non-degenerate type-II sandwich source.

The second source (Chapter 6) is an iteration of the EQUO source, and was based on a novel "folded sandwich" configuration. Using knowledge acquired in the EQUO project, we were able to implement a number of technical improvements, which led to higher brightness, stability, and entanglement fidelity ($>99\%$).

In terms of pair-generation efficiency, the folded sandwich source excels due to the recycling of pump power and the usage of only a single nonlinear crystal. There is no loss in efficiency when spatially overlapping SPDC emission from long crystals as the beam waists of the pump beam driving first and second pass SPDC emissions are both located at the center of the nonlinear crystal.

The third source (Chapter 7), based on the Sagnac-loop configuration, was optimized to allow for the highest useful pair rates when taking into account detector limitations. In order to limit detector saturation and multi-pair emissions for a given pair rate, the source was optimized with respect to the coincidence-to-singles ratio (heralding efficiency), which resulted in non-optimal brightness, but led to one of the highest heralding efficiencies directly detected with silicon-based single-photon avalanche detectors.

The efficiency of the sources developed in this thesis allows for maximal pair rates that extend beyond the capabilities of state-of-the-art single-photon detectors. Once the emitted pair rate becomes large compared to the electronic coincidences window used to identify the entangled photon pairs (t_c), multiple pairs emitted within t_c lead to an increased number of so-called accidental coincidences. The minimum coincidence window in experiments is set by the detectors' timing jitter and timing synchronization between the receivers. Since the coherence time of the SPDC photon pairs is small ($\sim$ 1 ps) compared to the typical size of t_c ($\sim$ 1 ns), these accidental coincidences stem from uncorrelated photon pairs and lead to a decrease in two-photon entanglement visibility.

This clearly demonstrates that, in order to achieve higher bit rates in quantum communications links based on SPDC, future research projects must include further advances in detector technology, in particular the development of detectors with high efficiency and low timing jitter, as well as schemes for clock synchronization and path length correction from the satellite to receivers with sub-nanosecond precision.

Main achievements

Specific achievements in this thesis include:

- Detailed study of spectral properties of SPDC emission, and first conclusive comparison of collinear type-0 and type-II quasi-phase-matching configurations in ppKTP, pumped with either continuous-wave or free-running laser diodes.
- Theoretical calculation of the fiber-coupling efficiency of SPDC photon pairs generated in periodically poled nonlinear crystals, and evaluation of the effect of additional spectral filtering. The results were subsequently validated in a series of experiments and led to an improved understanding of the theory of SPDC with Gaussian beams.
- Development of high-brightness and high-visibility source of polarization-entangled photons based only on space-proof components, and subsequent delivery of EPS to ESA, thus successfully closing EQUO project (ESA/ESTEC contract 22542/09/NL/SFe).
- Demonstration of source of polarization-entangled photons in a novel folded sandwich configuration, and achievement of unprecedented performance with respect to previous state of the art (see comparative table in Appendix A):

  Detected spectral brightness ($\sim$1 Mcps/mW/nm) was improved by factor > 3.

  Normalized pair-detection rate ($\sim$3 Mcps/mW) was improved by more than an order of magnitude.
- Demonstration of a Sagnac source of polarization-entangled photons with one of the highest symmetric heralding efficiencies directly observed using silicon SPADs (without correction for detection loss or dark counts).
- Thanks to the performance demonstrated, the sources developed will provide an enabling tool for future experiments and collaborations, and have already been incorporated into ongoing experiments, for example in quantum nanophotonics and quantum communications.

Outlook

Many obstacles remain in the pursuit of global-scale quantum optics experiments using ground-to-satellite, satellite-to-ground, or inter-satellite links. These include minimizing the link loss via adaptive optics, faster drift compensation, automatic tracking and link optimization, and improved pointing stability of transmitter and receiver telescopes, as well as establishing and maintaining a common polarization reference frame. In terms of detection electronics, further improvements in

timing and synchronization, accurate time-tagging, and low-timing-jitter single-photon detection with high peak count rates are required.

Regarding the design of entangled photon sources, the main challenges to be addressed are: further integration, improvement of mechanical and thermal stability, and implementation of remote possibilities for re-alignment, control and performance checks.

The engineering of robust ultra-narrowband or pulsed sources (e.g., for multi-photon experiments) and ultra-broadband sources (e.g., for clock synchronization) will also have to be addressed in further studies.

While the developments in competing technologies for the generation of entangled photon pairs (see Chapter 1) make them viable alternatives in the long term, SPDC in bulk crystals still seems to be the primary solution for the first generation of experiments in space. And while other EPS bulk crystal schemes may emerge in the near future, it is highly likely that the first generation of sources of entangled photons to deployed in space will be based on one of the schemes presented in this thesis. One open question may concern the choice of nonlinear crystals, taking into account a trade-off between efficiency and thermal stability.

The realization of a power-efficient prototype that can sustain the strong vibrations and thermal fluctuations of space flight and operation in space will be a critical step toward the implementation of experiments with entangled photons in space, and is the subject of both ongoing and future studies funded by the European Space Agency.

Appendix A: State-of-the-art polarization-entangled photon sources

Process (Material)	Comments	Pair Rate cps/mW	Spectral Brightness cps/mW/nm	λ_s, λ_i ($\Delta\lambda_{FWHM}$)	η_s (η_s/η_{det})	η_i (η_s/η_{det})	Fidelity	Reference
non-collinear type-II PM (BBO)	overlapping cones	10	2	702nm,702nm (5nm)	-	-	98.4%	Kwiat 1995 [83]
non-collinear type-I PM (BBO)	sandwich	140	28	702nm,702nm (5nm)	10% (15%)		99.7%	Kwiat 1999 [88]
collinear type-II QPM (ppKTP)	beam splitter post-selection	3×10^2	3×10^2	795nm,795nm (1nm)	10% (20%)		99.3%	Kuklewicz 2004 [92]
collinear type-II QPM (ppKTP)	bi-directional Mach-Zehnder	12×10^3	4×10^3	797nm,797nm (3nm)	18% (36%)		92%	Fiorentino 2004 [258]
non-collinear type-II QPM (ppKTP)	overlapping cone	8×10^2	8×10^2	797nm,797nm (1nm)	-	-	97%	Fiorentino 2005 [259]
non-collinear type-I PM (BBO)	sandwich	3.6×10^3	1.4×10^2	701nm,701nm (25nm)	30% (46%)		97.7%	Altepeter 2005 [260]
collinear type-II QPM (ppKTP)	Sagnac loop	3.6×10^3	1.4×10^2	810nm,810nm (1nm)	-	-	97.6%	Kim 2006 [174]
collinear type-II QPM (ppKTP)	Sagnac loop, tunable wavelength, SMF-coupled	8.2×10^4	2.7×10^5	810nm$\pm$26nm (0.3nm)	20% (71%)		99.6%	Fedrizzi 2007 [90]
collinear type-I (BBO)	sandwich, free-running pump, SMF-coupled	2.7×10^4	1.8×10^3	790nm,830nm (14.5nm)	38% (75%)		99.4%	Trojek 2008 [89]
non-collinear type-I PM (BBO,BiBO)	sandwich, pulsed pump	1.3×10^4	-	-	-	-	99%	Rangarajan 2009 [261]
collinear type-II QPM (ppKTP)	Sagnac loop, pulsed pump, SMF-coupled	4×10^4	1.5×10^4	808nm,808nm (2.67nm)	-	-	98.3%	Predojevic 2012 [252]
collinear type-II QPM (ppKTP)	Sagnac loop, TES detectors, 1550-nm SMF	4×10^4	8×10^4	820nm,820nm (0.5nm)	62% (80%)		98%	Smith 2012 [262]
collinear type-0 QPM (ppKTP)	sandwich, SMF-coupled	6.4×10^5	2.8×10^5	783nm,839nm (2.3nm)	18% (36%)	9% (18%)	98.3%	Steinlechner 2012[1] [236]
collinear type-II QPM (ppKTP)	pair source, SMF-coupled	3×10^3	1.5×10^4	810nm,810nm (0.2nm)	(84.4%)	(83.7%)	-	Cunha Pereira 2013 [241]
collinear type-II QPM (ppKTP)	Sagnac loop, TES detectors, 1550-nm SMF	10^4	2×10^4	810nm,810nm (0.5nm)	12%	83%	92%	Ramelow 2013 [184]
non-collinear type-I PM (BiBO)	crossed crystal, TES detectors, SMF			710nm,710nm ($\sim$20nm)	75%		99.8%	Christensen 2013 [149]
collinear type-II QPM (ppKTP)	Sagnac loop, TES detectors, 1550-nm SMF	10^4	2×10^4	810nm,810nm (0.5nm)	74%	79%	97%	Giustina 2013 [11]
collinear type-0 QPM (ppKTP)	folded sandwich, SMF-coupled	1.1×10^6	3.9×10^5	783nm,839nm (2.9nm)	19% (35%)	13% (25%)	99.1%	Steinlechner 2013[1] [220]
collinear type-II QPM (ppKTP)	Sagnac loop, SMF-coupled	8×10^3	2.7×10^4	810nm,810nm (0.3nm)	45% (83%)	39% (78%)	99.4%	Steinlechner 2014[1] [263]
collinear type-0 QPM (ppKTP)	Sagnac loop, SMF-coupled	1×10^6	4×10^5	783nm,839nm (2.3nm)	45% (83%)	35% (70%)	99.1%	Steinlechner 2014[1] [263]
collinear type-0 QPM (ppKTP)	folded sandwich, SMF-coupled	3×10^6	1×10^6	783nm,839nm (3nm)	18% (32%)	9% (17%)	98.3%	Steinlechner 2014[1]
collinear type-II QPM (ppKTP)	Sagnac loop, TES detectors, SMF-coupled	8×10^3	2×10^4	810nm,810nm ($\sim$0.4nm)	81.4 (86%)	69.6 (86%)	99.8%	Joshi 2014 [264]

[1]This thesis.

Table 1: State-of-the-art bulk SPDC sources of polarization-entangled photon pairs in the 810-nm region. The pair-generation efficiencies are compared in terms of pair rate per mW of pump power R, the spectral brightness ($d\mathrm{R}/d\lambda$), without correction for detector efficiency or losses. The spectral characteristics listed are central wavelengths of the signal and idler photons (λ_s, λ_i) and the full width at half maximum bandwidth bandwidth ($\Delta\lambda_{FWWHM}$). In order to facilitate a comparison of the heralding efficiency for different detector efficiencies, we state both the uncorrected experimental values ($\eta_{s,i}$) as well as the values corrected for the estimated detector efficiency ($\eta_{s,i}/\eta_{det}$). The Bell-state fidelity is stated for low pump powers. In articles that stated the experimental visibility the fidelity was estimated.

Appendix B: SPDC Mode weights

Integrals used in derivation of the mode weights

The following integrals were used in the calculation of the SPDC mode weights in Chapter 4:

Gaussian integral

$$\int_{\infty}^{\infty} x^m \exp(-ax^2)dx = \frac{\Gamma(m+1)/2}{2a^{(m+1)/2}} \tag{1}$$

where for integer m, $\Gamma(m) = (m-1)!$.

Integrals of sinc(x)=$\sin(x)/x$

$$\int_{\infty}^{\infty} \frac{\sin(ax)}{ax}dx = \frac{\pi}{a} \tag{2}$$

$$\int_{0}^{\infty} \frac{\sin(ax^2)}{x^2}dx = \sqrt{\frac{a\pi}{2}} \tag{3}$$

$$\int_{0}^{\infty} e^{-px}\frac{\sin(ax)}{x}dx = \sqrt{\frac{a\pi}{2}} = \tan^{-1}\frac{a}{p}\ ,\ [p>0] \tag{4}$$

Modified Bessel function I_0

$$\int_{0}^{\infty} e^{-bx^2} I_0(ax) = \frac{1}{2b}e^{\frac{a^2}{4b}}dx \tag{5}$$

where the modified Bessel function is defined as:

$$I_0(x) = \frac{1}{2\pi}\int_{0}^{2\pi} \exp(x\cos(\phi))d\phi \tag{6}$$

Mode weights $C^{l1l2}_{p1p2}(\Omega)$

The mode amplitudes in Chapter 4 are calculated by projecting the bi-photon state in free-space (Eq. 4.16) onto the respective target modes:

$$C^{l_1 l_2}_{p_1 p_2}(\Omega) = \int d\mathbf{q}_s d\mathbf{q}_i \, \Phi\left(\mathbf{q}_s, \mathbf{q}_i, \Omega\right) U^*_{l_1 p_1}\left(\mathbf{q}_s\right) U^*_{l_2 p_2}\left(\mathbf{q}_i\right) \tag{7}$$

with the SPDC mode function:

$$\Phi(\mathbf{q}_s, \mathbf{q}_i, \Omega) = \frac{L\tilde{\sigma} w_p}{\sqrt{2\pi}} \exp\left(-\frac{|\mathbf{q_s} + \mathbf{q_i}|^2 w_p^2}{4}\right) \text{sinc}\left(\frac{|\mathbf{q}_s - \mathbf{q}_i|^2 L}{4k_p^0} - \frac{D\Omega L}{2}\right) \tag{8}$$

and the mode functions of the Laguerre-Gauss target modes:

$$\begin{aligned} U_{lp}(\mathbf{q}) = \quad & \left(\frac{w_0^2 p!}{2\pi(|l|+p)!}\right)^{1/2} \left(\frac{w_0 \rho}{\sqrt{2}}\right)^{|l|} L_p^l\left(\frac{\rho^2 w_0^2}{2}\right) \\ & \times \exp\left(-\frac{\rho^2 w_0^2}{4}\right) \exp\left[il\phi + \left(p - \left|\frac{l}{2}\right|\right)\pi\right] \end{aligned} \tag{9}$$

where $\rho = |\mathbf{q}|$ and ϕ are the cylindrical transverse coordinates. The function $L_p^{|l|}\left(\rho^2 w_0^2/2\right)$ is the associated Laguerre polynomial and w_0 is the beam waist. As discussed in Chapter 3, the calculation of the coupling efficiency and spectral characteristics of fiber-coupled SPDC photons, requires the calculation of the mode weights for $l1 = l2 = p1 = 0$. These can be expressed as:

$$\begin{aligned} C^{00}_{0p}(\Omega) = & \int_0^\infty d\rho_1 \int_0^\infty d\rho_2 \rho_1 \rho_2 L G_p^0(\rho_1^2 w_s^2/2) \\ & \times \exp(-\rho_1^2(w_p^2 + w_s^2/2)) \exp(-\rho_2^2(w_p^2/4 + w_s^2/4)) \\ & \times 2\pi I_0(\rho_1\rho_2(w_p^2 + w_s^2/2)) \text{sinc}\left(\frac{\rho_2^2 L}{4k_p^0} - \frac{D\Omega L}{2}\right) \end{aligned} \tag{10}$$

where $LG_p^0(x)$ denote the Laguerre polynomials. The mode-weights decrease rapidly with increasing order. Hence it was sufficient to consider only the first few mode weights in the calculation of the single-photon spectra. The first few Laguerre polynomials read:

$$\begin{aligned} LG_0^0(x) &= 1 \\ LG_1^0(x) &= 1 - x \\ LG_2^0(x) &= x^2/2 - 2x + 1 \\ LG_3^0(x) &= 1/6(-x^3 + 9x^2 - 18x + 6) \\ LG_4^0(x) &= 1/24(x^4 - 16x^3 + 72x^2 - 96x + 24) \end{aligned} \tag{11}$$

Note that the sinc(x) function in Eq. 8 can also be replaced by the integral representation sinc$(x) = \int_{-1}^{1} \exp(ixt)dt$. With some additional work, the ρ integrations in Eq. 10 can then carried out analytically, and one arrives at an alternative expression for the mode weights [229].

Bibliography

[1] A. Peres, *Quantum theory: concepts and methods*. Springer Science & Business Media, 1995, vol. 57.

[2] A. Einstein, B. Podolsky, and N. Rosen, "Can quantum-mechanical description of physical reality be considered complete?" *Physical review*, vol. 47, no. 10, p. 777, 1935.

[3] J. S. Bell *et al.*, "On the einstein-podolsky-rosen paradox," *Physics*, vol. 1, no. 3, pp. 195–200, 1964.

[4] J. Bell, R. A. Bertlmann, and A. Zeilinger, *Quantum (un) speakables: from bell to quantum information*. Springer Science & Business Media, 2002.

[5] N. Brunner, D. Cavalcanti, S. Pironio, V. Scarani, and S. Wehner, "Bell nonlocality," *Reviews of Modern Physics*, vol. 86, no. 2, p. 419, 2014.

[6] J. F. Clauser, M. A. Horne, A. Shimony, and R. A. Holt, "Proposed experiment to test local hidden-variable theories," *Phys. Rev. Lett.*, vol. 23, no. 15, pp. 880–884, Oct. 1969. [Online]. Available: http://link.aps.org/doi/10.1103/PhysRevLett.23.880

[7] A. Aspect, J. Dalibard, and G. Roger, "Experimental test of bell's inequalities using time-varying analyzers," *Physical review letters*, vol. 49, no. 25, p. 1804, 1982.

[8] J. D. Franson, "Bell inequality for position and time," *Physical Review Letters*, vol. 62, no. 19, pp. 2205–2208, May 1989. [Online]. Available: http://link.aps.org/doi/10.1103/PhysRevLett.62.2205

[9] P. G. Kwiat, P. H. Eberhard, A. M. Steinberg, and R. Y. Chiao, "Proposal for a loophole-free bell inequality experiment," *Phys. Rev. A*, vol. 49, no. 5, pp. 3209–3220, May 1994. [Online]. Available: http://link.aps.org/doi/10.1103/PhysRevA.49.3209

[10] G. Weihs, T. Jennewein, C. Simon, H. Weinfurter, and A. Zeilinger, "Violation of bell's inequality under strict einstein locality conditions," *Physical Review Letters*, vol. 81, no. 23, p. 5039, 1998.

[11] M. Giustina, A. Mech, S. Ramelow, B. Wittmann, J. Kofler, J. Beyer, A. Lita, B. Calkins, T. Gerrits, S. W. Nam, R. Ursin, and A. Zeilinger, "Bell violation using entangled photons without the fair-sampling assumption," *Nature*, vol. 497, pp. 7448 (227–230), 2013.

[12] W. Tittel and G. Weihs, "Photonic entanglement for fundamental tests and quantum communication," *Quantum Inf. and Comp.*, vol. 1, pp. 3–56, 2001. [Online]. Available: http://www.univie.ac.at/qfp/publications3/pdffiles/2001-14.pdf

[13] I. A. Walmsley and M. G. Raymer, "Toward quantum-information processing with photons," *Science*, vol. 307, no. 5716, pp. 1733–1734, 2005.

[14] N. Gisin and R. Thew, "Quantum communication," *Nature Photonics*, vol. 1, no. 3, pp. 165–171, 2007.

[15] D. Bouwmeester, J.-W. Pan, K. Mattle, M. Eibl, H. Weinfurter, and A. Zeilinger, "Experimental quantum teleportation," *Nature*, vol. 390, no. 6660, pp. 575–579, Dec. 1997. [Online]. Available: http://dx.doi.org/10.1038/37539

[16] R. Ursin, T. Jennewein, M. Aspelmeyer, R. Kaltenbaek, M. Lindenthal, P. Walther, and A. Zeilinger, "Communications: Quantum teleportation across the danube," *Nature*, vol. 430, no. 7002, pp. 849–849, 2004.

[17] M. A. Nielsen and I. L. Chuang, "Quantum computation and quantum information," 2000.

[18] A. Gatti, E. Brambilla, M. Bache, and L. A. Lugiato, "Correlated imaging, quantum and classical," *Physical Review A*, vol. 70, no. 1, p. 013802, Jul. 2004. [Online]. Available: http://link.aps.org/doi/10.1103/PhysRevA.70.013802

[19] V. Giovannetti, S. Lloyd, and L. Maccone, "Quantum metrology," *Physical review letters*, vol. 96, no. 1, p. 010401, 2006.

[20] V. D'Ambrosio, N. Spagnolo, L. Del Re, S. Slussarenko, Y. Li, L. C. Kwek, L. Marrucci, S. P. Walborn, L. Aolita, and F. Sciarrino, "Photonic polarization gears for ultra-sensitive angular measurements," *Nature Communications*, vol. 4, Sep. 2013. [Online]. Available: http://www.nature.com/ncomms/2013/130918/ncomms3432/full/ncomms3432.html

[21] F. Wolfgramm, C. Vitelli, F. A. Beduini, N. Godbout, and M. W. Mitchell, "Entanglement-enhanced probing of a delicate material system," *Nature Photonics*, vol. 7, no. 1, pp. 28–32, 2013.

[22] T. Jennewein, C. Simon, G. Weihs, H. Weinfurter, and A. Zeilinger, "Quantum cryptography with entangled photons," *Phys. Rev. Lett.*,

vol. 84, no. 20, pp. 4729–4732, May 2000. [Online]. Available: http://link.aps.org/doi/10.1103/PhysRevLett.84.4729

[23] W. Tittel, J. Brendel, H. Zbinden, and N. Gisin, "Quantum cryptography using entangled photons in energy-time bell states," *Physical Review Letters*, vol. 84, no. 20, p. 4737, 2000.

[24] N. Gisin, G. Ribordy, W. Tittel, and H. Zbinden, "Quantum cryptography," *Rev. Mod. Phys.*, vol. 74, no. 1, pp. 145–195, Mar. 2002. [Online]. Available: http://link.aps.org/doi/10.1103/RevModPhys.74.145

[25] A. Acín, N. Gisin, and L. Masanes, "From bell's theorem to secure quantum key distribution," *Physical review letters*, vol. 97, no. 12, p. 120405, 2006.

[26] A. POPPE, M. PEEV, and O. MAURHART, "Outline of the secoqc quantum-key-distribution network in vienna," *International Journal of Quantum Information*, vol. 06, no. 02, pp. 209–218, 2008. [Online]. Available: http://www.worldscientific.com/doi/abs/10.1142/S0219749908003529

[27] A. Treiber, A. Poppe, M. Hentschel, D. Ferrini, T. Loruenser, E. Querasser, T. Matyus, H. Huebel, and A. Zeilinger, "A fully automated entanglement-based quantum cryptography system for telecom fiber networks," *New Journal of Physics*, vol. 11, no. 4, p. 045013, 2009. [Online]. Available: http://stacks.iop.org/1367-2630/11/i=4/a=045013

[28] M. Jofre, M. Curty, F. Steinlechner, G. Anzolin, J. P. Torres, M. W. Mitchell, and V. Pruneri, "True random numbers from amplified quantum vacuum," *Optics Express*, vol. 19, no. 21, pp. 20 665–20 672, Oct. 2011. [Online]. Available: http://www.opticsexpress.org/abstract.cfm?URI=oe-19-21-20665

[29] C. Abellán, W. Amaya, M. Jofre, M. Curty, A. Acín, J. Capmany, V. Pruneri, and M. Mitchell, "Ultra-fast quantum randomness generation by accelerated phase diffusion in a pulsed laser diode," *Optics express*, vol. 22, no. 2, pp. 1645–1654, 2014.

[30] W. K. Wootters and W. H. Zurek, "A single quantum cannot be cloned," *Nature*, vol. 299, no. 5886, pp. 802–803, Oct. 1982. [Online]. Available: http://www.nature.com/nature/journal/v299/n5886/abs/299802a0.html

[31] H. Takesue, S. W. Nam, Q. Zhang, R. H. Hadfield, T. Honjo, K. Tamaki, and Y. Yamamoto, "Quantum key distribution over a 40-db channel loss using superconducting single-photon detectors," *Nature photonics*, vol. 1, no. 6, pp. 343–348, 2007.

[32] D. Stucki, N. Walenta, F. Vannel, R. T. Thew, N. Gisin, H. Zbinden, S. Gray, C. Towery, and S. Ten, "High rate, long-distance quantum key distribution over 250 km of ultra low loss fibres," *New Journal of Physics*, vol. 11, no. 7, p. 075003, 2009.

[33] T. Inagaki, N. Matsuda, O. Tadanaga, M. Asobe, and H. Takesue, "Entanglement distribution over 300 km of fiber," *Optics express*, vol. 21, no. 20, pp. 23 241–23 249, 2013.

[34] L.-M. Duan, M. Lukin, J. I. Cirac, and P. Zoller, "Long-distance quantum communication with atomic ensembles and linear optics," *Nature*, vol. 414, no. 6862, pp. 413–418, 2001.

[35] C. Simon, H. De Riedmatten, M. Afzelius, N. Sangouard, H. Zbinden, and N. Gisin, "Quantum repeaters with photon pair sources and multimode memories," *Physical review letters*, vol. 98, no. 19, p. 190503, 2007.

[36] H. Kimble, "The quantum internet," *Nature*, vol. 453, no. 7198, pp. 1023–1030, 2008.

[37] H.-J. Briegel, W. Dür, J. I. Cirac, and P. Zoller, "Quantum repeaters: The role of imperfect local operations in quantum communication," *Physical Review Letters*, vol. 81, no. 26, p. 5932, 1998.

[38] N. Sangouard, C. Simon, H. De Riedmatten, and N. Gisin, "Quantum repeaters based on atomic ensembles and linear optics," *Reviews of Modern Physics*, vol. 83, no. 1, p. 33, 2011.

[39] J. G. Rarity, P. R. Tapster, P. M. Gorman, and P. Knight, "Ground to satellite secure key exchange using quantum cryptography," *New J. Phys.*, vol. 4, no. 1, p. 82, 2002. [Online]. Available: http://stacks.iop.org/1367-2630/4/i=1/a=382

[40] M. Aspelmeyer, T. Jennewein, M. Pfennigbauer, W. Leeb, and A. Zeilinger, "Long-distance quantum communication with entangled photons using satellites," *arXiv:quant-ph/0305105*, May 2003, arXiv: quant-ph/0305105. [Online]. Available: http://arxiv.org/abs/quant-ph/0305105

[41] M. Pfennigbauer, M. Aspelmeyer, W. Leeb, G. Baister, T. Dreischer, T. Jennewein, G. Neckamm, J. Perdigues, H. Weinfurter, and A. Zeilinger, "Satellite-based quantum communication terminal employing state-of-the-art technology," *Journal of Optical Networking*, vol. 4, no. 9, pp. 549–560, 2005.

[42] P. Villoresi, T. Jennewein, F. Tamburini, M. Aspelmeyer, C. Bonato, R. Ursin, C. Pernechele, V. Luceri, G. Bianco, A. Zeilinger, and C. Barbieri, "Experimental verification of the feasibility of a quantum channel between

space and earth," *New Journal of Physics*, vol. 10, no. 3, p. 033038, 2008. [Online]. Available: http://stacks.iop.org/1367-2630/10/i=3/a=033038

[43] C. Bonato, A. Tomaello, V. D. Deppo, G. Naletto, and P. Villoresi, "Feasibility of satellite quantum key distribution," *New Journal of Physics*, vol. 11, no. 4, p. 045017, 2009. [Online]. Available: http://stacks.iop.org/1367-2630/11/i=4/a=045017

[44] T. Scheidl, R. Ursin, A. Fedrizzi, S. Ramelow, X.-S. Ma, T. Herbst, R. Prevedel, L. Ratschbacher, J. Kofler, T. Jennewein, and A. Zeilinger, "Feasibility of 300 km quantum key distribution with entangled states," *New Journal of Physics*, vol. 11, no. 8, p. 085002, Aug. 2009. [Online]. Available: http://iopscience.iop.org/1367-2630/11/8/085002

[45] D. Elser, T. Bartley, B. Heim, C. Wittmann, D. Sych, and G. Leuchs, "Feasibility of free space quantum key distribution with coherent polarization states," *New Journal of Physics*, vol. 11, no. 4, p. 045014, 2009. [Online]. Available: http://stacks.iop.org/1367-2630/11/i=4/a=045014

[46] J.-P. Bourgoin, E. Meyer-Scott, B. L. Higgins, B. Helou, C. Erven, H. HÃ$\frac{1}{4}$bel, B. Kumar, D. Hudson, I. D'Souza, R. Girard, R. Laflamme, and T. Jennewein, "A comprehensive design and performance analysis of low earth orbit satellite quantum communication," *New Journal of Physics*, vol. 15, no. 2, p. 023006, Feb. 2013. [Online]. Available: http://iopscience.iop.org/1367-2630/15/2/023006

[47] M. Aspelmeyer, H. R. Boehm, T. Gyatso, T. Jennewein, R. Kaltenbaek, M. Lindenthal, G. Molina-Terriza, A. Poppe, K. Resch, M. Taraba, R. Ursin, P. Walther, and A. Zeilinger, "Long-distance free-space distribution of quantum entanglement," *Science*, vol. 301, no. 5633, pp. 621–623, 2003. [Online]. Available: http://www.sciencemag.org/content/301/5633/621.abstract

[48] K. J. Resch, M. Lindenthal, B. Blauensteiner, H. R. Boehm, A. Fedrizzi, C. Kurtsiefer, A. Poppe, T. Schmitt-Manderbach, M. Taraba, R. Ursin, P. Walther, H. Weier, H. Weinfurter, and A. Zeilinger, "Distributing entanglement and single photons through an intra-city, free-space quantum channel," *Opt. Express*, vol. 13, no. 1, pp. 202–209, Jan. 2005. [Online]. Available: http://www.opticsexpress.org/abstract.cfm?URI=oe-13-1-202

[49] C.-Z. Peng, T. Yang, X.-H. Bao, J. Zhang, X.-M. Jin, F.-Y. Feng, B. Yang, J. Yang, J. Yin, Q. Zhang, N. Li, B.-L. Tian, and J.-W. Pan, "Experimental free-space distribution of entangled photon pairs over 13 km: Towards satellite-based global quantum communication," *Phys. Rev. Lett.*, vol. 94, p. 150501, Apr 2005. [Online]. Available: http://link.aps.org/doi/10.1103/PhysRevLett.94.150501

[50] I. Marcikic, A. Lamas-Linares, and C. Kurtsiefer, "Free-space quantum key distribution with entangled photons," *Applied Physics Letters*, vol. 89, no. 10, pp. –, 2006. [Online]. Available: http://scitation.aip.org/content/aip/journal/apl/89/10/10.1063/1.2348775

[51] T. Schmitt-Manderbach, H. Weier, M. Fuerst, R. Ursin, F. Tiefenbacher, T. Scheidl, J. Perdigues, Z. Sodnik, C. Kurtsiefer, J. G. Rarity, A. Zeilinger, and H. Weinfurter, "Experimental demonstration of free-space decoy-state quantum key distribution over 144 km," *Phys. Rev. Lett.*, vol. 98, no. 1, p. 010504, Jan. 2007. [Online]. Available: http://link.aps.org/doi/10.1103/PhysRevLett.98.010504

[52] R. Ursin, F. Tiefenbacher, T. Schmitt-Manderbach, H. Weier, T. Scheidl, M. Lindenthal, B. Blauensteiner, T. Jennewein, J. Perdigues, P. Trojek, and others, "Entanglement-based quantum communication over 144 km," *Nature physics*, vol. 3, no. 7, pp. 481–486, 2007.

[53] C. Erven, C. Couteau, R. Laflamme, and G. Weihs, "Entangled quantum key distributionover two free-space optical links," *Opt. Express*, vol. 16, no. 21, pp. 16 840–16 853, Oct 2008. [Online]. Available: http://www.opticsexpress.org/abstract.cfm?URI=oe-16-21-16840

[54] M. P. Peloso, I. Gerhardt, C. Ho, A. Lamas-Linares, and C. Kurtsiefer, "Daylight operation of a free space, entanglement-based quantum key distribution system," *New Journal of Physics*, vol. 11, no. 4, p. 045007, 2009. [Online]. Available: http://stacks.iop.org/1367-2630/11/i=4/a=045007

[55] A. Fedrizzi, R. Ursin, T. Herbst, M. Nespoli, R. Prevedel, T. Scheidl, F. Tiefenbacher, T. Jennewein, and A. Zeilinger, "High-fidelity transmission of entanglement over a high-loss free-space channel," *Nature Physics*, vol. 5, no. 6, pp. 389–392, 2009.

[56] X.-M. Jin, J.-G. Ren, B. Yang, Z.-H. Yi, F. Zhou, X.-F. Xu, S.-K. Wang, D. Yang, Y.-F. Hu, S. Jiang, T. Yang, H. Yin, K. Chen, C.-Z. Peng, and J.-W. Pan, "Experimental free-space quantum teleportation," *Nat Photon*, vol. 4, no. 6, pp. 376–381, Jun. 2010. [Online]. Available: http://dx.doi.org/10.1038/nphoton.2010.87

[57] T. Scheidl, R. Ursin, J. Kofler, S. Ramelow, X.-S. Ma, T. Herbst, L. Ratschbacher, A. Fedrizzi, N. K. Langford, T. Jennewein *et al.*, "Violation of local realism with freedom of choice," *Proceedings of the National Academy of Sciences*, vol. 107, no. 46, pp. 19 708–19 713, 2010.

[58] X.-S. Ma, T. Herbst, T. Scheidl, D. Wang, S. Kropatschek, W. Naylor, B. Wittmann, A. Mech, J. Kofler, E. Anisimova, and others, "Quantum teleportation over 143 kilometres using active feed-forward," *Nature*, vol. 489, no. 7415, pp. 269–273, 2012.

[59] S. Nauerth, F. Moll, M. Rau, C. Fuchs, J. Horwath, S. Frick, and H. Weinfurter, "Air-to-ground quantum communication," *Nature Photonics*, vol. 7, no. 5, pp. 382–386, 2013.

[60] B. Heim, C. Peuntinger, N. Killoran, I. Khan, C. Wittmann, C. Marquardt, and G. Leuchs, "Atmospheric continuous-variable quantum communication," *New Journal of Physics*, vol. 16, no. 11, p. 113018, 2014. [Online]. Available: http://stacks.iop.org/1367-2630/16/i=11/a=113018

[61] C. Erven, E. Meyer-Scott, K. Fisher, J. Lavoie, B. Higgins, Z. Yan, C. Pugh, J.-P. Bourgoin, R. Prevedel, L. Shalm *et al.*, "Experimental three-photon quantum nonlocality under strict locality conditions," *Nature Photonics*, vol. 8, no. 4, pp. 292–296, 2014.

[62] M. Jofre, G. Anzolin, F. Steinlechner, N. Oliverio, J. P. Torres, V. Pruneri, and M. W. Mitchell, "Fast beam steering with full polarization control using a galvanometric optical scanner and polarization controller," *Optics Express*, vol. 20, no. 11, pp. 12 247–12 260, May 2012. [Online]. Available: http://www.opticsexpress.org/abstract.cfm?URI=oe-20-11-12247

[63] J.-W. Pan, D. Bouwmeester, H. Weinfurter, and A. Zeilinger, "Experimental entanglement swapping: Entangling photons that never interacted," *Physical Review Letters*, vol. 80, no. 18, pp. 3891–3894, May 1998. [Online]. Available: http://link.aps.org/doi/10.1103/PhysRevLett.80.3891

[64] D. Kielpinski, V. Meyer, M. Rowe, C. Sackett, W. Itano, C. Monroe, and D. Wineland, "A decoherence-free quantum memory using trapped ions," *Science*, vol. 291, no. 5506, pp. 1013–1015, 2001.

[65] M. P. Hedges, J. J. Longdell, Y. Li, and M. J. Sellars, "Efficient quantum memory for light," *Nature*, vol. 465, no. 7301, pp. 1052–1056, 2010.

[66] E. Saglamyurek, N. Sinclair, J. Jin, J. A. Slater, D. Oblak, F. Bussières, M. George, R. Ricken, W. Sohler, and W. Tittel, "Broadband waveguide quantum memory for entangled photons," *Nature*, vol. 469, no. 7331, pp. 512–515, 2011.

[67] M. Gündogan, M. Mazzera, P. M. Ledingham, M. Cristiani, and H. de Riedmatten, "Coherent storage of temporally multimode light using a spin-wave atomic frequency comb memory," *New Journal of Physics*, vol. 15, no. 4, p. 045012, 2013. [Online]. Available: http://stacks.iop.org/1367-2630/15/i=4/a=045012

[68] M. Halder, A. Beveratos, N. Gisin, V. Scarani, C. Simon, and H. Zbinden, "Entangling independent photons by time-measurement," *Nature Physics*, vol. 3, no. 10, pp. 692–695, Oct. 2007. [Online]. Available: http://www.nature.com/nphys/journal/v3/n10/full/nphys700.html

[69] M. Zukowski, A. Zeilinger, M. A. Horne, and A. K. Ekert, ""event-ready-detectors" bell experiment via entanglement swapping," *Phys. Rev. Lett.*, vol. 71, pp. 4287–4290, Dec 1993. [Online]. Available: http://link.aps.org/doi/10.1103/PhysRevLett.71.4287

[70] M. Halder, A. Beveratos, R. T. Thew, C. Jorel, H. Zbinden, and N. Gisin, "High coherence photon pair source for quantum communication," *New J. Phys.*, vol. 10, no. 2, p. 023027, 2008. [Online]. Available: http://stacks.iop.org/1367-2630/10/i=2/a=023027

[71] F. Wolfgramm, X. Xing, A. Cere, A., A. Predojevi?, A. M. Steinberg, and M. W. Mitchell, "Bright filter-free source of indistinguishable photon pairs," *Optics Express*, vol. 16, no. 22, pp. 18 145–18 151, Oct. 2008. [Online]. Available: http://www.opticsexpress.org/abstract.cfm?URI=oe-16-22-18145

[72] F. Kaiser, A. Issautier, L. A. Ngah, O. Alibart, A. Martin, and S. Tanzilli, "A versatile source of polarization entangled photons for quantum network applications," *Laser Physics Letters*, vol. 10, no. 4, p. 045202, Apr. 2013. [Online]. Available: http://iopscience.iop.org/1612-202X/10/4/045202

[73] F. Monteiro, A. Martin, B. Sanguinetti, H. Zbinden, and R. T. Thew, "Narrowband photon pair source for quantum networks," *Opt. Express*, vol. 22, no. 4, pp. 4371–4378, Feb 2014. [Online]. Available: http://www.opticsexpress.org/abstract.cfm?URI=oe-22-4-4371

[74] R. Ursin, G. Milburn, M. Peev, T. Ralph, J. G. Rarity, R Renner, N. Solomos, W. Tittel, J. P. Torres, M. Toyoshima, P. Villoresi, I. Walmsley, G. Weihs, H. Weinfurter, M Zukowski, N. Luetkenhaus, R. Laflamme, R. H. Hadfield, T Jennewein, J. Kofler, J. Perdigues, L. Cacciapuoti, C. Matos, M. Aspelmeyer, A. Valencia, T. Scheidl, A. Acin, C. Barbieri, G. Bianco, S. Cova, D. Giggenbach, W. Leeb, and A. Zeilinger, "Space-QUEST. experiments with quantum entanglement in space," in *Proceedings of the 2008 Microgravity Sciences and Process Symposium*. Glasgow, Scotland, UK: American Institute of Physics, arXiv:0806.0945v1 [quant-ph] 5 Jun 2008.

[75] H.-K. Lo, X. Ma, and K. Chen, "Decoy state quantum key distribution," *Physical Review Letters*, vol. 94, no. 23, p. 230504, 2005.

[76] M. Jofre, A. Gardelein, G. Anzolin, W. Amaya, J. Capmany, R. Ursin, L. Penate, D. Lopez, J. San Juan, J. A. Carrasco *et al.*, "Fast optical source for quantum key distribution based on semiconductor optical amplifiers," *Optics express*, vol. 19, no. 5, pp. 3825–3834, 2011.

[77] X. Sun, M. A. Krainak, J. B. Abshire, J. D. Spinhirne, C. Trottier, M. Davies, H. Dautet, G. R. Allan, A. T.

Lukemire, and J. C. Vandiver, "Space-qualified silicon avalanche-photodiode single-photon-counting modules," *Journal of Modern Optics*, vol. 51, no. 9-10, pp. 1333–1350, Jun. 2004. [Online]. Available: http://www.tandfonline.com/doi/abs/10.1080/09500340408235276

[78] I. Prochazka, K. Hamal, and L. Kral, "Single photon counting module for space applications," *Journal of Modern Optics*, vol. 54, no. 2-3, pp. 151–161, Jan. 2007. [Online]. Available: http://dx.doi.org/10.1080/09500340600791756

[79] T. Jennewein, J. Bourgoin, B. Higgins, C. Holloway, E. Meyer-Scott, C. Erven, B. Heim, Z. Yan, H. Huebel, H.bel, G. Weihs *et al.*, "Qeyssat: a mission proposal for a quantum receiver in space," in *SPIE OPTO*. International Society for Optics and Photonics, 2014, pp. 89 970A–89 970A.

[80] W. Morong, A. Ling, and D. Oi, "Quantum optics for space platforms," *Optics and Photonics News*, vol. 23, no. 10, pp. 42–49, Oct. 2012. [Online]. Available: http://www.osa-opn.org/abstract.cfm?URI=opn-23-10-42

[81] D. Dehlinger and M. W. Mitchell, "Entangled photon apparatus for the undergraduate laboratory," *American Journal of Physics*, vol. 70, no. 9, pp. 898–902, 2002. [Online]. Available: http://scitation.aip.org/content/aapt/journal/ajp/70/9/10.1119/1.1498859

[82] V. Pruneri, J. Rarity, R. Ursin, T. Jennewein, P. Trojek, H. Weinfurter, H. Weier, A. Gardelein, M. Jofre, and J. Perdigues, "Entangled photon source for quantum communications (22542/09/nl/sfe) - tn 1," ESA/ESTEC, Technical Note 1, 2010.

[83] P. G. Kwiat, K. Mattle, H. Weinfurter, A. Zeilinger, A. V. Sergienko, and Y. Shih, "New high-intensity source of polarization-entangled photon pairs," *Phys. Rev. Lett.*, vol. 75, no. 24, pp. 4337–4341, Dec. 1995. [Online]. Available: http://link.aps.org/doi/10.1103/PhysRevLett.75.4337

[84] C. Law, I. Walmsley, and J. Eberly, "Continuous frequency entanglement: effective finite hilbert space and entropy control," *Physical review letters*, vol. 84, no. 23, p. 5304, 2000.

[85] A. Mair, A. Vaziri, G. Weihs, and A. Zeilinger, "Entanglement of the orbital angular momentum states of photons," *Nature*, vol. 412, no. 6844, pp. 313–316, Jul. 2001. [Online]. Available: http://www.nature.com/nature/journal/v412/n6844/abs/412313a0.html

[86] J. T. Barreiro, N. K. Langford, N. A. Peters, and P. G. Kwiat, "Generation of hyperentangled photon pairs," *Phys. Rev. Lett.*, vol. 95, no. 26, p. 260501, Dec. 2005. [Online]. Available: http://link.aps.org/doi/10.1103/PhysRevLett.95.260501

[87] J. Leach, B. Jack, J. Romero, A. K. Jha, A. M. Yao, S. Franke-Arnold, D. G. Ireland, R. W. Boyd, S. M. Barnett, and M. J. Padgett, "Quantum correlations in optical orbital angular momentum variables," *Science*, vol. 329, no. 5992, pp. 662–665, Aug. 2010. [Online]. Available: http://www.sciencemag.org/content/329/5992/662

[88] P. G. Kwiat, E. Waks, A. G. White, I. Appelbaum, and P. H. Eberhard, "Ultrabright source of polarization-entangled photons," *Phys. Rev. A*, vol. 60, no. 2, pp. R773–R776, Aug. 1999. [Online]. Available: http://link.aps.org/doi/10.1103/PhysRevA.60.R773

[89] P. Trojek and H. Weinfurter, "Collinear source of polarization-entangled photon pairs at nondegenerate wavelengths," *Appl. Phys. Lett.*, vol. 92, no. 21, p. 211103, 2008. [Online]. Available: http://link.aip.org/link/?APL/92/211103/1

[90] A. Fedrizzi, T. Herbst, A. Poppe, T. Jennewein, and A. Zeilinger, "A wavelength-tunable fiber-coupled source of narrowband entangled photons," *Opt. Express*, vol. 15, no. 23, pp. 15 377–15 386, 2007. [Online]. Available: http://www.opticsinfobase.org/abstract.cfm?URI=oe-15-23-15377

[91] D. Ljunggren, M. Tengner, P. Marsden, and M. Pelton, "Theory and experiment of entanglement in a quasi-phase-matched two-crystal source," *Phys. Rev. A*, vol. 73, no. 3, p. 032326, Mar. 2006. [Online]. Available: http://link.aps.org/doi/10.1103/PhysRevA.73.032326

[92] C. E. Kuklewicz, M. Fiorentino, G. Messin, F. N. C. Wong, and J. H. Shapiro, "High-flux source of polarization-entangled photons from a periodically poled $\mathrmKTiOPO_4$ parametric down-converter," *Phys. Rev. A*, vol. 69, no. 1, p. 013807, Jan. 2004. [Online]. Available: http://link.aps.org/doi/10.1103/PhysRevA.69.013807

[93] S. Tanzilli, H. De Riedmatten, H. Zbinden, P. Baldi, M. De Micheli, D. Ostrowsky, N. Gisin *et al.*, "Highly efficient photon-pair source using periodically poled lithium niobate waveguide," *Electronics Letters*, vol. 37, no. 1, pp. 26–28, 2001.

[94] M. Fiorentino, S. M. Spillane, R. G. Beausoleil, T. D. Roberts, P. Battle, and M. W. Munro, "Spontaneous parametric down-conversion in periodically poled KTP waveguides and bulk crystals," *Opt. Express*, vol. 15, no. 12, pp. 7479–7488, 2007. [Online]. Available: http://www.opticsinfobase.org/abstract.cfm?URI=oe-15-12-7479

[95] S. M. Spillane, M. Fiorentino, and R. G. Beausoleil, "Spontaneous parametric down conversion in a nanophotonic waveguide," *Opt. Express*, vol. 15, no. 14, pp. 8770–8780, Jul. 2007. [Online]. Available: http://www.opticsinfobase.org/abstract.cfm?URI=oe-15-14-8770

[96] M. Fiorentino and R. G. Beausoleil, "Compact sources of polarization-entangled photons," *Opt. Express*, vol. 16, no. 24, pp. 20 149–20 156, 2008. [Online]. Available: http://www.opticsexpress.org/abstract.cfm?URI=oe-16-24-20149

[97] A. Martin, A. Issautier, H. Herrmann, W. Sohler, D. B. Ostrowsky, O. Alibart, and S. Tanzilli, "A polarization entangled photon-pair source based on a type-II PPLN waveguide emitting at a telecom wavelength," *New J. Phys.*, vol. 12, no. 10, p. 103005, 2010. [Online]. Available: http://stacks.iop.org/1367-2630/12/i=10/a=103005

[98] S. Tanzilli, A. Martin, F. Kaiser, M. De Micheli, O. Alibart, and D. Ostrowsky, "On the genesis and evolution of integrated quantum optics," *Laser Photon. Rev.*, vol. 6, no. 1, pp. 115–143, 2012. [Online]. Available: http://dx.doi.org/10.1002/lpor.201100010

[99] H. Herrmann, X. Yang, A. Thomas, A. Poppe, W. Sohler, and C. Silberhorn, "Post-selection free, integrated optical source of non-degenerate, polarization entangled photon pairs," *Opt. Express*, vol. 21, no. 23, pp. 27 981–27 991, Nov 2013. [Online]. Available: http://www.opticsexpress.org/abstract.cfm?URI=oe-21-23-27981

[100] A. Vallés, M. Hendrych, J. Svozilík, R. Machulka, P. Abolghasem, D. Kang, B. J. Bijlani, A. S. Helmy, and J. P. Torres, "Generation of polarization-entangled photon pairs in a bragg reflection waveguide," *Opt. Express*, vol. 21, no. 9, pp. 10 841–10 849, May 2013. [Online]. Available: http://www.opticsexpress.org/abstract.cfm?URI=oe-21-9-10841

[101] A. McMillan, Y.-P. Huang, B. Bell, A. Clark, P. Kumar, and J. Rarity, "Chapter 12 - four-wave mixing in single-mode optical fibers," in *Experimental Methods in the Physical Sciences*, ser. Single-Photon Generation and Detection Physics and Applications, S. V. P. Alan Migdall, Jingyun Fan and Joshua C. Bienfang, Ed. Academic Press, 2013, vol. Volume 45, pp. 411–465. [Online]. Available: http://www.sciencedirect.com/science/article/pii/B9780123876959000123

[102] C. Liang, K. F. Lee, T. Levin, J. Chen, and P. Kumar, "Ultra stable all-fiber telecom-band entangled photon-pair source for turnkey quantum communication applications," *Optics express*, vol. 14, no. 15, pp. 6936–6941, 2006.

[103] C. Liang, K. F. Lee, M. Medic, P. Kumar, R. H. Hadfield, and S. W. Nam, "Characterization of fiber-generated entangled photon pairs with superconducting single-photon detectors," *Optics express*, vol. 15, no. 3, pp. 1322–1327, 2007.

[104] B. J. Smith, P. Mahou, O. Cohen, J. Lundeen, and I. Walmsley, "Photon pair generation in birefringent optical fibers," *Optics express*, vol. 17, no. 26, pp. 23 589–23 602, 2009.

[105] A. R. McMillan, J. Fulconis, M. Halder, C. Xiong, J. Rarity, and W. J. Wadsworth, "Narrowband high-fidelity all-fibre source of heralded single photons at 1570 nm," *Optics express*, vol. 17, no. 8, pp. 6156–6165, 2009.

[106] H. Takesue and K. Inoue, "Generation of polarization-entangled photon pairs and violation of bell's inequality using spontaneous four-wave mixing in a fiber loop," *Physical Review A*, vol. 70, no. 3, p. 031802, 2004.

[107] J. Fulconis, O. Alibart, W. Wadsworth, P. Russell, and J. Rarity, "High brightness single mode source of correlated photon pairs using a photonic crystal fiber," *Optics Express*, vol. 13, no. 19, pp. 7572–7582, Sep. 2005. [Online]. Available: http://www.opticsexpress.org/abstract.cfm?URI=oe-13-19-7572

[108] J. G. Rarity, J. Fulconis, J. Duligall, W. J. Wadsworth, and P. S. J. Russell, "Photonic crystal fiber source of correlated photon pairs," *Optics Express*, vol. 13, no. 2, p. 534, 2005. [Online]. Available: http://www.opticsexpress.org/abstract.cfm?URI=OPEX-13-2-534

[109] J. Fulconis, O. Alibart, J. L. O'Brien, W. J. Wadsworth, and J. G. Rarity, "Nonclassical interference and entanglement generation using a photonic crystal fiber pair photon source," *Phys. Rev. Lett.*, vol. 99, no. 12, p. 120501, Sep. 2007. [Online]. Available: http://link.aps.org/doi/10.1103/PhysRevLett.99.120501

[110] A. Clark, B. Bell, J. Fulconis, M. M. Halder, B. Cemlyn, O. Alibart, C. Xiong, W. J. Wadsworth, and J. G. Rarity, "Intrinsically narrowband pair photon generation in microstructured fibres," *New Journal of Physics*, vol. 13, no. 6, p. 065009, 2011.

[111] J. E. Sharping, K. F. Lee, M. A. Foster, A. C. Turner, B. S. Schmidt, M. Lipson, A. L. Gaeta, and P. Kumar, "Generation of correlated photons in nanoscale silicon waveguides," *Opt. Express*, vol. 14, no. 25, pp. 12 388–12 393, Dec 2006. [Online]. Available: http://www.opticsexpress.org/abstract.cfm?URI=oe-14-25-12388

[112] H. Takesue, H. Fukuda, T. Tsuchizawa, T. Watanabe, K. Yamada, Y. Tokura, and S.-i. Itabashi, "Generation of polarization entangled photon pairs using silicon wire waveguide," *Optics express*, vol. 16, no. 8, pp. 5721–5727, 2008.

[113] N. Matsuda, H. Le Jeannic, H. Fukuda, T. Tsuchizawa, W. J. Munro, K. Shimizu, K. Yamada, Y. Tokura, and H. Takesue, "A monolithically inte-

grated polarization entangled photon pair source on a silicon chip," *Scientific reports*, vol. 2, 2012.

[114] J. Silverstone, D. Bonneau, K. Ohira, N. Suzuki, H. Yoshida, N. Iizuka, M. Ezaki, C. Natarajan, M. Tanner, R. Hadfield *et al.*, "On-chip quantum interference between silicon photon-pair sources," *Nature Photonics*, vol. 8, no. 2, pp. 104–108, 2014.

[115] X. Li, P. L. Voss, J. E. Sharping, and P. Kumar, "Optical-fiber source of polarization-entangled photons in the 1550 nm telecom band," *Physical Review Letters*, vol. 94, no. 5, p. 053601, 2005.

[116] M. Medic, J. B. Altepeter, M. A. Hall, Monika Patel, and P. Kumar, "Fiber-based telecommunication-band source of degenerate entangled photons," *Opt. Lett.*, vol. 35, no. 6, pp. 802–804, Mar. 2010. [Online]. Available: http://ol.osa.org/abstract.cfm?URI=ol-35-6-802

[117] P. Michler, A. Kiraz, C. Becher, W. V. Schoenfeld, P. M. Petroff, L. Zhang, E. Hu, and A. Imamoglu, "A quantum dot single-photon turnstile device," *Science*, vol. 290, no. 5500, pp. 2282–2285, 2000. [Online]. Available: http://www.sciencemag.org/content/290/5500/2282.abstract

[118] A. J. Shields, "Semiconductor quantum light sources," *Nature photonics*, vol. 1, no. 4, pp. 215–223, 2007.

[119] R. J. Young, R. M. Stevenson, P. Atkinson, K. Cooper, D. A. Ritchie, and A. J. Shields, "Improved fidelity of triggered entangled photons from single quantum dots," *New Journal of Physics*, vol. 8, no. 2, p. 29, 2006.

[120] A. Dousse, J. Suffczyński, A. Beveratos, O. Krebs, A. Lemaître, I. Sagnes, J. Bloch, P. Voisin, and P. Senellart, "Ultrabright source of entangled photon pairs," *Nature*, vol. 466, no. 7303, pp. 217–220, 2010.

[121] M. Ghioni, G. Armellini, P. Maccagnani, I. Rech, M. K. Emsley, and M. S. Unlu, "Resonant-cavity-enhanced single photon avalanche diodes on double silicon-on-insulator substrates," *Journal of Modern Optics*, vol. 56, no. 2-3, pp. 309–316, 2009. [Online]. Available: http://dx.doi.org/10.1080/09500340802272332

[122] K. Irwin and G. Hilton, "Transition-edge sensors," in *Cryogenic Particle Detection*, ser. Topics in Applied Physics, C. Enss, Ed. Springer Berlin Heidelberg, 2005, vol. 99, pp. 63–150. [Online]. Available: http://dx.doi.org/10.1007/10933596_3

[123] A. J. Miller, S. W. Nam, J. M. Martinis, and A. V. Sergienko, "Demonstration of a low-noise near-infrared photon

counter with multiphoton discrimination," *Applied Physics Letters*, vol. 83, no. 4, pp. 791–793, 2003. [Online]. Available: http://scitation.aip.org/content/aip/journal/apl/83/4/10.1063/1.1596723

[124] A. E. Lita, A. J. Miller, and S. W. Nam, "Counting near-infrared single-photons with 95% efficiency," *Opt. Express*, vol. 16, no. 5, pp. 3032–3040, Mar 2008. [Online]. Available: http://www.opticsexpress.org/abstract.cfm?URI=oe-16-5-3032

[125] T. Gerrits, N. Thomas-Peter, J. C. Gates, A. E. Lita, B. J. Metcalf, B. Calkins, N. A. Tomlin, A. E. Fox, A. L. Linares, J. B. Spring, N. K. Langford, R. P. Mirin, P. G. R. Smith, I. A. Walmsley, and S. W. Nam, "On-chip, photon-number-resolving, telecommunication-band detectors for scalable photonic information processing," *Phys. Rev. A*, vol. 84, p. 060301, Dec 2011. [Online]. Available: http://link.aps.org/doi/10.1103/PhysRevA.84.060301

[126] B. Calkins, P. L. Mennea, A. E. Lita, B. J. Metcalf, W. S. Kolthammer, A. Lamas-Linares, J. B. Spring, P. C. Humphreys, R. P. Mirin, J. C. Gates, P. G. R. Smith, I. A. Walmsley, T. Gerrits, and S. W. Nam, "High quantum-efficiency photon-number-resolving detector for photonic on-chip information processing," *Opt. Express*, vol. 21, no. 19, pp. 22 657–22 670, Sep 2013. [Online]. Available: http://www.opticsexpress.org/abstract.cfm?URI=oe-21-19-22657

[127] K. M. Rosfjord, J. K. W. Yang, E. A. Dauler, A. J. Kerman, V. Anant, B. M. Voronov, G. N. Gol'tsman, and K. K. Berggren, "Nanowire single-photon detector with an integrated optical cavity and anti-reflection coating," *Opt. Express*, vol. 14, no. 2, pp. 527–534, Jan 2006. [Online]. Available: http://www.opticsexpress.org/abstract.cfm?URI=oe-14-2-527

[128] A. Divochiy, F. Marsili, D. Bitauld, A. Gaggero, R. Leoni, F. Mattioli, A. Korneev, V. Seleznev, N. Kaurova, O. Minaeva *et al.*, "Superconducting nanowire photon-number-resolving detector at telecommunication wavelengths," *Nature Photonics*, vol. 2, no. 5, pp. 302–306, 2008.

[129] F. Marsili, D. Bitauld, A. Gaggero, S. Jahanmirinejad, R. Leoni, F. Mattioli, and A. Fiore, "Physics and application of photon number resolving detectors based on superconducting parallel nanowires," *New Journal of Physics*, vol. 11, no. 4, p. 045022, 2009.

[130] J. Sprengers, A. Gaggero, D. Sahin, S. Jahanmirinejad, G. Frucci, F. Mattioli, R. Leoni, J. Beetz, M. Lermer, M. Kamp *et al.*, "Waveguide superconducting single-photon detectors for integrated quantum photonic circuits," *Applied Physics Letters*, vol. 99, no. 18, p. 181110, 2011.

[131] C. M. Natarajan, M. G. Tanner, and R. H. Hadfield, "Superconducting nanowire single-photon detectors: physics and applications," *Superconductor Science and Technology*, vol. 25, no. 6, p. 063001, 2012. [Online]. Available: http://stacks.iop.org/0953-2048/25/i=6/a=063001

[132] V. Pruneri, J. Rarity, R. Ursin, and F. Steinlechner, "Entangled photon source for quantum communications (22542/09/nl/sfe) - summary report," ESA/ESTEC, Summary Report, 2012.

[133] R. J. Glauber, *Quantum theory of optical coherence: selected papers and lectures*. John Wiley & Sons, 2007.

[134] H.-A. Bachor and T. C. Ralph, "A guide to experiments in quantum optics, 2nd," *A Guide to Experiments in Quantum Optics, 2nd, Revised and Enlarged Edition, by Hans-A. Bachor, Timothy C. Ralph, pp. 434. ISBN 3-527-40393-0. Wiley-VCH, March 2004.*, vol. 1, 2004.

[135] L. Mandel and E. Wolf, *Optical coherence and quantum optics*. Cambridge university press, 1995.

[136] C. Gerry and P. Knight, *Introductory quantum optics*. Cambridge university press, 2005.

[137] M. Fox, *Quantum Optics: An Introduction: An Introduction*. Oxford university press, 2006, vol. 6.

[138] D. F. Walls and G. J. Milburn, *Quantum optics*. Springer Science & Business Media, 2007.

[139] I. Marcikic, H. de Riedmatten, W. Tittel, V. Scarani, H. Zbinden, and N. Gisin, "Time-bin entangled qubits for quantum communication created by femtosecond pulses," *Phys. Rev. A*, vol. 66, p. 062308, Dec 2002. [Online]. Available: http://link.aps.org/doi/10.1103/PhysRevA.66.062308

[140] I. Marcikic, H. de Riedmatten, W. Tittel, H. Zbinden, M. Legré, and N. Gisin, "Distribution of time-bin entangled qubits over 50 km of optical fiber," *Phys. Rev. Lett.*, vol. 93, p. 180502, Oct 2004. [Online]. Available: http://link.aps.org/doi/10.1103/PhysRevLett.93.180502

[141] T. Honjo, H. Takesue, H. Kamada, Y. Nishida, O. Tadanaga, M. Asobe, and K. Inoue, "Long-distance distribution of time-bin entangled photon pairs over 100 km using frequency up-conversion detectors," *Opt. Express*, vol. 15, no. 21, pp. 13 957–13 964, Oct 2007. [Online]. Available: http://www.opticsexpress.org/abstract.cfm?URI=oe-15-21-13957

[142] A. Martin, F. Kaiser, A. Vernier, A. Beveratos, V. Scarani, and S. Tanzilli, "Cross time-bin photonic entanglement for quantum key distribution," *Phys. Rev. A*, vol. 87, p. 020301, Feb 2013. [Online]. Available: http://link.aps.org/doi/10.1103/PhysRevA.87.020301

[143] J. M. Donohue, M. Agnew, J. Lavoie, and K. J. Resch, "Coherent ultrafast measurement of time-bin encoded photons," *Phys. Rev. Lett.*, vol. 111, p. 153602, Oct 2013. [Online]. Available: http://link.aps.org/doi/10.1103/PhysRevLett.111.153602

[144] O. Kwon, K.-K. Park, Y.-S. Ra, Y.-S. Kim, and Y.-H. Kim, "Time-bin entangled photon pairs from spontaneous parametric down-conversion pumped by a cw multi-mode diode laser," *Opt. Express*, vol. 21, no. 21, pp. 25 492–25 500, Oct. 2013. [Online]. Available: http://www.opticsexpress.org/abstract.cfm?URI=oe-21-21-25492

[145] H. Hübel, M. R. Vanner, T. Lederer, B. Blauensteiner, T. Lorünser, A. Poppe, and A. Zeilinger, "High-fidelity transmission of polarization encoded qubits from an entangled source over 100 km of fiber," *Opt. Express*, vol. 15, no. 12, pp. 7853–7862, Jun 2007. [Online]. Available: http://www.opticsexpress.org/abstract.cfm?URI=oe-15-12-7853

[146] C. H. Bennett, G. Brassard, and others, "Quantum cryptography: Public key distribution and coin tossing," in *Proceedings of IEEE International Conference on Computers, Systems and Signal Processing*, vol. 175. New York, 1984.

[147] D. Bohm and Y. Aharonov, "Discussion of experimental proof for the paradox of einstein, rosen, and podolsky," *Physical Review*, vol. 108, no. 4, p. 1070, 1957.

[148] J. Bell and others, "Speakable and unspeakable in quantum mechanics," *Speakable and Unspeakable in Quantum Mechanics, by JS Bell, Introduction by Alain Aspect, Cambridge, UK: Cambridge University Press, 2004*, vol. 1, 2004.

[149] B. G. Christensen, K. T. McCusker, J. B. Altepeter, B. Calkins, T. Gerrits, A. E. Lita, A. Miller, L. K. Shalm, Y. Zhang, S. W. Nam, N. Brunner, C. C. W. Lim, N. Gisin, and P. G. Kwiat, "Detection-loophole-free test of quantum nonlocality, and applications," *Phys. Rev. Lett.*, vol. 111, p. 130406, Sep 2013. [Online]. Available: http://link.aps.org/doi/10.1103/PhysRevLett.111.130406

[150] T. Scheidl, "A fundamental test and an application of quantum entanglement," Ph.D. dissertation, University of Vienna, 2009.

[151] O. Guehne and G. Toth, "Entanglement detection," *Phys. Rep.*, vol. 474, no. 1-6, pp. 1 – 75, 2009. [Online]. Available: http://www.sciencedirect.com/science/article/pii/S0370157309000623

[152] J. B. Altepeter, E. R. Jeffrey, and P. G. Kwiat, "Photonic state tomography," *Advances in Atomic, Molecular, and Optical Physics*, vol. 52, pp. 105–159, 2005.

[153] D. F. James, P. G. Kwiat, W. J. Munro, and A. G. White, "Measurement of qubits," *Physical Review A*, vol. 64, no. 5, p. 052312, 2001.

[154] T. Jennewein, R. Ursin, M. Aspelmeyer, and A. Zeilinger, "Performing high-quality multi-photon experiments with parametric down-conversion," *Journal of Physics B: Atomic, Molecular and Optical Physics*, vol. 42, no. 11, p. 114008, 2009. [Online]. Available: http://stacks.iop.org/0953-4075/42/i=11/a=114008

[155] A. K. Ekert, "Quantum cryptography based on bell's theorem," *Physical Review Letters*, vol. 67, no. 6, pp. 661–663, Aug. 1991. [Online]. Available: http://link.aps.org/doi/10.1103/PhysRevLett.67.661

[156] C. H. Bennett, G. Brassard, and N. D. Mermin, "Quantum cryptography without bell's theorem," *Physical Review Letters*, vol. 68, no. 5, pp. 557–559, Feb. 1992. [Online]. Available: http://link.aps.org/doi/10.1103/PhysRevLett.68.557

[157] H.-K. Lo and N. Lütkenhaus, "Quantum cryptography: from theory to practice," *arXiv preprint quant-ph/0702202*, 2007.

[158] N. Lütkenhaus and A. J. Shields, "Focus on quantum cryptography: Theory and practice," *New Journal of Physics*, vol. 11, no. 4, p. 045005, 2009. [Online]. Available: http://stacks.iop.org/1367-2630/11/i=4/a=045005

[159] E. Waks, A. Zeevi, and Y. Yamamoto, "Security of quantum key distribution with entangled photons against individual attacks," *Physical Review A*, vol. 65, no. 5, p. 052310, Apr. 2002. [Online]. Available: http://link.aps.org/doi/10.1103/PhysRevA.65.052310

[160] X. Ma, C.-H. F. Fung, and H.-K. Lo, "Quantum key distribution with entangled photon sources," *Physical Review A*, vol. 76, no. 1, p. 012307, Jul. 2007. [Online]. Available: http://link.aps.org/doi/10.1103/PhysRevA.76.012307

[161] C. Holloway, J. A. Doucette, C. Erven, J.-P. Bourgoin, and T. Jennewein, "Optimal pair-generation rate for entanglement-based quantum key distribution," *Physical Review A*, vol. 87, no. 2, p. 022342, Feb. 2013. [Online]. Available: http://link.aps.org/doi/10.1103/PhysRevA.87.022342

[162] J. P. Torres, K. Banaszek, and I. A. Walmsley, "Chapter 5 - engineering nonlinear optic sources of photonic entanglement," in *Progress in Optics*, ser. Progress in Optics, E. Wolf, Ed. Elsevier, 2011, vol. 56, pp. 227 – 331. [Online]. Available: http://www.sciencedirect.com/science/article/pii/B9780444538864000058

[163] Z.-Y. J. Ou, *Multi-photon quantum interference*. Springer, 2007.

[164] R. J. Glauber, "Coherent and incoherent states of the radiation field," *Phys. Rev.*, vol. 131, pp. 2766–2788, Sep 1963. [Online]. Available: http://link.aps.org/doi/10.1103/PhysRev.131.2766

[165] P. Kok and S. L. Braunstein, "Limitations on the creation of maximal entanglement," *Physical Review A*, vol. 62, no. 6, p. 064301, Nov. 2000. [Online]. Available: http://link.aps.org/doi/10.1103/PhysRevA.62.064301

[166] ——, "Postselected versus nonpostselected quantum teleportation using parametric down-conversion," *Physical Review A*, vol. 61, no. 4, p. 042304, Mar. 2000. [Online]. Available: http://link.aps.org/doi/10.1103/PhysRevA.61.042304

[167] P. Walther, M. Aspelmeyer, and A. Zeilinger, "Heralded generation of multiphoton entanglement," *Physical Review A*, vol. 75, no. 1, p. 012313, 2007.

[168] C. Śliwa and K. Banaszek, "Conditional preparation of maximal polarization entanglement," *Physical Review A*, vol. 67, no. 3, p. 030101, Mar. 2003. [Online]. Available: http://link.aps.org/doi/10.1103/PhysRevA.67.030101

[169] S. Barz, G. Cronenberg, A. Zeilinger, and P. Walther, "Heralded generation of entangled photon pairs," *Nature Photonics*, vol. 4, no. 8, pp. 553–556, Aug. 2010. [Online]. Available: http://www.nature.com/nphoton/journal/v4/n8/abs/nphoton.2010.156.html

[170] H. Hübel, D. R. Hamel, A. Fedrizzi, S. Ramelow, K. J. Resch, and T. Jennewein, "Direct generation of photon triplets using cascaded photon-pair sources," *Nature*, vol. 466, no. 7306, pp. 601–603, Jul. 2010. [Online]. Available: http://www.nature.com/nature/journal/v466/n7306/abs/nature09175.html

[171] D. R. Hamel, L. K. Shalm, H. Hübel, A. J. Miller, F. Marsili, V. B. Verma, R. P. Mirin, S. W. Nam, K. J. Resch, and T. Jennewein, "Direct generation of three-photon polarization entanglement," *Nature Photonics*, vol. 8, no. 10, pp. 801–807, 2014.

[172] C. K. Hong, Z. Y. Ou, and L. Mandel, "Measurement of subpicosecond time intervals between two photons by interference," *Physical Review Letters*, vol. 59, no. 18, pp. 2044–2046, Nov. 1987. [Online]. Available: http://link.aps.org/doi/10.1103/PhysRevLett.59.2044

[173] P. Trojek, "Efficient generation of photonic entanglement and multiparty quantum communication," Ph.D. dissertation, LMU-Munich, 2007.

[174] T. Kim, M. Fiorentino, and F. N. C. Wong, "Phase-stable source of polarization-entangled photons using a polarization sagnac interferometer," *Phys. Rev. A*, vol. 73, no. 1, p. 012316, Jan. 2006. [Online]. Available: http://link.aps.org/doi/10.1103/PhysRevA.73.012316

[175] P. G. Kwiat, "Hyper-entangled states," *Journal of Modern Optics*, vol. 44, no. 11-12, pp. 2173–2184, 1997. [Online]. Available: http://www.tandfonline.com/doi/abs/10.1080/09500349708231877

[176] C. Wang, F.-G. Deng, Y.-S. Li, X.-S. Liu, and G. L. Long, "Quantum secure direct communication with high-dimension quantum superdense coding," *Phys. Rev. A*, vol. 71, p. 044305, Apr 2005. [Online]. Available: http://link.aps.org/doi/10.1103/PhysRevA.71.044305

[177] J.-W. Pan, Z.-B. Chen, C.-Y. Lu, H. Weinfurter, A. Zeilinger, and M. Å»ukowski, "Multiphoton entanglement and interferometry," *Reviews of Modern Physics*, vol. 84, no. 2, pp. 777–838, May 2012. [Online]. Available: http://link.aps.org/doi/10.1103/RevModPhys.84.777

[178] P. R. Tapster and J. G. Rarity, "Photon statistics of pulsed parametric light," *Journal of Modern Optics*, vol. 45, no. 3, pp. 595–604, 1998. [Online]. Available: http://dx.doi.org/10.1080/09500349808231917

[179] H. D. Riedmatten, V. Scarani, I. Marcikic, A. AcÃn, W. Tittel, H. Zbinden, and N. Gisin, "Two independent photon pairs versus four-photon entangled states in parametric down conversion," *Journal of Modern Optics*, vol. 51, no. 11, pp. 1637–1649, 2004. [Online]. Available: http://www.tandfonline.com/doi/abs/10.1080/09500340408232478

[180] W. Grice, R. Bennink, P. Evans, T. Humble, and J. Schaake, "Auxiliary entanglement in photon pairs for multi-photon entanglement," *Journal of Modern Optics*, vol. 59, no. 17, pp. 1538–1545, 2012. [Online]. Available: http://www.tandfonline.com/doi/abs/10.1080/09500340.2012.705342

[181] V. Scarani, H. de Riedmatten, I. Marcikic, H. Zbinden, and N. Gisin, "Four-photon correction in two-photon bell experiments," *The European Physical Journal D - Atomic, Molecular, Optical and Plasma Physics*, vol. 32, no. 1, pp. 129–138, 2005. [Online]. Available: http://dx.doi.org/10.1140/epjd/e2004-00170-7

[182] H. Takesue and K. Shimizu, "Effects of multiple pairs on visibility measurements of entangled photons generated by spontaneous parametric processes," *Optics Communications*, vol. 283, no. 2, pp. 276 – 287, 2010. [Online]. Available: http://www.sciencedirect.com/science/article/pii/S0030401809009651

[183] T. Jennewein, M. Barbieri, and A. G. White, "Single-photon device requirements for operating linear optics quantum computing outside the post-selection basis," *Journal of Modern Optics*, vol. 58, no. 3-4, pp. 276–287, 2011. [Online]. Available: http://www.tandfonline.com/doi/abs/10.1080/09500340.2010.546894

[184] S. Ramelow, A. Mech, M. Giustina, S. GrÃ¶blacher, W. Wieczorek, J. Beyer, A. Lita, Brice Calkins, T. Gerrits, S. W. Nam, A. Zeilinger, and R. Ursin, "Highly efficient heralding of entangled single photons," *Opt. Express*, vol. 21, no. 6, pp. 6707–6717, Mar. 2013. [Online]. Available: http://www.opticsexpress.org/abstract.cfm?URI=oe-21-6-6707

[185] S. Gaertner, M. Bourennane, M. Eibl, C. Kurtsiefer, and H. Weinfurter, "High-fidelity source of four-photon entanglement," *Applied Physics B*, vol. 77, no. 8, pp. 803–807, 2003.

[186] Z. Zhao, Y.-A. Chen, A.-N. Zhang, T. Yang, H. J. Briegel, and J.-W. Pan, "Experimental demonstration of five-photon entanglement and open-destination teleportation," *Nature*, vol. 430, no. 6995, pp. 54–58, 2004.

[187] Y.-F. Huang, B.-H. Liu, L. Peng, Y.-H. Li, L. Li, C.-F. Li, and G.-C. Guo, "Experimental generation of an eight-photon greenberger–horne–zeilinger state," *Nature communications*, vol. 2, p. 546, 2011.

[188] T. Scheidl, F. Tiefenbacher, R. Prevedel, F. Steinlechner, R. Ursin, and A. Zeilinger, "Crossed-crystal scheme for femtosecond-pulsed entangled photon generation in periodically poled potassium titanyl phosphate," *Physical Review A*, vol. 89, no. 4, p. 042324, Apr. 2014. [Online]. Available: http://link.aps.org/doi/10.1103/PhysRevA.89.042324

[189] B. Kardynał, Z. Yuan, and A. Shields, "An avalanche-photodiode-based photon-number-resolving detector," *nature photonics*, vol. 2, no. 7, pp. 425–428, 2008.

[190] A. L. Migdall, D. Branning, and S. Castelletto, "Tailoring single-photon and multiphoton probabilities of a single-photon on-demand source," *Phys. Rev. A*, vol. 66, p. 053805, Nov 2002. [Online]. Available: http://link.aps.org/doi/10.1103/PhysRevA.66.053805

[191] M. A. Broome, M. P. Almeida, A. Fedrizzi, and A. G. White, "Reducing multi-photon rates in pulsed down-conversion by temporal multiplexing," *Opt. Express*, vol. 19, no. 23, pp. 22 698–22 708, Nov 2011. [Online]. Available: http://www.opticsexpress.org/abstract.cfm?URI=oe-19-23-22698

[192] A. Christ, A. Fedrizzi, H. HÃ$\frac{1}{4}$bel, T. Jennewein, and C. Silberhorn, "Chapter 11 - parametric down-conversion," in *Experimental Methods in the Physical Sciences*, ser. Single-Photon Generation and Detection Physics and Applications, S. V. P. Alan Migdall, Jingyun Fan and Joshua C. Bienfang, Ed. Academic Press, 2013, vol. Volume 45, pp. 351–410. [Online]. Available: http://www.sciencedirect.com/science/article/pii/B9780123876959000111

[193] S. Arahira and H. Murai, "Nearly degenerate wavelength-multiplexed polarization entanglement by cascaded optical nonlinearities in a PPLN ridge waveguide device," *Optics Express*,

vol. 21, no. 6, pp. 7841–7850, 2013. [Online]. Available: http://www.opticsexpress.org/abstract.cfm?URI=oe-21-6-7841

[194] M. N. Satyanarayan, A. Deepthy, and H. L. Bhat, "Potassium titanyl phosphate and its isomorphs: Growth, properties, and applications," *Crit. Rev. Solid State Mater. Sci.*, vol. 24, no. 2, pp. 103–191, 1999. [Online]. Available: http://www.tandfonline.com/doi/abs/10.1080/10408439991329189

[195] D. A. Roberts, "Simplified characterization of uniaxial and biaxial nonlinear optical crystals: a plea for standardization of nomenclature and conventions," *Quantum Electronics, IEEE Journal of*, vol. 28, no. 10, pp. 2057–2074, 1992.

[196] R. Boyd, *Nonlinear optics*. Acad. Press, Jan. 2003. [Online]. Available: http://www.osti.gov/scitech/servlets/purl/5321594

[197] B. E. A. Saleh and M. C. Teich, "Nonlinear optics," in *Fundamentals of Photonics*. John Wiley & Sons, Inc., 2001, pp. 737–798. [Online]. Available: http://dx.doi.org/10.1002/0471213748.ch19

[198] D. S. Hum and M. M. Fejer, "Quasi-phasematching," *Comptes Rendus Physique*, vol. 8, no. 2, pp. 180–198, Mar. 2007. [Online]. Available: http://www.sciencedirect.com/science/article/pii/S1631070506002349

[199] V. Pruneri, A. Gardelein, M. Jofre, J. Perdigues, L. Penate, E. Wille, E. Bernabeu, D. Lopez, and R. Ursin, "Quantum transceiver for secure global communications (contract number 21460/08/nl/ia)," ESA/ESTEC, Tech. Rep., 2015.

[200] R. C. Pooser and O. Pfister, "Observation of triply coincident nonlinearities in periodically poled KTiOPO4," *Optics Letters*, vol. 30, no. 19, pp. 2635–2637, Oct. 2005. [Online]. Available: http://ol.osa.org/abstract.cfm?URI=ol-30-19-2635

[201] S. Lerch, B. Bessire, C. Bernhard, Thomas Feurer, and A. Stefanov, "Tuning curve of type-0 spontaneous parametric down-conversion," *J. Opt. Soc. Am. B*, vol. 30, no. 4, pp. 953–958, Apr. 2013. [Online]. Available: http://josab.osa.org/abstract.cfm?URI=josab-30-4-953

[202] S.-Y. Baek and Y.-H. Kim, "Spectral properties of entangled photons generated via type-i frequency-nondegenerate spontaneous parametric down-conversion," *Phys. Rev. A*, vol. 80, no. 3, p. 033814, Sep. 2009. [Online]. Available: http://link.aps.org/doi/10.1103/PhysRevA.80.033814

[203] W. P. Grice and I. A. Walmsley, "Spectral information and distinguishability in type-II down-conversion with a broadband pump," *Phys. Rev. A*, vol. 56, no. 2, pp. 1627–1634, Aug. 1997. [Online]. Available: http://link.aps.org/doi/10.1103/PhysRevA.56.1627

[204] Y.-H. Kim and W. P. Grice, "Measurement of the spectral properties of the two-photon state generated via type II spontaneous parametric downconversion," *Opt. Lett.*, vol. 30, no. 8, pp. 908–910, Apr. 2005. [Online]. Available: http://ol.osa.org/abstract.cfm?URI=ol-30-8-908

[205] H. Vanherzeele and J. D. Bierlein, "Magnitude of the nonlinear-optical coefficients of KTiOPO4," *Opt. Lett.*, vol. 17, no. 14, pp. 982–984, Jul. 1992. [Online]. Available: http://ol.osa.org/abstract.cfm?URI=ol-17-14-982

[206] M. V. Pack, D. J. Armstrong, and A. V. Smith, "Measurement of the $\chi(2)$ tensors of KTiOPO4, KTiOAsO4, RbTiOPO4, and RbTiOAsO4 crystals," *Appl. Opt.*, vol. 43, no. 16, pp. 3319–3323, Jun. 2004. [Online]. Available: http://ao.osa.org/abstract.cfm?URI=ao-43-16-3319

[207] T. Y. Fan, C. E. Huang, B. Q. Hu, R. C. Eckardt, Y. X. Fan, R. L. Byer, and R. S. Feigelson, "Second harmonic generation and accurate index of refraction measurements in flux-grown KTiOPO4," *Appl. Opt.*, vol. 26, no. 12, pp. 2390–2394, Jun. 1987. [Online]. Available: http://ao.osa.org/abstract.cfm?URI=ao-26-12-2390

[208] K. Kato and E. Takaoka, "Sellmeier and thermo-optic dispersion formulas for KTP," *Applied Optics*, vol. 41, no. 24, pp. 5040–5044, Aug. 2002. [Online]. Available: http://ao.osa.org/abstract.cfm?URI=ao-41-24-5040

[209] W. H. Peeters and M. P. van Exter, "Optical characterization of periodically-poled KTiOPO4," *Optics Express*, vol. 16, no. 10, pp. 7344–7360, May 2008. [Online]. Available: http://www.opticsexpress.org/abstract.cfm?URI=oe-16-10-7344

[210] W. Wiechmann, S. Kubota, T. Fukui, and H. Masuda, "Refractive-index temperature derivatives of potassium titanyl phosphate," *Opt. Lett.*, vol. 18, no. 15, pp. 1208–1210, Aug. 1993. [Online]. Available: http://ol.osa.org/abstract.cfm?URI=ol-18-15-1208

[211] S. Emanueli and A. Arie, "Temperature-dependent dispersion equations for KTiOPO4 and KTiOAsO4," *Appl. Opt.*, vol. 42, no. 33, pp. 6661–6665, Nov. 2003. [Online]. Available: http://ao.osa.org/abstract.cfm?URI=ao-42-33-6661

[212] K. Fradkin, A. Arie, A. Skliar, and G. Rosenman, "Tunable midinfrared source by difference frequency generation in bulk periodically poled KTiOPO4," *Applied Physics Letters*, vol. 74, no. 7, pp. 914–916, Feb. 1999. [Online]. Available: http://scitation.aip.org/content/aip/journal/apl/74/7/10.1063/1.123408

[213] F. Pignatiello, M. De Rosa, P. Ferraro, S. Grilli, P. De Natale, A. Arie, and S. De Nicola, "Measurement of the thermal expansion

coefficients of ferroelectric crystals by a moirÃ© interferometer," *Optics Communications*, vol. 277, no. 1, pp. 14–18, Sep. 2007. [Online]. Available: http://www.sciencedirect.com/science/article/pii/S0030401807004506

[214] B. Dayan, A. Pe'er, A. A. Friesem, and Y. Silberberg, "Nonlinear interactions with an ultrahigh flux of broadband entangled photons," *Phys. Rev. Lett.*, vol. 94, no. 4, p. 043602, Feb. 2005. [Online]. Available: http://link.aps.org/doi/10.1103/PhysRevLett.94.043602

[215] M. B. Nasr, S. Carrasco, B. E. A. Saleh, A. V. Sergienko, M. C. Teich, J. P. Torres, L. Torner, D. S. Hum, and M. M. Fejer, "Ultrabroadband biphotons generated via chirped quasi-phase-matched optical parametric down-conversion," *Phys. Rev. Lett.*, vol. 100, no. 18, p. 183601, May 2008. [Online]. Available: http://link.aps.org/doi/10.1103/PhysRevLett.100.183601

[216] A. F. Abouraddy, B. E. A. Saleh, A. V. Sergienko, and M. C. Teich, "Entangled-photon fourier optics," *Journal of the Optical Society of America B*, vol. 19, no. 5, pp. 1174–1184, May 2002. [Online]. Available: http://josab.osa.org/abstract.cfm?URI=josab-19-5-1174

[217] M. B. Nasr, B. E. A. Saleh, A. V. Sergienko, and M. C. Teich, "Demonstration of dispersion-canceled quantum-optical coherence tomography," *Phys. Rev. Lett.*, vol. 91, no. 8, p. 083601, Aug. 2003. [Online]. Available: http://link.aps.org/doi/10.1103/PhysRevLett.91.083601

[218] A. Valencia, G. Scarcelli, and Y. Shih, "Distant clock synchronization using entangled photon pairs," *Appl. Phys. Lett.*, vol. 85, no. 13, pp. 2655 –2657, Sep. 2004.

[219] S. Ramelow and R. Lapkiewicz, 2013, published: private communication.

[220] F. Steinlechner, S. Ramelow, M. Jofre, M. Gilaberte, T. Jennewein, J. P. Torres, M. W. Mitchell, and V. Pruneri, "Phase-stable source of polarization-entangled photons in a linear double-pass configuration," *Optics express*, vol. 21, no. 10, pp. 11 943–11 951, 2013.

[221] O. Kwon, Y.-S. Ra, and Y.-H. Kim, "Coherence properties of spontaneous parametric down-conversion pumped by a multi-mode cw diode laser," *Optics Express*, vol. 17, no. 15, pp. 13 059–13 069, Jul. 2009. [Online]. Available: http://www.opticsexpress.org/abstract.cfm?URI=oe-17-15-13059

[222] C. Kurtsiefer, M. Oberparleiter, and H. Weinfurter, "High-efficiency entangled photon pair collection in type-II parametric fluorescence," *Phys. Rev. A*, vol. 64, no. 2, p. 023802, Jul. 2001. [Online]. Available: http://link.aps.org/doi/10.1103/PhysRevA.64.023802

[223] F. A. Bovino, P. Varisco, A. M. Colla, G. Castagnoli, G. D. Giuseppe, and A. V. Sergienko, "Effective fiber-coupling of entangled photons for quantum communication," *Optics Communications*, vol. 227, no. 4-6, pp. 343 – 348, 2003. [Online]. Available: http://www.sciencedirect.com/science/article/pii/S0030401803020194

[224] A. Dragan, "Efficient fiber coupling of down-conversion photon pairs," *Phys. Rev. A*, vol. 70, no. 5, p. 053814, Nov. 2004. [Online]. Available: http://link.aps.org/doi/10.1103/PhysRevA.70.053814

[225] R. Andrews, E. Pike, and S. Sarkar, "Optimal coupling of entangled photons into single-mode optical fibers," *Opt. Express*, vol. 12, no. 14, pp. 3264–3269, Jul. 2004. [Online]. Available: http://www.opticsexpress.org/abstract.cfm?URI=oe-12-14-3264

[226] D. Ljunggren and M. Tengner, "Optimal focusing for maximal collection of entangled narrow-band photon pairs into single-mode fibers," *Phys. Rev. A*, vol. 72, no. 6, p. 062301, Dec. 2005. [Online]. Available: http://link.aps.org/doi/10.1103/PhysRevA.72.062301

[227] A. Ling, A. Lamas-Linares, and C. Kurtsiefer, "Absolute emission rates of spontaneous parametric down-conversion into single transverse gaussian modes," *Phys. Rev. A*, vol. 77, no. 4, p. 043834, Apr. 2008. [Online]. Available: http://link.aps.org/doi/10.1103/PhysRevA.77.043834

[228] M. W. Mitchell, "Parametric down-conversion from a wave-equation approach: Geometry and absolute brightness," *Phys. Rev. A*, vol. 79, p. 043835, Apr 2009. [Online]. Available: http://link.aps.org/doi/10.1103/PhysRevA.79.043835

[229] R. S. Bennink, "Optimal collinear gaussian beams for spontaneous parametric down-conversion," *Physical Review A*, vol. 81, no. 5, p. 053805, May 2010. [Online]. Available: http://link.aps.org/doi/10.1103/PhysRevA.81.053805

[230] S. Palacios, R. d. J. León-Montiel, M. Hendrych, A. Valencia, and J. P. Torres, "Flux enhancement of photons entangled in orbital angular momentum," *Optics Express*, vol. 19, no. 15, pp. 14 108–14 120, Jul. 2011. [Online]. Available: http://www.opticsexpress.org/abstract.cfm?URI=oe-19-15-14108

[231] T. Guerreiro, A. Martin, B. Sanguinetti, N. Bruno, H. Zbinden, and R. T. Thew, "High efficiency coupling of photon pairs in practice," *Optics Express*, vol. 21, no. 23, pp. 27 641–27 651, Nov. 2013. [Online]. Available: http://www.opticsexpress.org/abstract.cfm?URI=oe-21-23-27641

[232] P. B. Dixon, D. Rosenberg, V. Stelmakh, M. E. Grein, R. S. Bennink, E. A. Dauler, A. J. Kerman, R. J. Molnar, and F. N. Wong, "Heralding efficiency and correlated-mode coupling of near-ir fiber-coupled photon pairs," *Physical Review A*, vol. 90, no. 4, p. 043804, 2014.

[233] J. P. Torres, C. I. Osorio, and L. Torner, "Orbital angular momentum of entangled counterpropagating photons," *Opt. Lett.*, vol. 29, no. 16, pp. 1939–1941, Aug. 2004. [Online]. Available: http://ol.osa.org/abstract.cfm?URI=ol-29-16-1939

[234] S. P. Walborn, C. H. Monken, S. Pádua, and P. H. Souto Ribeiro, "Spatial correlations in parametric down-conversion," *Physics Reports*, vol. 495, no. 4-5, pp. 87–139, Oct. 2010. [Online]. Available: http://www.sciencedirect.com/science/article/pii/S0370157310001602

[235] G. D. Boyd and D. A. Kleinman, "Parametric interaction of focused gaussian light beams," *Journal of Applied Physics*, vol. 39, no. 8, pp. 3597–3639, 1968. [Online]. Available: http://link.aip.org/link/?JAP/39/3597/1

[236] F. Steinlechner, P. Trojek, M. Jofre, H. Weier, D. Perez, T. Jennewein, R. Ursin, J. Rarity, M. W. Mitchell, J. P. Torres, H. Weinfurter, and V. Pruneri, "A high-brightness source of polarization-entangled photons optimized for applications in free space," *Opt. Express*, vol. 20, no. 9, pp. 9640–9649, Apr. 2012. [Online]. Available: http://www.opticsexpress.org/abstract.cfm?URI=oe-20-9-9640

[237] S. Carrasco, A. V. Sergienko, B. E. A. Saleh, M. C. Teich, J. P. Torres, and L. Torner, "Spectral engineering of entangled two-photon states," *Phys. Rev. A*, vol. 73, no. 6, p. 063802, Jun. 2006. [Online]. Available: http://link.aps.org/doi/10.1103/PhysRevA.73.063802

[238] W. P. Grice, R. S. Bennink, D. S. Goodman, and A. T. Ryan, "Spatial entanglement and optimal single-mode coupling," *Physical Review A*, vol. 83, no. 2, p. 023810, Feb. 2011. [Online]. Available: http://link.aps.org/doi/10.1103/PhysRevA.83.023810

[239] F. M. Miatto, D. Giovannini, J. Romero, S. Franke-Arnold, S. M. Barnett, and M. J. Padgett, "Bounds and optimisation of orbital angular momentum bandwidths within parametric down-conversion systems," *The European Physical Journal D*, vol. 66, no. 7, pp. 1–6, Jul. 2012. [Online]. Available: http://link.springer.com/article/10.1140/epjd/e2012-20736-x

[240] A. Siegman, *Lasers*. University Science Books, 1986. [Online]. Available: http://books.google.de/books?id=1BZVwUZLTkAC

[241] M. D. Cunha Pereira, F. E. Becerra, B. L. Glebov, J. Fan, S. W. Nam, and A. Migdall, "Demonstrating highly symmetric single-mode, single-photon

heralding efficiency in spontaneous parametric downconversion," *Optics Letters*, vol. 38, no. 10, pp. 1609–1611, May 2013. [Online]. Available: http://ol.osa.org/abstract.cfm?URI=ol-38-10-1609

[242] A. Migdall, R. Datla, A. Sergienko, J. Orszak, and Y. Shih, "Absolute detector quantum-efficiency measurements using correlated photons," *Metrologia*, vol. 32, no. 6, p. 479, 1995.

[243] S. V. Polyakov and A. L. Migdall, "High accuracy verification of a correlated-photon- based method for determining photoncounting detection efficiency," *Opt. Express*, vol. 15, no. 4, pp. 1390–1407, Feb 2007. [Online]. Available: http://www.opticsexpress.org/abstract.cfm?URI=oe-15-4-1390

[244] T. Jennewein, *T. Toolbox for Quantum Photonics in Matlab. http://info.iqc.ca/qpl/ (accessed June 1, 2010).*

[245] A. Gallivanoni, I. Rech, D. Resnati, M. Ghioni, and S. Cova, "Monolithic active quenching and picosecond timing circuit suitable for large-area single-photon avalanche diodes," *Opt. Express*, vol. 14, no. 12, pp. 5021–5030, Jun. 2006. [Online]. Available: http://www.opticsexpress.org/abstract.cfm?URI=oe-14-12-5021

[246] J. F. Hodelin, G. Khoury, and D. Bouwmeester, "Optimal generation of pulsed entangled photon pairs," *Phys. Rev. A*, vol. 74, no. 1, p. 013802, Jul. 2006. [Online]. Available: http://link.aps.org/doi/10.1103/PhysRevA.74.013802

[247] M. Barbieri, F. De Martini, G. Di Nepi, P. Mataloni, G. M. D'Ariano, and C. Macchiavello, "Detection of entanglement with polarized photons: Experimental realization of an entanglement witness," *Phys. Rev. Lett.*, vol. 91, no. 22, p. 227901, Nov. 2003. [Online]. Available: http://link.aps.org/doi/10.1103/PhysRevLett.91.227901

[248] B.-S. Shi and A. Tomita, "Generation of a pulsed polarization entangled photon pair using a sagnac interferometer," *Physical Review A*, vol. 69, no. 1, p. 013803, Jan. 2004. [Online]. Available: http://link.aps.org/doi/10.1103/PhysRevA.69.013803

[249] D. E. Zelmon, J. J. Lee, K. M. Currin, J. M. Northridge, and D. Perlov, "Revisiting the optical properties of nd doped yttrium orthovanadate," *Appl. Opt.*, vol. 49, no. 4, pp. 644–647, Feb. 2010. [Online]. Available: http://ao.osa.org/abstract.cfm?URI=ao-49-4-644

[250] C. Abellán, "A comprehensive characterization of polarization-entangled photon pairs generated in a double-pass configuration," Master's thesis, ICFO - Institut de Ciencies Fotoniques, 2014.

[251] Y. Nambu, K. Usami, Y. Tsuda, K. Matsumoto, and K. Nakamura, "Generation of polarization-entangled photon pairs in a cascade of two type-i crystals pumped by femtosecond pulses," *Phys. Rev. A*, vol. 66, no. 3, p. 033816, Sep. 2002. [Online]. Available: http://link.aps.org/doi/10.1103/PhysRevA.66.033816

[252] A. Predojević, S. Grabher, and G. Weihs, "Pulsed sagnac source of polarization entangled photon pairs," *Optics Express*, vol. 20, no. 22, pp. 25 022–25 029, Oct. 2012. [Online]. Available: http://www.opticsexpress.org/abstract.cfm?URI=oe-20-22-25022

[253] S. Krapick, H. Herrmann, V. Quiring, B. Brecht, H. Suche, and C. Silberhorn, "An efficient integrated two-color source for heralded single photons," *New Journal of Physics*, vol. 15, no. 3, p. 033010, 2013. [Online]. Available: http://stacks.iop.org/1367-2630/15/i=3/a=033010

[254] C. Soeller, O. Cohen, B. J. Smith, I. A. Walmsley, and C. Silberhorn, "High-performance single-photon generation with commercial-grade optical fiber," *Phys. Rev. A*, vol. 83, no. 3, p. 031806, Mar. 2011. [Online]. Available: http://link.aps.org/doi/10.1103/PhysRevA.83.031806

[255] B. Wittmann, S. Ramelow, F. Steinlechner, N. K. Langford, N. Brunner, H. M. Wiseman, R. Ursin, and A. Zeilinger, "Loophole-free einstein-podolsky-rosen experiment via quantum steering," *New Journal of Physics*, vol. 14, no. 5, p. 053030, 2012. [Online]. Available: http://stacks.iop.org/1367-2630/14/i=5/a=053030

[256] M. Hentschel, H. Huebel, A. Poppe, and Anton Zeilinger, "Three-color sagnac source of polarization-entangled photon pairs," *Opt. Express*, vol. 17, no. 25, pp. 23 153–23 159, 2009. [Online]. Available: http://www.opticsexpress.org/abstract.cfm?URI=oe-17-25-23153

[257] A. Arora and S. Ghosh, "A twisted periscope arrangement for transporting elliptically polarized light without change in its polarization state," *Review of Scientific Instruments*, vol. 81, no. 12, pp. –, 2010. [Online]. Available: http://scitation.aip.org/content/aip/journal/rsi/81/12/10.1063/1.3518949

[258] M. Fiorentino, G. Messin, C. E. Kuklewicz, F. N. C. Wong, and J. H. Shapiro, "Generation of ultrabright tunable polarization entanglement without spatial, spectral, or temporal constraints," *Phys. Rev. A*, vol. 69, no. 4, p. 041801, Apr. 2004. [Online]. Available: http://link.aps.org/doi/10.1103/PhysRevA.69.041801

[259] M. Fiorentino, C. E. Kuklewicz, and F. N. C. Wong, "Source of polarization entanglement in a single periodically poled KTiOPO4 crystal with overlapping emission cones," *Optics Express*, vol. 13, no. 1, p. 127, 2005. [Online]. Available: http://www.opticsinfobase.org/oe/abstract.cfm?uri=oe-13-1-127

[260] J. Altepeter, E. Jeffrey, and P. Kwiat, "Phase-compensated ultra-bright source of entangled photons," *Opt. Express*, vol. 13, no. 22, pp. 8951–8959, Oct. 2005. [Online]. Available: http://www.opticsexpress.org/abstract.cfm?URI=oe-13-22-8951

[261] R. Rangarajan, M. Goggin, and P. Kwiat, "Optimizing type-i polarization-entangled photons," *Opt. Express*, vol. 17, no. 21, pp. 18 920–18 933, Oct. 2009. [Online]. Available: http://www.opticsexpress.org/abstract.cfm?URI=oe-17-21-18920

[262] D. H. Smith, G. Gillett, M. P. d. Almeida, C. Branciard, A. Fedrizzi, T. J. Weinhold, A. Lita, B. Calkins, T. Gerrits, H. M. Wiseman, S. W. Nam, and A. G. White, "Conclusive quantum steering with superconducting transition-edge sensors," *Nature Communications*, vol. 3, no. 625, 2012.

[263] F. Steinlechner, M. Gilaberte, M. Jofre, T. Scheidl, J. P. Torres, V. Pruneri, and R. Ursin, "Efficient heralding of polarization-entangled photons from type-0 and type-ii spontaneous parametric downconversion in periodically poled ktiopo 4," *JOSA B*, vol. 31, no. 9, pp. 2068–2076, 2014.

[264] S. K. JOSHI, "Entangled photon pairs: Efficient generation and detection, and bit commitment," Ph.D. dissertation, NUS Singapore, 2014.

Acknowledgments

I am dearly indebted to several people, without whom this thesis would not have been possible.

First, I would like to thank my thesis supervisor Prof. Valerio Pruneri for welcoming me into the Optoelectronics group at the Institute of Photonic Sciences and offering his support over the past four years, while also letting me follow my own research interests. It has been a truly enlightening period of my life, both professionally and personally, and I am sincerely grateful for having had the opportunity to work with, and learn from, the people that make ICFO unique.

Furthermore, I would like to thank Prof. Juan P. Torres for his introducing me to the theory of nonlinear quantum photonics and patiently discussing ideas, as well as Prof. Morgan Mitchell for letting me call upon his encyclopedic knowledge. I also thank Dr. Rupert Ursin for hosting my research stay at IQOQI and his contributions to various publications.

Special thanks also to Marc Jofre, Pavel Trojek, and Sven Ramelow for experimental advice and numerous fruitful discussions. Also many thanks to Adam Valles, Carlos Abellan, Linda Hirlehey, Robert Fass, and Lisa Ruby for proofreading the manuscript.

On a personal note, I would like to thank the entire OPTO group, for making sure I eat well at lunch time. You'll always have a seat of honor in my pintxos chiringuito cervezeria artesana! And to all the friends, flatmates, officemates, labmates, chefs, burgerlovers, and beachgoers who provided most welcome distractions from mining for photon pairs: I've had the time of my life, and I owe it all to you!

Finally, I would like to thank my family, for their continued loving support, my grandparents, Eileen May, Lawrence Edward, Dolly, and Josef, to whom I dedicate this thesis, for everything, and my love, Lisa, for everything else.